University of California
Santa Barbara

High-brightness lasers with spectral beam combining on silicon

A dissertation submitted in partial satisfaction
of the requirements for the degree

Doctor of Philosophy
in
Electrical and Computer Engineering

by

Eric John Stanton

Committee in charge:

Professor John E. Bowers, Chair
Professor Larry A. Coldren
Professor Nadir Dagli
Dr. Jerry R. Meyer

January 2018

The Dissertation of Eric John Stanton is approved.

Professor Larry A. Coldren

Professor Nadir Dagli

Dr. Jerry R. Meyer

Professor John E. Bowers, Committee Chair

January 2018

High-brightness lasers with spectral beam combining on silicon

by

Eric John Stanton

To Papa

Acknowledgements

My family has always supported and helped feed my engineering interests, even as a child. I give credit to my mom for guiding me to enjoy mathematics and to my dad for giving me my first engineering projects and lessons. Kevin, my brother, has been very close and consistently gives me the best competition. He may have been granted a Ph.D. first, but now the race is on to make the next breakthrough in physics! Benjamin Boyce and Nicholas Dazzi were also great friends and competition, both on and off the soccer field. I owe my physics curiosity to Papa.

During my undergraduate degree in electrical engineering, Cal Poly provided the many practical engineering skills and theoretical background to prepare me for graduate school. Since my childhood, I was fascinated with light. When I first heard that light was the fastest thing in the universe, I tried to observe it with my own eyes by flicking the light switch on and off. I was maybe 7 years old. Naturally, I began taking physics courses at Cal Poly to help improve my understanding. Cal Poly has many undergraduate-run research groups and I knew that joining one would give me valuable experience. By chance, I found myself in the PolySat lab working on CubeSat micro-satellite projects. It still amazes me how we somehow learned by brute-force to design, build, launch (by piggybacking), and operate satellites. However, I was always left wanting to understand more about the physics behind the systems we made, so I turned toward photonics.

UCSB has been an incredible experience and, equally, John Bowers was a stellar advisor. During my masters degree, I shared an office with Alexander Spott and Andreas De Groote. As I studied for the screening exam with Mihir Pendharkar and Alex, Andreas seemed to have great fun in distracting, pitying, and sometimes teaching us a few things. My first research project began under the guidance of Daryl Spencer, who was a valuable mentor and continues to be. The first year was a bit challenging to

manage time between courses like Electromagnetic Theory with Professor Nadir Dagli while working as a teaching assistant and trying to get started with optics research. I often heard more senior students say, "You will be glad once you are done with classes," but I always felt otherwise. They were right though. Once my masters degree was finished, I realized how liberating it is to do research full-time.

A few of the senior students and postdocs taught me most of what I know in photonics, including Daryl, Sudharsanan Srinivasan, Michael Davenport, Molly Piels, Jared Bauters, Jock Bovington, Martijn Heck, and Tin Komljenovic. Nicolas Volet has been exceptionally helpful with theory and programming, as well as being a good friend. Alex and I have worked well together on the Rainbow project and along with Akhilesh Khope, Warren Jin, Nicolas, and Tin have been excellent office-mates. A vital thanks is owed to our funding support from ONR and AFRL. I am greatly indebted to Jon Peters for all the cleanroom processing instructions, particularly with bonding. And, I wish the best for Aditya Malik, Junqian Liu, and Alex in continuing this project. To the rest of the Bowers group members, thank you for the keen scientific feedback: Emmett Perl, Jared Hulme, Alan Liu, Chong Zhang, Akhilesh Khope, Minh Tran, Duani Huang, Justin Norman, Paolo Pintus, Alfredo Torres, Andy Netherton, Lin Chang, Jinxi Huang, Robert Zhang, Jennifer Selvidge, Daehwan Jung, and the many other newcomers. Sometimes, research can be tedious, and I thank Geza Kurćzveil for perpetually providing humor in the laboratory setting.

Good mentors are invaluable. Professor Jonathan Klamkin quickly become a strong guide for me, especially with my job-search. I learned about lasers from Professor Larry Coldren and he always provided a steadfast voice of reason. Professor Nadir Dagli receives my admiration for being a model of unwavering theoretical knowledge. Jerry Meyer has been an excellence leader and an example of scientific prowess. Without a doubt, John

Bowers has guided, pushed, and led me to hone my scientific skills beyond any of my expectations.

Some of my favorite memories are from the annual Bowers ski trips to Colorado. Many thanks to John and Ariel for hosting all of us. Nothing gets your blood pumping like trying to keep up with Dan Blumenthal and John Bowers skiing through some dense trees!

My girlfriend, Maiya Bourland, and I came together during graduate school. She provided an incredible support for me and continues to do so. Throughout my time at UCSB, she listened to enough of the photonics issues I was working through that she probably could have written most of this thesis. Thanks for being there for me.

Curriculum vitæ
Eric John Stanton

Personal

Date of Birth: September 18, 1989

Place of Birth: San Jose, CA, U.S.A.

Email: eric.stanton22@gmail.com

Education

Ph.D. in Electronics & Photonics, Electrical & Computer Engineering, University of California Santa Barbara (UCSB), January 2018

M.Sc. in Electronics & Photonics, Electrical & Computer Engineering, UCSB, June 2014

B.Sc. in Electrical Engineering, California Polytechnic State University (Cal Poly), San Luis Obispo, CA, June 2012

Professional Activities

President, IEEE Photonics Society Student Chapter, UCSB, 2015–2016

Secretary, IEEE Photonics Society Student Chapter, UCSB, 2014–2015

Electrical Engineering Representative, College of Engineering Ambassadors, Cal Poly, 2010–2012

Awards and Honors

Most Innovative Chapter, IEEE Photonics Society Student Chapter, UCSB, 2017

Chapter of the Year, IEEE Photonics Society Student Chapter, UCSB, 2016

NASA Group Achievement Award, IPEX/CP-8 CubeSat Mission, Cal Poly, 2014

Holbrook Foundation Fellowship, Institute for Energy Efficiency, UCSB, 2012

Barpal Family Fellowship, UCSB Foundation, UCSB, 2012

Patent

I. Vurgaftman, J. R. Meyer, M. J. R. Heck, J. Bovington, A. Spott, **E. J. Stanton**, and J. E. Bowers, "Ultra-Broadband Photonic Integrated Circuit Platform and Ultra-Broadband Photonic Integrated Circuit," Patent No.: US 9,612,398 B2, filed Oct. 17, 2014, allowed Jan. 30, 2017, issued Apr. 4, 2017, **URL**.

Journal Publications

1. **E. J. Stanton**, A. Spott, J. Peters, M. L. Davenport, A. Malik, N. Volet, J. Liu, C. D. Merritt, W. W. Bewley, I. Vurgaftman, C. S. Kim, J. R. Meyer, and J. E. Bowers, "Multi-spectral quantum cascade laser on silicon with integrated multiplexer," *manuscript in preparation*, (2017).
2. **E. J. Stanton**, N. Volet, and J. E. Bowers, "Silicon arrayed waveguide gratings at 2.0-µm wavelength characterized with an on-chip resonator," *Opt. Lett.* **in press**, (2018).
3. N. Volet, X. Yi, Q.-F. Yang, **E. J. Stanton**, P. A. Morton, K. Y. Yang, K. J. Vahala, and J. E. Bowers, "Micro-resonator soliton generated directly with a diode laser," *manuscript submitted*, (2017).
4. **E. J. Stanton**, N. Volet, and J. E. Bowers, "Low-loss demonstration and refined characterization of silicon arrayed waveguide gratings in the near-infrared," *Opt. Express* **25**, 30651–30663 (2017), **URL**.
5. Z. Zhang, R. Wu, Y. Wang, C. Zhang, **E. J. Stanton**, C. L. Schow, K.-T. Cheng, and J. E. Bowers, "Compact Modeling for Silicon Photonic Heterogeneously Integrated Circuits," *J. Lightw. Technol.* **35**, 2973–2980 (2017), **URL**.
6. A. Spott, **E. J. Stanton**, N. Volet, J. Peters, J. R. Meyer, and J. E. Bowers, "Heterogeneous Integration for Mid-Infrared Silicon Photonics," *IEEE J. Sel. Topics Quantum Electron.* **23**, 8200810 (2017), **URL**.
7. N. Volet, A. Spott, **E. J. Stanton**, M. L. Davenport, L. Chang, J. D. Peters, T. C. Briles, I. Vurgaftman, J. R. Meyer, and J. E. Bowers, "Semiconductor optical amplifiers at 2.0-µm wavelength on silicon," *Laser Photon. Rev.* **11**, 1600165, (2017), **URL**.
8. L. Chang, M. H. P. Pfeiffer, N. Volet, M. Zervas, J. D. Peters, C. L. Manganelli, **E. J. Stanton**, Y. Li, T. J. Kippenberg, and J. E. Bowers, "Heterogeneous integration of lithium niobate and silicon nitride waveguides for wafer-scale photonic integrated circuits on silicon," *Opt. Lett.* **42**, 803–806, (2017), **URL**.
9. A. Spott, J. Peters, M. L. Davenport, **E. J. Stanton**, C. Zhang, C. D. Merritt, W. W. Bewley, I. Vurgaftman, C. S. Kim, J. R. Meyer, J. Kirch, L. J. Mawst, D. Botez, and J. E. Bowers, "Heterogeneously Integrated Distributed Feedback Quantum Cascade Lasers on Silicon," *Photonics* **3**, 35, (2016), **URL**.
10. A. Spott, J. Peters, M. L. Davenport, **E. J. Stanton**, C. D. Merritt, W. W. Bewley, I. Vurgaftman, C. S. Kim, J. R. Meyer, J. Kirch, L. J. Mawst, D. Botez, and J. E. Bowers, "Quantum cascade laser on silicon," *Optica* **3**, 545–551, (2016), **URL**.
11. S. Chien, J. Doubleday, D. R. Thompson, K. L. Wagstaff, J. Bellardo, C. Francis, E. Baumgarten, A. Williams, E. Yee, **E. J. Stanton**, and J. Piug-Suari, "Onboard Autonomy on the Intelligent Payload EXperiment CubeSat Mission," *J. Aerosp. Inform. Syst.* **0**, 1–9, (2016), **URL**.

12. **E. J. Stanton**, A. Spott, M. L. Davenport, N. Volet, and J. E. Bowers, "Low-loss arrayed waveguide grating at 760 nm," *Opt. Lett.* **41**, 1785–1788, (2016), **URL**.
13. T. Komljenovic, M. L. Davenport, J. Hulme, A. Y. Liu, C. T. Santis, A. Spott, S. Srinivasan, **E. J. Stanton**, C. Zhang, and J. E. Bowers, "Heterogeneous silicon photonic integrated circuits," *J. Lightw. Technol.* **34**, 20–35, (2016), **URL**.
14. **E. J. Stanton**, M. J. R. Heck, J. Bovington, A. Spott, and J. E. Bowers, "Multi-octave spectral beam combiner on ultra-broadband photonic integrated circuit platform," *Opt. Express* **23**, 11272–11283, (2015), **URL**.
15. A. Spott, M. L. Davenport, J. Peters, J. Bovington, M. J. R. Heck, **E. J. Stanton**, I. Vurgaftman, J. R. Meyer, and J. E. Bowers, "Heterogeneously integrated 2.0 µm CW hybrid silicon lasers at room temperature," *Opt. Lett.* **40**, 1480–1483, (2015), **URL**.

Conference Publications

1. A. Spott, **E. J. Stanton**, A. Torres, M. L. Davenport, C. L. Canedy, I. Vurgaftman, M. Kim, C. S. Kim, C. D. Merritt, W. W. Bewley, J. R. Meyer, and J. E. Bowers, "Interband Cascade Laser on Silicon," in *IEEE Photonics Conference (IPC)*, Post-Deadline Paper, Lake Buena Vista, Florida, 2017.
2. W. Jin, **E. J. Stanton**, N. Volet, R. G. Polcawich, D. Baney, P. Morton, and J. E. Bowers, "Piezoelectric tuning of a suspended silicon nitride ring resonator," in *IEEE Photonics Conference (IPC)*, paper MD3, Lake Buena Vista, Florida, 2017.
3. A. S. P. Khope, A. M. Netherton, T. Hirokawa, N. Volet, **E. J. Stanton**, C. Schow, R. Helkey, A. A. M. Saleh, J. E. Bowers, and R. C. Alferness, "Elastic WDM optoelectronic crossbar switch with on-chip wavelength control," in *Photonics in Switching*, New Orleans, Louisiana, 2017.
4. **E. J. Stanton**, N. Volet, and J. E. Bowers, "Low-loss arrayed waveguide grating at 2.0 µm," in *Conference on Lasers and Electro-Optics*, IEEE, paper STh1M.7, San Jose, CA, 2017, **URL**.
5. **E. J. Stanton**, N. Volet, T. Komljenovic, and J. E. Bowers, "Star coupler for high-etendue LIDAR," in *Conference on Lasers and Electro-Optics*, IEEE, paper STh1M.4, San Jose, CA, 2017, **URL**.
6. L. Chang, M. H. P. Pfeiffer, N. Volet, M. Zervas, J. D. Peters, C. L. Manganelli, **E. J. Stanton**, Y. Li, T. J. Kippenberg, and J. E. Bowers, "A lithium niobate-Si_3N_4 platform on silicon by heterogeneous wafer bonding," in *Conference on Lasers and Electro-Optics*, IEEE, paper SM4O.2, San Jose, CA, 2017, **URL**.
7. **E. J. Stanton**, A. Spott, N. Volet, M. L. Davenport, and J. E. Bowers, "High-brightness lasers on silicon by beam combining," in *Proc. SPIE 10108, Silicon Photonics XII, 101080K*, San Francisco, CA, 2017, **URL**.

8. A. Spott, J. D. Peters, M. L. Davenport, **E. J. Stanton**, C, Zhang, W. W. Bewley, C. D. Merritt, I. Vurgaftman, C. S. Kim, J. R. Meyer, J. D. Kirch, L. J. Mawst, D. Botez, and J. E. Bowers, "Quantum cascade lasers on silicon," in *Proc. SPIE 10123, Novel In-Plane Semiconductor Lasers XVI, 101230I*, San Francisco, CA, 2017, **URL**.
9. **E. J. Stanton**, N. Volet, and J. E. Bowers, "Ring resonator with cascaded arrayed waveguide gratings for accurate insertion loss measurement," in *IEEE Photonics Conference (IPC)*, paper MB3.4, Waikoloa, HI, 2016, **URL**.
10. N. Volet, **E. J. Stanton**, M. L. Davenport, A. Spott, L. Chang, and J. E. Bowers, "Refined procedure for gain measurement in Fabry-Perot semiconductor lasers," in *IEEE Photonics Conference (IPC)*, paper WC1.2, Waikoloa, HI, 2016, **URL**.
11. T. Brashears, P. Lubin, N. Rupert, **E. Stanton**, A. Mehta, P. Knowles, and G. B. Hughes, "Building the future of WaferSat spacecraft for relativistic spacecraft," in *Proc. SPIE 9981, Planetary Defense and Space Environment Applications, 998104* ,San Diego, CA, 2016, **URL**.
12. A. Spott, J. Peters, M. L. Davenport, **E. J. Stanton**, C. Zhang, W. W. Bewley, C. D. Merritt, I. Vurgaftman, C. S. Kim, J. R. Meyer, J. Kirch, L. J. Mawst, D. Botez, and J. E. Bowers, "Distributed feedback quantum cascade lasers on silicon," at *International Semiconductor Laser Conference (ISLC)*, IEEE, paper TuB3, Kobe, Japan, 2016, **URL**.
13. **E. J. Stanton**, A. Spott, M. L. Davenport, N. Volet, and J. E. Bowers, "Arrayed waveguide grating near 760 nm wavelength for integrated spectral beam combining applications," in *Conference on Lasers and Electro-Optics*, IEEE, paper SM1F.1, San Jose, CA, 2016, **URL**.
14. A. Spott, J. Peters, M. L. Davenport, **E. J. Stanton**, C. Merritt, W. Bewley, I. Vurgaftman, J. R. Meyer, J. Kirch, L. Mawst, D. Botez, and J. E. Bowers, "Quantum Cascade Laser on Silicon at 4.8 µm," in *Conference on Lasers and Electro-Optics*, IEEE, paper STh3L.4, San Jose, CA, 2016, **URL**.
15. N. Volet, A. Spott, **E. J. Stanton**, M. L. Davenport, J. Peters, J. R. Meyer, and J. E. Bowers, "Semiconductor optical amplifiers at 2.0-µm wavelength heterogeneously integrated on silicon," in *Conference on Lasers and Electro-Optics*, IEEE, paper SM4G.4, San Jose, CA, 2016, **URL**.
16. J. E. Bowers, T. Komljenovic, M. L. Davenport, J. Hulme, A. Y. Liu, C. T. Santis, A. Spott, S. Srinivasan, **E. J. Stanton**, and C. Zhang, "Recent advances in silicon photonic integrated circuits," in *Proc. SPIE 9774, Next-Generation Optical Communication: Components, Sub-Systems, and Systems V, 977402*, San Francisco, CA, 2016, **URL**.
17. **E. J. Stanton**, M. J. R. Heck, J. Bovington, A. Spott, and J. E. Bowers, "Ultra-broadband Spectral Beam Combiner," *Conference on Lasers and Electro-Optics*, IEEE, San Jose, CA, 2015, **URL**.

18. J. E. Bowers, **E. J. Stanton**, M. J. R. Heck, A. Spott, M. L. Davenport, A. Y. Liu, J. T. Bovington, J. R. Meyer, C. L. Canedy, J. Abell, C. D. Merritt, W. W. Bewley, C. S. Kim, and I. Vurgaftman, "Technology for Multispectral Infrared Laser Integration on Silicon," at *IEEE Photonics Society Summer Topical Meeting Series*, Montreal, QC, 2014, **URL**.

19. S. Chien, J. Doubleday, D. Thompson, K. Wagstaff, J. Bellardo, C. Francis, E. Baumgarten, A. Williams, E. Yee, D. Fluitt, **E. J. Stanton**, and J. Piug-Suari, "Onboard Autonomy on the Intelligent Payload EXperiment (IPEX) Cubesat Mission: A pathfinder for the proposed HyspIRI Mission Intelligent Payload Module," in *Proc. 12th International Symposium in Artificial Intelligence, Robotics and Automation in Space*, Montreal, QC, 2014, **URL**.

20. S. Chien, J. Doubleday, D. Tran, J. Bellardo, C. Francis, E. Baumgarten, A. Williams, E. Yee, D. Fluitt, **E. J. Stanton**, and J. Piug-Suari, "Onboard Mission Planning on the Intelligent Payload Experiment (IPEX) Cubesat Mission," in *Proc. International Workshop on Planning and Scheduling for Space*, Moffett Field, CA, 2013, **URL**.

21. J. J. Puschell, and **E. J. Stanton**, "CubeSat modules for multispectral environmental imaging from polar orbit," in *Proc. SPIE 8516, Remote Sensing System Engineering IV, 85160B*, San Diego, CA, 2012, **URL**.

22. S. Chien, J. Doubleday, K. Ortega, T. Flatley, G. Crum, A. Geist, M. Lin, A. Williams, J. Bellardo, J. Puig-Suari, **E. J. Stanton**, and E. Yee, "Onboard processing and autonomous operations on the IPEX Cubesat," at *4th Annual Government Forum on CubeSats (GFC)*, Greenbelt, MD, 2012, **URL**.

23. **E. J. Stanton**, E. Yee, S. Chien, J. Doubleday, K. Ortega, T. Flatley, G. Crum, A. Geist, M. Lin, A. Williams, J. Bellardo, and J. Puig-Suari, "IPEX - Maximizing 1U Payload Potential," at *9th Annual Spring CubeSat Developer's Workshop*, San Luis Obispo, CA, 2012, **URL**.

Abstract

High-brightness lasers with spectral beam combining on silicon

by

Eric John Stanton

Modern implementations of absorption spectroscopy and infrared-countermeasures demand advanced performance and integration of high-brightness lasers, especially in the molecular fingerprint spectral region. These applications, along with others in communication, remote-sensing, and medicine, benefit from the light source comprising a multitude of frequencies. To realize this technology, a single multi-spectral optical beam of near-diffraction-limited divergence is created by combining the outputs from an array of laser sources. Full integration of such a laser is possible with direct bonding of several epitaxially-grown chips to a single silicon (Si) substrate. In this platform, an array of lasers is defined with each gain material, creating a densely spaced set of wavelengths similar to wavelength division multiplexing used in communications.

Scaling the brightness of a laser typically involves increasing the active volume to produce more output power. In the direction transverse to the light propagation, larger geometries compromise the beam quality. Lengthening the cavity provides only limited scaling of the output power due to the internal losses. Individual integrated lasers have low brightness due to combination of thermal effects and high optical intensities. With heterogeneous integration, many lasers can be spectrally combined on a single integrated chip to scale brightness in a compact platform. This allows for the gain region to be separated from the output facet and the beam quality to be optimized without the typical degradations of and active facet. Compared to a laser array, the beam-combing approach is predicted to improve the brightness by a factor of 5. Recent demonstrations of 2.0-

µm diode and 4.8-µm quantum cascade lasers on Si have extended this heterogeneous platform beyond the telecommunications band to the mid-infrared.

In this work, low-loss beam combining elements spanning the visible to the mid-infrared are developed and a high-brightness multi-spectral laser is demonstrated in the range of 4.6–4.7-µm wavelengths. An architecture is presented where light is combined in multiple stages: first within the gain-bandwidth of each laser material and then coarsely between each spectral band to a single output waveguide. All components are demonstrated on a common material platform with a Si substrate, which lends feasibility to the complete system integration. Particular attention is focused on improving the efficiency of arrayed waveguide gratings (AWGs), used in the dense wavelength combining stage. This requires development of a refined characterization technique involving AWGs in a ring-resonator configuration to reduce measurement uncertainty. New levels of low-loss are achieved for visible, near-infrared, and mid-infrared multiplexing devices. Also, a multi-spectral laser in the mid-infrared is demonstrated by integrating an array of quantum cascade lasers and an AWG with Si waveguides. The output power and spectra are measured, demonstrating efficient beam combining and power scaling. Thus, a bright laser source in the mid-infrared has been demonstrated, along with an architecture and the components for incorporating visible and near-infrared optical bands.

Contents

List of figures

List of tables

Chapter 1

Introduction

1.1 The science of light

Spurred by the invention of the laser in 1960 [1], photonics serves as the backbone of the modern age. It has delivered unprecedented communication connectivity [2], the discovery of a new state of matter [3], life-saving medical tools [4], environmental sensing and monitoring capabilities [5], and a the next era in astronomy by observing gravitational waves [6]. All these applications and many more have been enabled by the generation and manipulation of light. The largest technological revolution stimulated by photonics is in communication with the advent of the internet and mobile phones. Development in this field led to major advances in laser performance and increased integration to reap benefits similar to those found in electronics: smaller size, large-scale manufacturing for cost reduction, more complex circuits, and faster data rates. This miniaturization opens new applications for photonics and often leads to higher efficiencies and greater wavelength flexibility. Now, the growth rate of photonic research is more rapid than ever before, partially driven by the prospect of highly mature manufacturing. In just this past decade,

twenty-three new photonics-specific journals were introduced[1]. The work in this thesis contributes to the trend of increasing performance with a high level of integration. Using the silicon (Si) photonic platform, technology for an ultra-broadband multi-spectral laser spanning the ultra-violet (UV) to the mid-infrared (mid-IR) is introduced. Molecular identification and quantification via absorption spectroscopy is a primary application and others include infrared countermeasures, free-space communication, remote sensing, medicine, industrial manufacturing, and fundamental science.

1.2 Lasers on silicon

Integrating lasers on Si substrates has been an enduring topic of research in photonics. There are many reasons to use the Si photonic platform, though the biggest driving factor is the potential for large-scale manufacturing that leverages current infrastructure investments from the electronics industry. The challenge is that materials with efficient optical gain, pumped with electrical current are not easily grown by an epitaxial method [7–10]. Although crystal growth is the preferred technique for large-scale manufacturing, an alternative approach was developed by bonding a III–V gain material to Si [11]. This technology has been adopted by many research groups and industry leaders[2]. Others

[1]The Optical Society (OSA) founded *Journal of Optical Society of Korea* in 2007, *Advances in Optics and Photonics* in 2009, *Biomedical Optics Express* in 2010, *Optical Materials Express* in 2011, *Photonics Research* in 2013, and *Optica* in 2014. The Institute of Electrical and Electronics Engineers (IEEE) Photonics Society founded the *IEEE Photonics Journal* in 2009. The American Institute of Physics (AIP) founded *APL Photonics* in 2016. John Wiley & Sons (Wiley) founded *Laser & Photonics Reviews* in 2007 and *Advanced Optical Materials* in 2013. Springer Nature founded *Nature Photonics* in 2007 and *Light: Science & Applications* in 2012. De Gruyter founded *Nanophotonics* in 2012. SPIE founded the *Journal of Nanophotonics* in 2007, the *Journal of Photonics for Energy* in 2011, *Neurophotonics* in 2014, the *Journal of Medical Imaging* in 2014, and the *Journal of Astronomical Telescopes, Instruments, and Systems* in 2015. The American Chemical Society (ACS) founded *ACS Photonics* in 2014. The Multidisciplinary Digital Publishing Institute (MDPI) founded *Photonics* in 2014. Springer founded *Photonic Sensors* in 2011 and *Lasers in Dental Science* in 2017. Frontiers founded *Optics and Photonics* in 2014.

[2]Juniper Networks Inc. (previously Aurrion Inc.), Intel Corp., Hewlett Packard Enterprise, and Axalume, Inc. (previously Oracle Corporation) use heterogeneous integration of III–V materials on Si substrates.

are working on Si photonic products as well[3]. There are many examples of advanced photonic integrated circuits (PICs) on Si that leverage the integration of electronics with photonics [12] and Si photonics continues find new applications that benefit from its unique versatility, low-cost, and high performance.

In addition to the initial motivations for integrating lasers on Si, the heterogeneous platform serves as a unique method for integrating completely separate and different III–V materials to a single substrate. In optical communications, this is beneficial for integrating lasers, modulators, and photodetectors without performing re-growth steps [13]. This also allows for lasers from different spectral bands to be integrated on a single substrate [14]. This feature is the primary motivation behind the work in this thesis. If a passive waveguide platform can be designed to support the wavelengths generated by the bonded gain-material, then a platform spanning the UV to the mid-IR is possible. Lasers have been demonstrated in the UV and the visible (VIS) based on gallium nitride (GaN) substrates. Separately, GaN has been bonded with a metal interface to Si for vertical emission of light emitting diode and laser devices [15, 16]. Gallium arsenide (GaAs) substrates support efficient laser growth in the VIS and near-infrared (near-IR) and GaAs has been bonded to Si substrates [17]. Indium phosphide (InP) is ubiquitous in photonics for near-IR light generation in the telecommunication bands and was the first material used to demonstrate the heterogeneous laser on Si [11]. Coincidentally, InP is also the substrate material of quantum cascade lasers (QCLs), which efficiently emit light in the mid-IR [18]. Also, interband cascade lasers (ICLs) are grown on gallium antimonide (GaSb) substrates, producing more efficient lasers on the short-wavelength side of the mid-IR band.

[3]Cisco Corp. (previously Lightwire Inc.), Luxtera Inc., Acacia Communications Inc., and Mellanox Technologies (previously Kotura Inc.) are developing Si-based photonic devices.

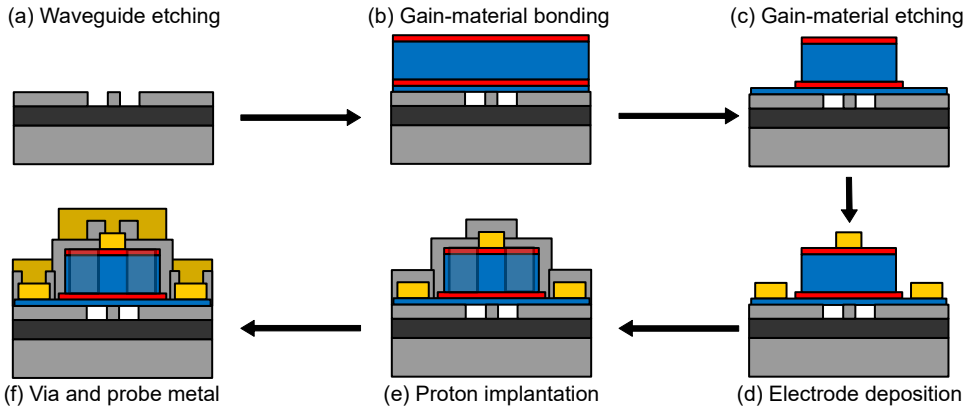

Figure 1.1: Generic fabrication process for heterogeneous integration. (a) Waveguides are defined in Si. (b) III–V gain material is bonded. (c) Laser mesas are etched through the top-contact, top-cladding, and active regions. (d) Electrodes are patterned with a lift-off process. (e) Protons are implanted using the top-electrode as a mask. An electrically insulating layer is deposited. (f) Vias are etched and probe metal is deposited.

The fabrication process to integrate lasers on Si by direct bonding has progressively been optimized since its first demonstrated in 2006. A current nominal process follows the steps in Fig. 1.1. Nearly all demonstrations begin with a Si-on-insulator (SOI) wafer, which are widely available with high quality[4]. Advancements to the fabrication process involve reducing the Si waveguide propagation loss, developing methods to improve bonding yield, decreasing contact resistances, and improving the transition from the hybrid III–V/Si mode to the purely passive Si waveguide. It is hypothesized that processing steps involving hydrogen may be limiting the III–V/Si taper transition [19]. However, the fabrication process is not limiting development with this technology. Research in this field is increasingly focused on more complex PICs that incorporate large numbers and varieties of photonic devices.

[4]High resistance Si with low doping is preferred to reduce free-carrier absorption. Also, layer thickness precision and uniformity are critical features for high performance photonic devices.

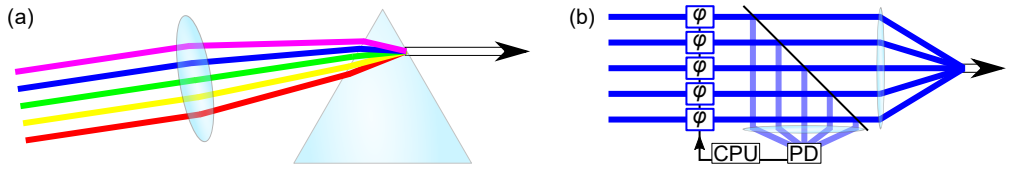

Figure 1.2: Schematics of (a) spectral and (b) coherent beam combining. In (b), the path length differences between the feedback and output arms are equal.

1.3 High-brightness lasers

A high-brightness laser is a high-power laser that emits light to a near-diffraction limited beam. Brightness is defined as the output power divided by the beam quality parameter[5]. There are two methods of scaling the power from individual lasers to create a high-brightness source with high efficiency: spectral and coherent beam combining. Both these schemes are depicted in Fig. 1.2. Spectral beam combining relies on passive elements to combine a set of various input wavelengths to a single spacial output beam, either using angular dispersion or a diffraction gratings. Coherent beam combining takes several inputs, all with exact same wavelength, and generates a single output by controlling the physical position and phase of each input to constructively interfere all input beams to a designated focus. A key distinction is that spectral beam combining does not require feedback, while coherent beam combining does. Also, spectral beam combining is inherently multi-spectral, while coherent beam combining is inherently uni-spectral.

A passive waveguide can be designed with a near-diffraction limited output, though it is challenging to do so over a broad spectral band. High-power lasers with III–V facets typically have a low beam quality due to thermal and non-linear optical effects that modify the optical mode profile at the output facet, induce absorption, or both. The heterogeneous Si platform does not suffer from the same limitation; however, Si

[5]This is described in more detail in Section 3.5.

exhibits a non-linear two-photon absorption (TPA) in the near-IR, which begins to limit the output power at around several hundred mW. A multi-spectral laser can produce a total output power much greater than the TPA limit, as long as each channel does not exceed the limit. It is shown in Chapter 3 that a single multi-spectral output waveguide has $\sim 5\times$ higher brightness than an array of eight lasers.

Using individual laser sources with one laser per substrate to make ultra-broadband multi-spectral would require bulk optical packaging to integrate a free-space multiplexer and separate mounts for each laser. The primary advantage of integrating all the wavelengths sources and multiplexer together on a single chip is that the size is reduced and the mechanical stability is improved.

1.4 Arrayed waveguide gratings

Arrayed waveguide gratings (AWGs) with low loss and high fundamental-mode transmission are an important part of a high-brightness multi-spectral integrated laser. These devices are waveguide-based diffraction gratings that route multiple input waveguides, containing different wavelengths, to a single output waveguide. Nearly three decades ago, the first AWGs were designed and demonstrated [20–23] and the arrayed waveguide transition to the free propagation region was rigorously investigated [24]. A schematic of the AWG design is shown in Fig. 1.3. Light from an array of lasers with dense channel spacing can be combined with a low insertion loss to allow for power or brightness scaling. Coarse spectral combining better suited for other devices, such as directional couplers, adiabatic couplers, or planar concave gratings [25]. The spectral combining architecture presented in this work relies on AWGs, adiabatic couplers, and a modified adiabatic coupler, called the ultra-broadband coupler.

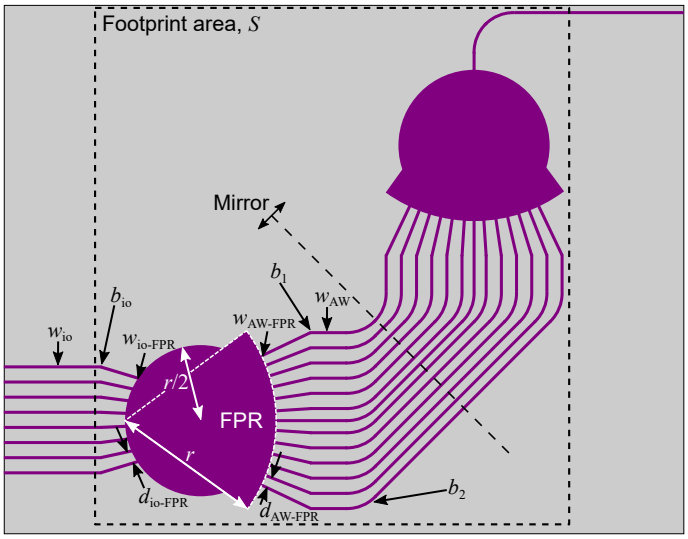

Figure 1.3: Diagram of the basic AWG layout.

The waveguide platforms for AWGs at each wavelength use a common Si substrate. Core and cladding materials consist of Si, SiO_2, and Si_3N_4. These materials are compatible with large-volume infrastructures, currently used for complementary metal–oxide–semiconductor (CMOS) fabrication [26], allowing for the potential of low-cost devices with high performance. By choosing materials with low absorption loss, AWGs can be designed to combine light from the VIS [27, 28] to the mid-IR [29, 30]. Developing devices across this wavelength range also has a broad impact in supporting applications in spectroscopy, communication, astronomy, remote sensing, and others yet discovered.

1.5 Mid-infrared photonics

There is an immediate relevancy for mid-IR multi-spectral integrated sources to reduce the cost and size of molecular detection and quantification devices. Environmental monitoring is important in industrial, military, residential setting. Data from these devices could be used to detect gas leaks, improve air-quality monitoring, screen medical products for contaminants, and support many other applications due to the fundamental

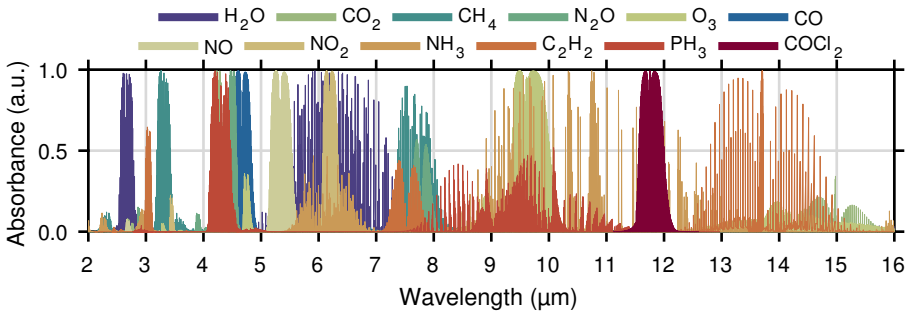

Figure 1.4: Absorption lines for many greenhouse and toxic gases in the mid-IR.

nature of intermolecular forces. The strongest rotational-vibrational resonances of molecular bonds occur at frequencies corresponding to photons in the mid-IR, especially at wavelengths in the range of 2–16 µm [31]. This is responsible for narrow and distinct absorption features that create a spectral "fingerprint" that is used to identify molecules. An example of some important greenhouse and toxic gas absorption spectra is shown in Fig. 1.4 [32].

Absorption spectra are obtained with two methods of transmitting light through a sample. The first is to send a single frequency which is tunable and make time-resolved measurements that correspond to the tuning frequency. The second is to send a broad, continuous or comb, of frequencies and then de-multiplex the sample. This second method is the target of the high-brightness multi-spectral laser described in this work. Efficient on-chip beam combiners are reciprocal and can serve as de-multiplexers on the detection side.

1.6 Thesis overview

The architecture for an ultra-broadband high-brightness laser, the passive beam combining components, and a single-band multi-spectral laser are presented in this thesis. Designs methodologies for the beam combining elements are contributed and an improved

characterization technique for the AWGs is introduced. Beam combining is demonstrated for dense and coarse stages from the VIS to the mid-IR. To culminate, a multi-spectral QCL is demonstrated, integrating an array of lasers combined with an AWG.

In Chapter 2, the architecture of a high-brightness multi-spectral laser implemented on a single chip is discussed. The waveguide platform that supports a low loss over an ultra-broadband is presented in Chapter 2. These waveguides are used to demonstrate AWGs in Chapter 4. A part of the AWG, the star coupler, is also investigated separately in Chapter 5. Devices for ultra-broadband spectral beam combining in Chapter 6 compliment the AWGs and culminate the demonstration of the passive components for the multi-spectral beam combining circuit. Since the mid-IR spectral band is of particular interest due to its relation to molecular resonances, the first multi-spectral laser demonstrated in this wavelength range. A multi-spectral mid-IR laser is demonstrated in Chapter 7 with an array of quantum cascade lasers (QCLs) coupled to an AWG. Chapter 8 concludes the thesis and gives a prospective view of related research.

References

[1] T. H. Maiman, "Stimulated optical radiation in ruby," Nature **187**, 493–494 (1960).

[2] G. P. Agrawal, *Fiber-optic communication systems*, vol. 222 (John Wiley & Sons, 2012).

[3] K. B. Davis, M.-O. Mewes, M. R. Andrews, N. J. Van Druten, D. S. Durfee, D. M. Kurn, and W. Ketterle, "Bose-Einstein condensation in a gas of sodium atoms," Phys. Rev. Lett. **75**, 3969 (1995).

[4] J. A. S. Carruth, "Lasers in medicine and surgery," J. Med. Eng. Technol. **8**, 161–167 (1984).

[5] P. A. Martin, "Near-infrared diode laser spectroscopy in chemical process and environmental air monitoring," Chem. Soc. Rev. **31**, 201–210 (2002).

[6] B. P. Abbott, R. Abbott, T. Abbott, M. Abernathy, F. Acernese, K. Ackley, C. Adams, T. Adams, P. Addesso, R. Adhikari *et al.*, "Observation of gravitational waves from a binary black hole merger," Phys. Rev. Lett. **116**, 061102 (2016).

[7] J. M. Shainline and J. Xu, "Silicon as an emissive optical medium," Laser Photon. Rev. **1**, 334–348 (2007).

[8] L. Pavesi, S. Gaponenko, and L. Dal Negro, *Towards the first silicon laser*, vol. 93 (Springer Science & Business Media, 2012).

[9] Z. Zhou, B. Yin, and J. Michel, "On-chip light sources for silicon photonics," Light Sci. Appl. **4**, e358 (2015).

[10] S. Chen, W. Li, J. Wu, Q. Jiang, M. Tang, S. Shutts, S. N. Elliott, A. Sobiesierski, A. J. Seeds, I. Ross *et al.*, "Electrically pumped continuous-wave III–V quantum dot lasers on silicon," Nat. Photon. **10**, 307–311 (2016).

[11] A. W. Fang, H. Park, O. Cohen, R. Jones, M. J. Paniccia, and J. E. Bowers, "Electrically pumped hybrid AlGaInAs-silicon evanescent laser," Opt. Express **14**, 9203–9210 (2006).

[12] M. H. Idjadi and F. Aflatouni, "Integrated Pound-Drever-Hall laser stabilization system in silicon," Nat. Commun. **8**, 1209 (2017).

[13] C. Zhang and J. E. Bowers, "Silicon photonic terabit/s network-on-chip for datacenter interconnection," Opt. Fiber Technol. (2017).

[14] H.-H. Chang, Y.-h. Kuo, R. Jones, A. Barkai, and J. E. Bowers, "Integrated hybrid silicon triplexer," Opt. Express **18**, 23891–23899 (2010).

[15] W. Wong, T. Sands, N. Cheung, M. Kneissl, D. Bour, P. Mei, L. Romano, and N. Johnson, "$In_xGa_{1-x}N$ light emitting diodes on Si substrates fabricated by Pd–In metal bonding and laser lift-off," Appl. Phys. Lett. **77**, 2822–2824 (2000).

[16] D. Kasahara, D. Morita, T. Kosugi, K. Nakagawa, J. Kawamata, Y. Higuchi, H. Matsumura, and T. Mukai, "Demonstration of blue and green GaN-based vertical-cavity surface-emitting lasers by current injection at room temperature," Appl. Phys. Express **4**, 072103 (2011).

[17] J. T. Bovington, M. J. R. Heck, and J. E. Bowers, "Heterogeneous lasers and coupling to Si_3N_4 near 1060 nm," Opt. Lett. **39**, 6017–6020 (2014).

[18] J. Faist, F. Capasso, D. L. Sivco, C. Sirtori, A. L. Hutchinson, and A. Y. Cho, "Quantum Cascade Laser," Science **264**, 553–556 (1994).

[19] M. L. Davenport. Personal communication.

[20] M. K. Smit, "New focusing and dispersive planar component based on an optical phased array," Electron. Lett. **24**, 385–386 (1988).

[21] H. Takahashi, S. Suzuki, K. Kato, and I. Nishi, "Arrayed-waveguide grating for wavelength division multi/demultiplexer with nanometre resolution," Electron. Lett. **26**, 87–88 (1990).

[22] C. Dragone, "An $N \times N$ optical multiplexer using a planar arrangement of two star couplers," IEEE Photon. Technol. Lett. **3**, 812–815 (1991).

[23] C. Dragone, C. Edwards, and R. Kistler, "Integrated optics $N \times N$ multiplexer on silicon," IEEE Photon. Technol. Lett. **3**, 896–899 (1991).

[24] C. Dragone, "Optimum design of a planar array of tapered waveguides," J. Opt. Soc. Am. A **7**, 2081–2093 (1990).

[25] J. Brouckaert, W. Bogaerts, S. Selvaraja, P. Dumon, R. Baets, and D. Van Thourhout, "Planar concave grating demultiplexer with high reflective Bragg reflector facets," IEEE Photon. Technol. Lett. **20**, 309–311 (2008).

[26] T. Baehr-Jones, T. Pinguet, P. L. Guo-Qiang, S. Danziger, D. Prather, and M. Hochberg, "Myths and rumours of silicon photonics," Nat. Photon. **6**, 206–208 (2012).

[27] S. Bloom, E. Korevaar, J. Schuster, and H. Willebrand, "Understanding the performance of free-space optics [invited]," J. Opt. Netw. **2**, 178–200 (2003).

[28] Z. Hu, A. Glidle, C. N. Ironside, M. Sorel, M. J. Strain, J. Cooper, and H. Yin, "Integrated microspectrometer for fluorescence based analysis in a microfluidic format," Lab Chip **12**, 2850–2857 (2012).

[29] A. Malik, M. Muneeb, S. Pathak, Y. Shimura, J. Van Campenhout, R. Loo, and G. Roelkens, "Germanium-on-Silicon Mid-Infrared Arrayed Waveguide Grating Multiplexers," IEEE Photon. Technol. Lett. **25**, 1805–1808 (2013).

[30] M. Muneeb, X. Chen, P. Verheyen, G. Lepage, S. Pathak, E. Ryckeboer, A. Malik, B. Kuyken, M. Nedeljkovic, J. Van Campenhout, G. Z. Mashanovich, and G. Roelkens, "Demonstration of Silicon-on-insulator mid-infrared spectrometers operating at 3.8 µm," Opt. Express **21**, 11659–11669 (2013).

[31] T. Schadle, B. Pejcic, M. Myers, and B. Mizaikoff, "Portable Mid-Infrared Sensor System for Monitoring CO_2 and CH_4 at High Pressure in Geosequestration Scenarios," ACS Sensors **1**, 413–419 (2016).

[32] L. S. Rothman, I. E. Gordon, Y. Babikov, A. Barbe, D. C. Benner, P. F. Bernath, M. Birk, L. Bizzocchi, V. Boudon, L. R. Brown, A. Campargue, K. Chance, E. A. Cohen, L. H. Coudert, V. M. Devi, B. J. Drouin, A. Fayt, J.-M. Flaud, R. R. Gamache, J. J. Harrison, J.-M. Hartmann, C. Hill, J. T. Hodges, D. Jacquemart, A. Jolly, J. Lamouroux, R. J. L. Roy, G. Li, D. A. Long, O. M. Lyulin, C. J. Mackie, S. T. Massie, S. Mikhailenko, H. S. P. Muller, O. V. Naumenko, A. V. Nikitin, J. Orphal, V. Perevalov, A. Perrin, E. R. Polovtseva, C. Richard, M. A. H. Smith, E. Starikova, K. Sung, S. Tashkun, J. Tennyson, G. C. Toon, V. G. Tyuterev, and G. Wagner, "The HITRAN2012 molecular spectroscopic database," J. Quant. Spectrosc. Radiat. Transfer **130**, 4–50 (2013).

Chapter 2

High-brightness laser architecture

2.1 Introduction

For applications in manufacturing, remote sensing, medicine, military, and fundamental science, an ideal laser would have high output power and a diffraction-limited beam. The figure-of-merit to describe this property is the brightness, which scales proportional to output power and inverse to the beam quality factor M^2. Lasers that are both compact and have high-brightness are challenging to realize. As the size of the laser is reduced, either the output power is decreased or the M^2 is increased, primarily due to a combination of thermal effects and high optical intensities [1, 2]. Many applications, such as spectroscopy, infrared countermeasures, free-space communication, and industrial manufacturing, benefit from the light source having multiple frequencies. A compact and high-brightness laser can then be achieved by spectral beam combining [3]. This PIC may expand on the spectral bandwidth of currently available optical sources for less cost, smaller size, reduced vibration sensitivity, and higher brightness.

Over the past decade, advances in heterogeneous lasers on Si enable such a multi-frequency and high-brightness laser to be integrated on a single cost-effective substrate

[4, 5]. With multiple die bonding [6, 7], materials exhibiting optical gain at various wavelengths are brought together onto a Si chip and lasers are formed with integrated mirrors. Outputs from each laser can be combined with various stages of wavelength division multiplexing optical elements [8], as shown in Fig. 2.1. Semiconductor optical amplifiers (SOAs) are critical components for many kinds of photonic integrated circuits to increase output power or maintain signal levels as the signal propagates throughout a large number of optical components [9]. In our approach, SOAs are integrated on the same platform with the lasers on Si and, in addition to the concept of Fig. 2.1, could be used to increase power following each intra-band combiner.

This manuscript reviews recent progress on integration of multiple laser sources on a chip that combines the outputs to a single waveguide. Each laser gain material could support many lasers with densely spaced wavelengths, similar to modern optical communication systems filling the optical bandwidth of the erbium-doped-fiber-amplifier with densely-spaced frequency channels. To extend the spectral capacity of the Si-on-insulator (SOI) platform beyond the transmission window supported by a Si-core and silicon dioxide (SiO_2) -clad waveguide, a silicon nitride (Si_3N_4) waveguide layer can be added [8]. Optical sources at 1.0-µm [10], 1.3-µm [11], 1.5-µm [4], 2.0-µm [12], and 4.8-µm [13] wavelengths on Si have been demonstrated separately. Efficient integrated spectral combining elements have been investigated for coarse and dense wavelength combining stages [8]. In particular, efforts have been made to reduce the losses associated with AWGs used in the dense wavelength combining stage. The following sections present the architecture for this multi-frequency high-brightness laser, discuss materials for broadband and low-loss operation, review demonstrations of lasers on Si with different wavelengths, and present integrated wavelength combining devices compatible with these lasers on Si.

2.2 Integrated beam combining

An ultra-broadband multi-spectral laser on Si is feasible with existing technology to heterogeneously integrate lasers on Si by direct wafer bonding [14, 15]. This fully integrated device is schematized in Fig. 2.1, showing presently demonstrated spectral bands of lasers on Si at 1.3-µm [6, 11], 1.5-µm [4, 9], 2.0-µm [12, 16], and 4.8-µm [13, 17] wavelengths, based on indium phosphide (InP). Active devices based on gallium arsenide (GaAs) have also been integrated with Si_3N_4 at 1.0-µm [10] and at 1.5-µm [18]. The spectral bands at 0.4-µm and 3.6-µm wavelengths will be realized with gallium nitride (GaN) and gallium antimonide (GaSb) based materials, respectively.

The multi-octave spectral beam combiner, in Fig. 2.1, is designed to be compatible with multiple arrays of heterogeneously integrated diode lasers where each laser operates at a different wavelength and each array covers a different spectral band. A first stage of intra-band combiners multiplexes light with arrayed waveguide gratings (AWGs) [19], to combine each laser output within a spectral band into a single single-mode waveguide. A second stage of directional couplers is used to combine all of the spectral bands within each waveguide type. Before the final ultra-broadband combiner stage, optical modes in the Si core waveguide are transferred to the Si_3N_4 core waveguide [18, 20]. The two waveguides resulting from each waveguide platform are then input to the ultra-broadband combiner.

Spectral beam combining of each laser wavelength to a single output waveguide is achieved by several stages from dense to coarse wavelength division multiplexing (WDM). There is no inherent loss to combining. Note that AWGs efficiently combine light both for the dense WDM and for the coarse WDM with more than two channels. Adiabatic couplers can be designed to combine light for coarse WDM with just two inputs. Lasers with wavelengths longer than ∼1.1 µm are integrated on Si waveguides, while shorter

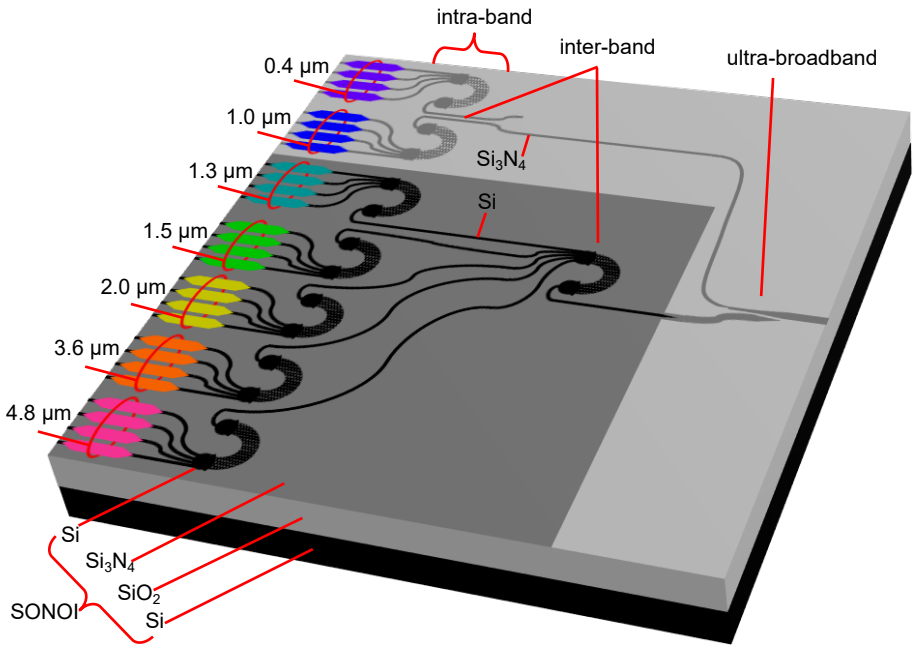

Figure 2.1: Architecture for a multi-spectral laser on Si, spanning the UV to the mid-IR [8].

wavelength lasers are on Si_3N_4 waveguides. The final ultra-broadband combining stage has been demonstrated [8] to combine light from the visible (0.76 µm) to the mid-IR (3.6 µm) with high fundamental mode transmission. Furthermore, simulations show efficient operation in the range of 0.35–6.7 µm, however, this was not verified due to limited availability of optical sources. To obtain high brightness, every element of this PIC must be efficient. For the lasers, high wall-plug efficiency and output power are critical figures-of-merit. SOAs may also be included to boost the power of each spectral band. The beam combining elements must have low on-chip loss and transmit light to the fundamental modes of each wavelength in a single output waveguide.

Examples of the waveguide mode sizes are simulated in Fig. 2.2 for wavelengths in the range of 0.35–4.50 µm. Wavelengths shorter than 1.1 µm are guided with the nitride-on-insulator (NOI) platform and those longer than 1.1 µm are guided with the Si-on-nitride-on-insulator (SONOI). Each mode is plotted on a scale of 2.5 µm height and 8.0 µm width. This highlights the challenge of bringing all of these wavelengths to a single ultra-

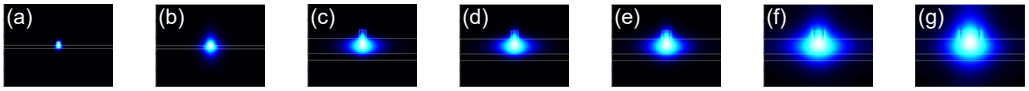

Figure 2.2: Mode simulations for NOI waveguides at (a) 350 nm and (b) 780 nm wavelengths. SONOI simulations are shown at (c) 1.30 µm, (d) 1.55 µm, (e) 2.10 µm, (f) 3.70 µm, and (c) 4.50 µm wavelengths.

broadband output waveguide. This final output waveguide needs to be large enough to confine the longest wavelengths and small enough to limit the number of higher order modes for the shortest wavelengths. Of course, this requires compromises for each: the longest wavelengths may experience substrate leakage loss and the shortest wavelengths may excite higher-order modes that decrease the beam quality.

The brightness (B) is defined by the output power (P) and the beam quality factor (M^2) as: $B = P/M^2$. The transverse divergence angles ($\theta_\perp$ and $\theta_\parallel$) can be expressed from the diffraction-limited divergence angles ($\theta_{\perp,0}$ and $\theta_{\parallel,0}$) modified by the beam quality factors ($M_\perp^2$ and $M_\parallel^2$): $\theta_\perp = \theta_{\perp,0} M_\perp^2$ and $\theta_\parallel = \theta_{\parallel,0} M_\parallel^2$. Both angles can be combined from the geometric mean: $M^2 = M_\perp M_\parallel$. The total degradation to the beam quality from multiple ($\mathcal{N}$) elements in an optical system is calculated from the quadrature combination as $M^2_{\text{total}} = \sqrt{\sum_{x=1}^{\mathcal{N}} (M_x^2)^2}$ [1], as long as the elements are not correlated, *i.e.*, each element independently degrades the beam quality. The ideal condition of $M^2 = 1.0$ is achieved by tailoring the output optical mode of the laser to have an exactly Gaussian-shaped intensity profile in the vertical and the horizontal orientations. For this reason, the passive beam-combining elements must transmit a high percentage of input light to the output fundamental mode. Additionally, the output waveguide must be able to support Gaussian-shaped modes throughout the bandwidth of the multi-spectral optical sources.

2.3 Heterogeneous lasers

In this section, the current spectral capabilities of heterogeneous lasers on Si are motivated and discussed. Fabrication for lasers and amplifiers at each spectral band follows a similar process, schematized in Fig. 1.1. More detailed processing information can be found in a recent manuscript about distributed feedback (DFB) lasers on Si [21]. Laser performance is reviewed at each wavelength and compared by the threshold currents, maximum output powers, and temperature dependencies.

2.3.1 Lasers at 1.31-µm on Si

One of the early demonstrations of the heterogeneously integrated laser operates at 1.31-µm wavelength with an InP-based gain material [11]. A maximum output power of 32 mW is reported with a 35-mA threshold current at room temperature. Continuous-wave (CW) lasing up to 105 °C is observed. More recently, improved performance is shown with an 18-mA threshold current, 35-mW CW output power, and a wall-plug efficiency of 14 % [22]. The gain region length is only 700 µm and higher output power is expected for a design with a longer gain region. Simultaneous operation of 16 lasers arrayed on the same chip is demonstrated. This spectral band has the most mature technology for fabrication and packaging [23]. Also, 1.31-µm lasers are typically more efficient that 1.55-µm lasers, because of lower intervalence band absorption [24] and reduced Auger recombination [25].

2.3.2 Lasers and SOAs at 1.55-µm on Si

Since the first electrically pumped laser on Si was demonstrated [4], there has been significant focus and development to improve performance and advance this technology for large scale integration to drive down the cost of optical communication systems.

The most complex PICs using heterogeneous integration are at this wavelength [7]. A recent demonstration at 1.55-µm details design optimization and performance for SOAs and lasers [9]. This work exemplifies a unique property of the heterogeneously integrated lasers and SOAs: the optical confinement is controlled lithographically by the Si waveguide width, independent of the current injection width or active region alterations. As a result, SOAs fabricated on the same chip may be designed with different values of gain and output saturation power. On-chip gain is demonstrated in the range 11–26 dB, controlled by the Si waveguide width and corresponding to input saturation powers as high as 4 dBm. Operation over a wide bandwidth shows how a single SOA can amplify multi-spectral light following the intra-band combiner stage in Fig. 2.1.

Prior to the application of the anti-reflective (AR) coating to the SOAs, the devices lase from the Si-waveguide facet reflections. Output power is measured up to 42 mW. The thermal impedance is 11 K/W [9], which is comparable to similar diodes on InP. Due to the high thermal conductivity of Si (1.56 $\mathrm{W{\cdot}cm^{-1}{\cdot}K^{-1}}$), [26] lateral heat spreading in the Si waveguide layer is responsible for this low thermal impedance. By defining a wide mesa of 26 µm, the III–V is in contact with ∼10 µm of the Si on both sides of the Si waveguide trench. Heat generated in the active region then has a low impedance path to this Si layer. Again, higher power is expected for longer gain region lengths.

A common challenge of heterogeneously integrated lasers is to produce an efficient optical mode converter between the gain and the passive waveguide regions. This taper efficiency (l_t) has a maximum value of −0.25 dB and increases as the wavelength increases. It is extracted from two similar lasers with different gain (g_1 and g_2), different gain-region lengths L_1 and L_2, and a passive waveguide loss ($\alpha_\mathrm{Si} \approx 50$ dB/m) as:

$$l_\mathrm{t} \equiv \frac{L_1 g_2 - L_2 g_1}{2\,(L_2 - L_1)} - \alpha_\mathrm{Si} L_2\,. \tag{2.1}$$

Note that this relation depends on the wavelength and the current density. By accurately characterizing the taper loss, designs can be optimized for lasers at each wavelength for the multi-spectral laser.

2.3.3 Lasers and SOAs at 2.0-µm on Si

Si exhibits both a low two-photon absorption coefficient and a high Kerr coefficient at ∼2.0-µm wavelength [27]. Therefore, low waveguide propagation loss is expected in this spectral band. Also, Si provides a power-efficient platform for chip-level applications in non-linear optics [28–30], including comb generation and on-chip doubling [31], so PICs with integrated 2.0-µm active devices are highly desired.

Recently, the first laser operating at 2-µm wavelength on Si was demonstrated [12]. The first ever reported 2-µm SOA was also demonstrated on Si [16]. These devices consist of GaInAs quantum wells (QWs) bonded on top of a Si waveguide. The hybrid optical mode is laterally confined by the Si waveguide, while a portion of the mode overlaps the active region. The III–V mesa is terminated on both sides by a lateral taper, causing the hybrid active mode to couple into a passive Si waveguide mode. A Fabry–Perot cavity is then formed by the polished Si facets for the lasers, and they are AR coated to form the SOAs. The laser output power has emission up to 4.2 mW from a single facet with a ∼122-mA threshold current. CW lasing is observed up to 35 °C. A maximum gain of 13-dB is observed and gain is demonstrated up to 50 °C.

2.3.4 Lasers at 4.8-µm on Si

Light of longer wavelengths than 3 µm can be exploited for numerous sensing and detection applications. Chemical bond spectroscopy [32], environmental monitoring, and remote sensing [33] can potentially be addressed on an integrated Si platform.

Low-cost, versatile, and complex technologies can be enabled by integrating multiple sensors on one Si chip. However, room-temperature InP-based type-I diode lasers have only been reported up to ∼2.4 µm [34]. Alternatively, GaSb-based interband cascade lasers (ICL) and InP-based quantum cascade lasers (QCL) are promising candidates for extending heterogeneous integration to wavelengths throughout the mid-IR (3.0–8.0 µm). QCLs operate from 3.0 µm to the terahertz regime and can emit watts of CW output power [35, 36].

Last year, the first QCLs integrated on Si were demonstrated with operation at a wavelength near 4.8 µm [13]. These lasers utilize a III–V active mesa bonded to Si and tapered at both ends to transfer light into passive Si waveguides. A cross-sectional schematic of the active region of a heterogeneously integrated QCL is shown in Fig. 2.3(a). Due to the high material absorption of SiO_2, the traditionally-used SOI platform is not ideal for mid-IR Si photonic integration. The QCLs are therefore integrated on the SONOI waveguide platform, which should permit transmission of the wavelength range 1.1–6.7 µm.

The first integrated QCLs include a Fabry–Perot laser cavity, operated in pulsed mode at room temperature, and exhibit threshold currents as low as 387 mA and output powers up to 31 mW per facet. Subsequent advancements are demonstrated with DFB lasers, which employ a $\lambda/4$-shifted grating on top of Si waveguides within the active region [17]. These wavelength-selective devices emit over 200 mW from a single facet after removing the III–V taper. This verifies that high power and low threshold QCLs can be integrated on Si with improved taper design. In Fig. 2.3(b) the light output versus drive current for an integrated DFB QCL is shown operating at temperatures from 10 °C to 100 °C. A far-field measurement, shown in Fig. 2.4, demonstrates a fundamental-mode output. These results open the opportunity to build a wide range of fully-integrated sensors and detectors on Si operating with wavelengths throughout the mid-IR.

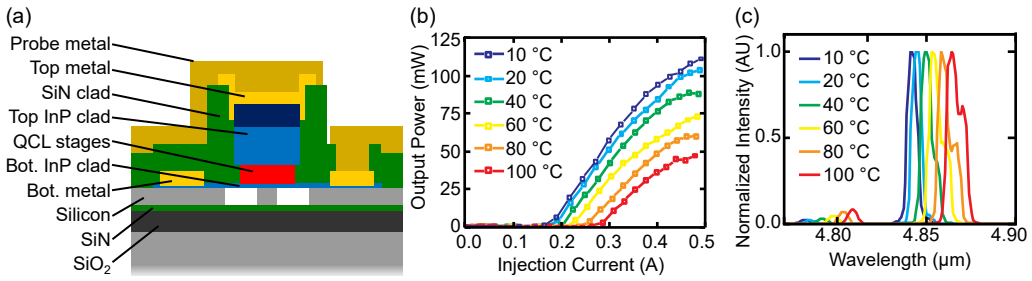

Figure 2.3: DFB QCL on SONOI (a) cross-sectional diagram, (b) LIV temperature dependence, and (c) spectrum temperature dependence [17].

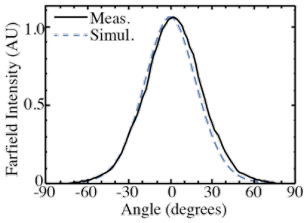

Figure 2.4: Farfield plot from the DFB QCL on SONOI [17].

2.4 Multi-spectral photonic integrated circuit

This section describes the passive wavelength beam combining devices for integration with each of the different laser spectral bands. In particular, devices for dense and course WDM are reviewed to present how the intra-band, inter-band, and ultra-broadband stages in Fig. 2.1 are realized.

2.4.1 Dense WDM

For the range of wavelengths generated from a single gain material, a dense WDM device will combine each laser output to a single waveguide. AWGs provide the most efficient spectral beam combining for dense spectral spacing. Measurement results for AWGs operating near 0.76-μm, 1.55-μm, and 2.0-μm wavelengths are reviewed and a recently fabricated AWG at 3.6-μm is shown in this sub-section.

Low-loss AWGs are achieved by minimizing loss contributions from waveguide propagation, width transitions, and bend radius transitions. Phase errors in the arrayed waveguides must also be minimized. Additionally, the waveguide array in the AWG must have low side-order excitation. All of these design aspects become more problematic for shorter wavelengths compared AWGs commonly made in the near-IR for communication applications. For bulk material, Rayleigh scattering dominates, which is proportional to λ^{-4} [37], and for waveguides, interfacial scattering dominates, having a similar wavelength dependence [38, 39]. Phase errors arise due to lithography inaccuracies (from mask writing or photoresist exposure), waveguide interfacial roughness, or non-uniformities in the waveguide thickness and in the etch. These fabrication-related limitations have greater effect at reduced wavelengths.

To optimize our design tools, an AWG near 0.76-µm wavelength is demonstrated [40] before attempting longer wavelength AWGs. The waveguide core is Si_3N_4 and cladding is SiO_2, consistent with the SONOI platform. A record low loss of <0.5 dB and crosstalk level of −25 dB is reported. The on-chip transmission data and model show good agreement within the ∼20-dB peak channel bandwidths. However, the crosstalk level of the model is about 5 dB lower than the data. This is attributed to fabrication variations, such as waveguide thickness and etch non-uniformities, that are not included in the model.

Recently, AWGs near 1.55-µm and 2.0-µm wavelengths have been demonstrated on SOI with eight channels. The 1.55-µm AWG is reported with <1.6 dB of loss and about −29 dB of crosstalk [41]. Preliminary measurements of the 2.0-µm AWG reveals a low loss of <1.0 dB and crosstalk at about −28 dB. Also, a 3.6-µm wavelength AWG has been designed on SOI. Future work will compare the performance of these AWG demonstrations on SOI to similar designs on SONOI. This will indicate if loss decreases

with SONOI due to the reduced material absorption of Si_3N_4 compared to SiO_2 or if excess loss arises from the additional material interfaces.

2.4.2 Coarse WDM

Inter-band combiners are either realized with adiabatic couplers or AWGs. The adiabatic coupler serves as a wavelength combiner with two inputs and one output, operating over spectral ranges spanning multiple octaves. These duplexers can achieve very low loss, only limited by the waveguide propagation loss (<0.05 dB). AWGs can combine more spectral channels, however, the loss is higher (∼1.0 dB) and the bandwidth is narrower.

The final combiner stage must be *ultra*-broadband, guiding and combining wavelengths that span more than four octaves to converge the each laser output into a single waveguide. The efficiency of fundamental mode excitation at each wavelength is important because this determines the output beam quality and affects the brightness (B) of the multi-spectral laser. A modified adiabatic coupler has been demonstrated to meet these specifications [8]. One input to this combiner supports the short wavelengths and the other the long wavelengths. A narrow spectral region near 1.55-µm exhibits decreased transmission with a maximum loss of 3.0 dB. Less than 0.5-dB loss is found between 0.35-µm to 1.3-µm for one input and 1.9-µm to 6.5-µm light for the other. The center of the low-transmission region can be tuned by changing the length of the coupler, which is independent of the operating bandwidth.

2.5 Summary and conclusions

Each element of the high-brightness multi-spectral laser on Si has been demonstrated and a path towards complete integration is feasible. High powered lasers spanning the

near-IR to the mid-IR are integrated on Si. Low-loss beam combining elements are realized at corresponding wavelengths to the optical sources, paving the way for full-system integration. Remaining challenges for this multi-spectral PIC are to improve laser wall-plug efficiencies and to develop a fabrication process for simultaneous integration of InP with other gain materials. This technology is important to enable fully-integrated multi-spectral lasers for highly attuned gas sensors, infrared counter-measures, ultra-broadband WDM optical communications, and industrial processing. Fabrication of this device is scalable and would drastically reduce the cost compared to technologies with similar performance.

References

[1] A. Siegman, "Analysis of laser beam quality degradation caused by quartic phase aberrations," Appl. Opt. **32**, 5893–5901 (1993).

[2] R. Paschotta, "Beam quality deterioration of lasers caused by intracavity beam distortions," Opt. Express **14**, 6069–6074 (2006).

[3] T. Y. Fan, "Laser beam combining for high-power, high-radiance sources," IEEE J. Sel. Topics Quantum Electron. **11**, 567–577 (2005).

[4] A. W. Fang, H. Park, O. Cohen, R. Jones, M. J. Paniccia, and J. E. Bowers, "Electrically pumped hybrid AlGaInAs-silicon evanescent laser," Opt. Express **14**, 9203–9210 (2006).

[5] D. Liang and J. E. Bowers, "Recent progress in lasers on silicon," Nat. Phot. **4**, 511–517 (2010).

[6] H.-H. Chang, Y.-h. Kuo, R. Jones, A. Barkai, and J. E. Bowers, "Integrated hybrid silicon triplexer," Opt. Express **18**, 23891–23899 (2010).

[7] C. Zhang, S. Zhang, J. D. Peters, and J. E. Bowers, "8×8×40 Gbps fully integrated silicon photonic network on chip," Optica **3**, 785–786 (2016).

[8] E. J. Stanton, M. J. Heck, J. Bovington, A. Spott, and J. E. Bowers, "Multi-octave spectral beam combiner on ultra-broadband photonic integrated circuit platform," Opt. Express **23**, 11272–11283 (2015).

[9] M. L. Davenport, S. Skendžić, N. Volet, J. C. Hulme, M. J. Heck, and J. E. Bowers, "Heterogeneous Silicon/III–V Semiconductor Optical Amplifiers," IEEE J. Sel. Topics Quantum Electron. **22**, 78–88 (2016).

[10] J. T. Bovington, M. J. R. Heck, and J. E. Bowers, "Heterogeneous lasers and coupling to Si_3N_4 near 1060 nm," Opt. Lett. **39**, 6017–6020 (2014).

[11] H.-H. Chang, A. W. Fang, M. N. Sysak, H. Park, R. Jones, O. Cohen, O. Raday, M. J. Paniccia, and J. E. Bowers, "1310nm silicon evanescent laser," Opt. Express **15**, 11466–11471 (2007).

[12] A. Spott, M. Davenport, J. Peters, J. Bovington, M. J. R. Heck, E. J. Stanton, I. Vurgaftman, J. Meyer, and J. Bowers, "Heterogeneously integrated 2.0 µm CW hybrid silicon lasers at room temperature," Opt. Lett. **40**, 1480–1483 (2015).

[13] A. Spott, J. Peters, M. L. Davenport, E. J. Stanton, C. D. Merritt, W. W. Bewley, I. Vurgaftman, C. S. Kim, J. R. Meyer, J. Kirch, L. J. Mawst, D. Botez, and J. E. Bowers, "Quantum cascade laser on silicon," Optica **3**, 545–551 (2016).

[14] D. Liang, A. W. Fang, H. Park, T. E. Reynolds, K. Warner, D. C. Oakley, and J. E. Bowers, "Low-Temperature, Strong SiO_2-SiO_2 Covalent Wafer Bonding for III–V Compound Semiconductors-to-Silicon Photonic Integrated Circuits," J. Electron. Mater. **37**, 1552–1559 (2008).

[15] D. Liang, D. C. Chapman, Y. Li, D. C. Oakley, T. Napoleone, P. W. Juodawlkis, C. Brubaker, C. Mann, H. Bar, O. Raday *et al.*, "Uniformity study of wafer-scale InP-to-silicon hybrid integration," Appl. Phys. A Mater. Sci. Process. **103**, 213–218 (2011).

[16] N. Volet, A. Spott, E. J. Stanton, M. L. Davenport, L. Chang, J. D. Peters, T. C. Briles, I. Vurgaftman, J. R. Meyer, and J. E. Bowers, "Semiconductor optical amplifiers at 2.0-µm wavelength on silicon," Laser Photon. Rev. **11**, 1600165 (2017).

[17] A. Spott, J. Peters, M. L. Davenport, E. J. Stanton, C. Zhang, C. D. Merritt, W. W. Bewley, I. Vurgaftman, C. S. Kim, J. R. Meyer, J. Kirch, L. J. Mawst, D. Botez, and J. E. Bowers, "Heterogeneously Integrated Distributed Feedback Quantum Cascade Lasers on Silicon," Photonics **3**, 35 (2016).

[18] M. Piels, J. F. Bauters, M. L. Davenport, M. J. R. Heck, and J. E. Bowers, "Low-loss silicon nitride AWG demultiplexer heterogeneously integrated with hybrid III–V/silicon photodetectors," J. Lightw. Technol. **32**, 817–823 (2014).

[19] G. Kurczveil, M. J. R. Heck, J. D. Peters, J. M. Garcia, D. Spencer, and J. E. Bowers, "An integrated hybrid silicon multiwavelength AWG laser," IEEE J. Sel. Topics Quantum Electron. **17**, 1521–1527 (2011).

[20] J. F. Bauters, M. L. Davenport, M. J. R. Heck, J. K. Doylend, A. Chen, A. W. Fang, and J. E. Bowers, "Silicon on ultra-low-loss waveguide photonic integration platform," Opt. Express **21**, 544–555 (2013).

[21] C. Zhang, S. Srinivasan, Y. Tang, M. J. Heck, M. L. Davenport, and J. E. Bowers, "Low threshold and high speed short cavity distributed feedback hybrid silicon lasers," Opt. Express **22**, 10202–10209 (2014).

[22] B. R. Koch, E. J. Norberg, B. Kim, J. Hutchinson, J.-H. Shin, G. Fish, and A. Fang, "Integrated silicon photonic laser sources for telecom and datacom," in "National Fiber Optic Engineers Conference," (OSA, 2013), pp. Paper PDP5C–8.

[23] H.-F. Liu, "Integrated silicon photonics links for high bandwidth data transportation," in "Optical Fiber Communication Conference," (OSA, 2014), p. Paper Th1D.1.

[24] H. C. Casey Jr. and P. L. Carter, "Variation of intervalence band absorption with hole concentration in p-type InP," Appl. Phys. Lett. **44**, 82–83 (1984).

[25] N. Volet and E. Kapon, "Turn-on delay and Auger recombination in long-wavelength vertical-cavity surface-emitting lasers," Appl. Phys. Lett. **97**, 131102 (2010).

[26] C. J. Glassbrenner and G. A. Slack, "Thermal conductivity of silicon and germanium from 3°K to the melting point," Phys. Rev. **134**, A1058 (1964).

[27] A. D. Bristow, N. Rotenberg, and H. M. Van Driel, "Two-photon absorption and Kerr coefficients of silicon for 850–2200 nm," Appl. Phys. Lett. **90**, 191104 (2007).

[28] M. A. Foster, A. C. Turner, J. E. Sharping, B. S. Schmidt, M. Lipson, and A. L. Gaeta, "Broad-band optical parametric gain on a silicon photonic chip," Nature **441**, 960–963 (2006).

[29] S. Zlatanovic, J. S. Park, S. Moro, J. M. C. Boggio, I. B. Divliansky, N. Alic, S. Mookherjea, and S. Radic, "Mid-infrared wavelength conversion in silicon waveguides using ultracompact telecom-band-derived pump source," Nat. Photon. **4**, 561–564 (2010).

[30] P. Del'Haye, T. Herr, E. Gavartin, M. Gorodetsky, R. Holzwarth, and T. J. Kippenberg, "Octave spanning tunable frequency comb from a microresonator," Phys. Rev. Lett. **107**, 063901 (2011).

[31] L. Chang, Y. Li, N. Volet, L. Wang, J. Peters, and J. E. Bowers, "Thin film wavelength converters for photonic integrated circuits," Optica **3**, 531–535 (2016).

[32] L. S. Rothman, I. E. Gordon, Y. Babikov, A. Barbe, D. C. Benner, P. F. Bernath, M. Birk, L. Bizzocchi, V. Boudon, L. R. Brown, A. Campargue, K. Chance, E. A. Cohen, L. H. Coudert, V. M. Devi, B. J. Drouin, A. Fayt, J.-M. Flaud, R. R. Gamache, J. J. Harrison, J.-M. Hartmann, C. Hill, J. T. Hodges, D. Jacquemart, A. Jolly, J. Lamouroux, R. J. L. Roy, G. Li, D. A. Long, O. M. Lyulin, C. J. Mackie, S. T. Massie, S. Mikhailenko, H. S. P. Muller, O. V. Naumenko, A. V. Nikitin, J. Orphal, V. Perevalov, A. Perrin, E. R. Polovtseva, C. Richard, M. A. H. Smith, E. Starikova, K. Sung, S. Tashkun, J. Tennyson, G. C. Toon, V. G. Tyuterev, and G. Wagner, "The HITRAN2012 molecular spectroscopic database," J. Quant. Spectrosc. Radiat. Transfer **130**, 4–50 (2013).

[33] J. W. Salisbury and D. M. D'Aria, "Emissivity of terrestrial materials in the 3–5 µm atmospheric window," Remote Sens. Environ. **47**, 345–361 (1994).

[34] Y. Gu, Y. Zhang, Y. Cao, L. Zhou, X. Chen, H. Li, and S. Xi, "2.4 µm InP-based antimony-free triangular quantum well lasers in continuous-wave operation above room temperature," Appl. Phys. Express **7**, 032701 (2014).

[35] Y. Bai, N. Bandyopadhyay, S. Tsao, S. Slivken, and M. Razeghi, "Room temperature quantum cascade lasers with 27% wall plug efficiency," Appl. Phys. Lett. **98**, 181102 (2011).

[36] Y. Yao, A. J. Hoffman, and C. F. Gmachl, "Mid-infrared quantum cascade lasers," Nat. Photon. **6**, 432–439 (2012).

[37] J. W. Strutt, "On the light from the sky, its polarization and colour," Philos. Mag. **41**, 107–120 (1871).

[38] J. F. Bauters, M. J. Heck, D. John, D. Dai, M.-C. Tien, J. S. Barton, A. Leinse, R. G. Heideman, D. J. Blumenthal, and J. E. Bowers, "Ultra-low-loss high-aspect-ratio Si_3N_4 waveguides," Opt. Express **19**, 3163–3174 (2011).

[39] T. Barwicz and H. A. Haus, "Three-dimensional analysis of scattering losses due to sidewall roughness in microphotonic waveguides," J. Lightw. Technol. **23**, 2719 (2005).

[40] E. Stanton, A. Spott, M. Davenport, N. Volet, and J. Bowers, "Low-loss arrayed waveguide grating at 760 nm," Opt. Lett. **41**, 1785–1788 (2016).

[41] E. J. Stanton, N. Volet, and J. E. Bowers, "Low-loss demonstration and refined characterization of silicon arrayed waveguide gratings in the near-infrared," Opt. Express **25**, 30651–30663 (2017).

Chapter 3

Waveguide platform

3.1 Introduction

Choosing the appropriate waveguide platform is the essential starting point for any photonic design. There are many factors to consider that affect performance, size, cost, and fabrication time of the device. As with any type of design, compromises must be made to balance these aspects, and these design choices depend on the specific type of photonic device. In the case of the multi-spectral laser, desired features for the waveguide platform include low-loss waveguides with low scattering, efficient mode transfer from the hybrid active region to the passive waveguide, compact modes with small bend radii, and a high beam quality output.

Materials to form the waveguide core, waveguide cladding[1], and substrate must be chosen first. Because of the infrastructure investments in Si manufacturing for electronics, there is incentive to use Si substrates to decrease cost. Also, there are performance advantages, including low-loss waveguides and precise feature control, thanks to the mature process quality and uniformity. The most standard Si-photonic

[1]This includes the top, bottom, and side claddings, which can be different materials.

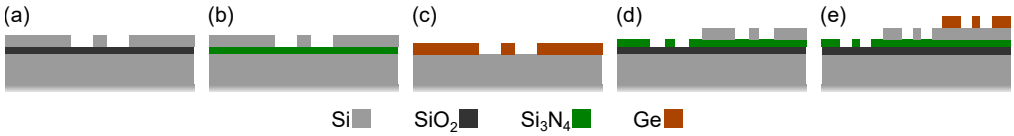

Figure 3.1: Schematics of (a) SOI, (b) SON, (c) GOS, (d) SONOI, and (e) GOSONOI waveguide platforms.

waveguide platform is SOI, shown in Fig. 3.1(a). Other waveguide platforms that have been demonstrated on Si substrates include the Si-on-nitride (SON) in Fig. 3.1(b) and Germanium-on-Si (GOS) in Fig. 3.1(c). The lowest on-chip propagation loss was demonstrated using the nitride-on-insulator (NOI) platform [1].

Investigation into waveguides for low-loss mid-IR transmission has shown that Si can guide light from the near-IR (∼1.1-µm) to the mid-IR (∼7.0-µm) with low absorption loss [2–4]. SiO_2 and Si_3N_4 are commonly integrated on Si and can be layered to create multiple waveguide cores in the same platform. These materials have transmission windows in the wavelength ranges of 0.35–3.5-µm and 0.35–6.7-µm, respectively, according to [3, 5]. From this information, a waveguide platform with layers of Si, Si_3N_4, and SiO_2 on a Si substrate, called Si-on-nitride-on-insulator (SONOI) is constructed [6–8] and depicted in Fig. 3.1(d). By defining waveguides in the top Si layer and depositing an upper cladding of Si_3N_4, light from ∼1.1-µm to ∼6.7-µm wavelengths is efficiently guided. In other areas of the same chip, the top Si layer is removed and waveguides with Si_3N_4 core and SiO_2 cladding are defined to support ∼0.4-µm to ∼3.5-µm wavelengths. For longer wavelengths in the mid-IR, $Si_{1-x}Ge_x$ waveguides can transmit light with low-loss from 1.9-µm, to 16.7-µm [3, 9, 10]. This can potentially be integrated with the SONOI platform by adding the $Si_{1-x}Ge_x$ on top of the Si waveguide layer as shown in Fig. 3.1(e).

This chapter discusses the general design, simulation, fabrication, and characterization of waveguides for the multi-spectral laser platform. These steps are applied to

waveguides for demonstrations of AWGs, star couplers, broadband combiners, and multi-spectral QCLs in the following chapters.

3.2 Design

The SONOI platform uses two waveguide types to avoid prohibitively high material losses that would be present in a single waveguide platform for UV to mid-IR wavelengths. It also provides a platform compatible with heterogeneous integration of laser sources covering the same spectral range. In general, multiple waveguide platforms can be integrated together by layering materials with progressively larger refractive indices. Adiabatic tapers can be used transition between waveguide types.

Waveguide geometries can either be dual layer buried rib type, as in Fig. 3.1(d–e), or a single layer buried channel type in order to manage waveguide modes and increase the tolerance of the waveguide effective index against process variations, respectively. For the SONOI waveguide platform, a cross-over wavelength of ∼1.8 µm is chosen such that longer wavelengths are guided by a Si core with Si_3N_4 cladding waveguide and shorter wavelengths are guided by a Si_3N_4 core with SiO_2 cladding waveguide. This provides an ultra-broadband spectral transparency from UV to mid-IR. Si absorption in the UV, VIS, and near-IR bands is avoided by using Si_3N_4 and SiO_2 (down to ∼350nm) and SiO_2 absorption in the mid-IR band (up to ∼6.5 µm) is avoided by using Si and Si_3N_4 [5, 11]. Significant mid-IR optical absorption in SiO_2 increases loss after the transition from the Si waveguide to the Si_3N_4 waveguide, both shown in Fig. 3.1(d), but it is feasible to minimize the waveguide length and keep absorption loss below 1 dB. Other approaches could be used to avoid absorption loss, for example by etching away the SiO_2 underneath the Si_3N_4, leading to a membrane type waveguide [3]. For mid-IR wavelengths in the Si_3N_4 core waveguide, Si substrate leakage also contributes significant loss. Although

substrate leakage loss is not addressed in this work, a fabrication experiment is tested on these devices to investigate undercut etching the Si substrate below the Si_3N_4 waveguide platform in regions that guide mid-IR light. This reduces substrate leakage loss for mid-IR wavelengths and it should not affect loss at shorter wavelengths.

The Si_3N_4 waveguide platform must ultimately guide all of the spectrally combined light across the entire UV to mid-IR spectrum during the ultra-broadband combiner stage and the final output waveguide. Therefore, this waveguide platform must also provide low loss for NIR to mid-IR wavelengths as well as UV to NIR wavelengths. By employing a high aspect ratio of width to thickness, the sidewall scattering loss can be minimized [1, 12]. Substrate leakage and material absorption losses for mid-IR wavelengths can be minimized as previously discussed through Si substrate undercut and minimizing the length of the final ultra-broadband combiner and output waveguide region.

3.2.1 Scattering loss

One of the primary sources of loss for integrated waveguides comes from interfacial scattering. For decades, this effect has been studied, modeled, simulated, and experimentally investigated. Rigorous tools have been developed to calculate scattering using mode simulations and interfacial roughness models based on the position deviation along an interface. An exponential fit to the auto-covariance of this deviation is used to extract the root-mean-square (RMS) roughness and the correlation length. The scattering loss simulation and waveguide designs used in this work are clearly detailed in [13]. Mode simulations are performed with FIMMWAVE using a python scripting interface [14]. Electric and magnetic field amplitudes at the material interfaces are computed as in [15].

3.2.2 Absorption

Only recently has the absorption loss of a waveguide platform been the limiting factor for reducing loss [1]. Propagation losses below 100 dB/m are typically considered "low-loss" and sometimes loses below 10 dB/m are called "ultra-low-loss". Accurate knowledge of material absorption is necessary to design for ultra-low-loss waveguides.

Absorption loss for Si [2–4], SiO_2 [16, 17], and Si_3N_4 [18] are plotted in Fig. 3.2. Other literature searches have concluded that absorption loss in SiO_2 is higher than in Si_3N_4 in the mid-IR near 3–6 µm, even claiming transparency for Si_3N_4 up to 6.7-µm wavelength [3, 5]. The data presented in Fig. 3.2 referenced from the original material absorption measurements. Although these are molecularly the same materials, the forms of SiO_2 and Si_3N_4 are different from the thin films integrated on Si substrates. It is evident that Si_3N_4 does not have lower loss than SiO_2 in the mid-IR. The loss of these two materials are very similar and likely depend greatly on the impurities due to the growth or deposition technique. Also, a thorough investigation of Si, SiO_2, and Si_3N_4 absorption for high-quality thin-films like those used in NOI and SOI waveguide platforms is lacking in scientific literature.

3.2.3 Indices

Simulations throughout this work incorporate experimental refractive index values from thin film materials, when available, and literature values when this data is not available. The Sellmeier coefficients for calculating refractive indices of Si, SiO_2, Si_3N_4, and InP are listed in Table 3.1 and the corresponding equation is [20]:

$$n^2(\lambda) = A + \sum_m \frac{B_m}{1 - (C_m/\lambda)^2}\,. \tag{3.1}$$

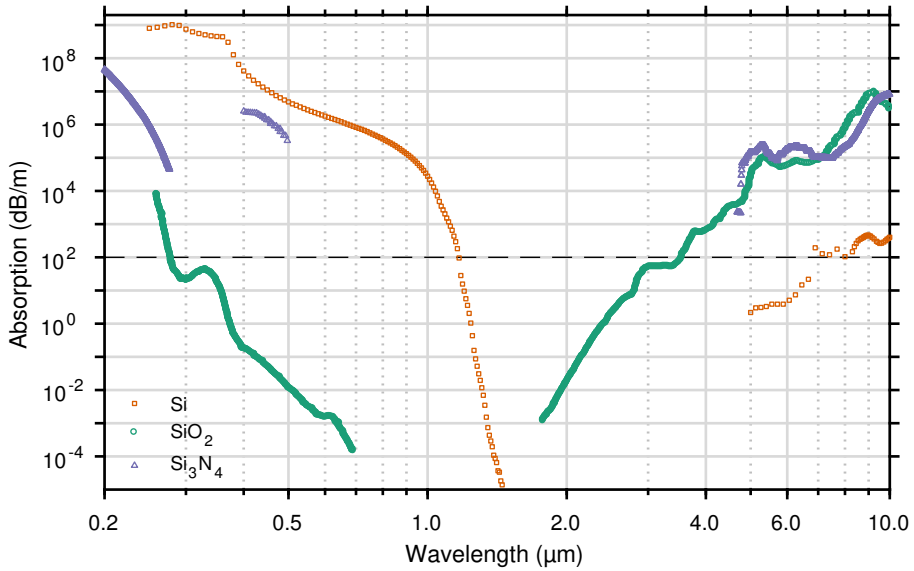

Figure 3.2: Absorption spectra of Si ($\lambda < 1.45$ µm [2], 5.00 µm $< \lambda <$ 8.30 µm [3], and $\lambda >$ 8.30 µm [4]), SiO_2 ($\lambda <$ 0.69 µm [16] and $\lambda >$ 1.78 µm [17]), and Si_3N_4 ($\lambda <$ 0.28 µm [18], 0.40 µm $< \lambda <$ 0.50 µm [19], and $\lambda >$ 4.67 µm [19]).

Although these parameters are found phenomenologically, they do have physical significance, aside from the A coefficient, which is used as an offset to improve the fit. The C coefficient corresponds to a strong absorption resonance wavelength and the B coefficients for the same m are scale factors related to the strength of the resonance. This equation is generally more accurate than the Cauchy equation. The Sellmeier equation can model anomalous dispersion and is valid for nearly the entire transparent range of a material, while neither is true for the Cauchy equation. Accurate values of material refractive indices are important for mode simulations across all wavelengths in this ultra-broadband design. Small deviations in modeled indices significantly shift the AWG channels and the cross-over wavelengths of adiabatic couplers. To optimize these devices, design and fabrication iterations must be performed to exactly match the modeled and actual indices.

Table 3.1: Sellmeier coefficients of materials used in simulations. The right column shows the valid wavelength range λ. Coefficients A and B are dimensionless, while coefficient C and λ are in units of µm.

Material	A	B_1	B_2	B_3	C_1	C_2	C_3	λ
Si [21]	1.000	10.6684	0.0030	1.5413	0.3015	1.1348	1104	1.36–11.0
SiO_2 [22]	1.000	0.6962	0.4079	0.8975	0.0684	0.1162	9.896	0.21–6.70
Si_3N_4 [23]	1.000	3.0249	40314	-	0.1353	1240	-	0.31–5.50
Ge [21]	1.000	14.7587	0.2353	−24.8823	0.4343	1.2625	1302	2.06–13.0
InP [24]	7.255	2.316	2.765	-	0.6263	32.935	-	0.95–10.0

3.3 Fabrication

Fabrication is the dominant factor driving the broad adoption of a waveguide platform. SOI is a good example of a waveguide platform that can be fabricated on a large scale with low impurities and interfacial roughness. These attributes have driven demand, decreased the cost, and increased the acceptance of this platform. The electronics industry originally drove this demand since SOI is used to make device with low parasitic capacitance. This section highlights some important but general fabrication considerations. More specific fabrication processes are presented alongside the device demonstration sections.

Large wafer diameters, such as 400 mm, are more common in the photonics industry because of the smaller unit-area cost. Therefore, SOI manufacturers produce 400-mm wafers with better Si thickness uniformity and surface roughness than for 200-mm wafer to meet this demand. The trend follows for smaller diameter wafers as well. Lithography processes also have superior alignment tolerances for larger diameter wafers. Therefore, these wafers are preferred.

Waveguide by lithography and etching needs to be optimized by fabricating test structures to measure the waveguide propagation loss with high sensitivity. Lithography and etch recipes are modified and then and compared.

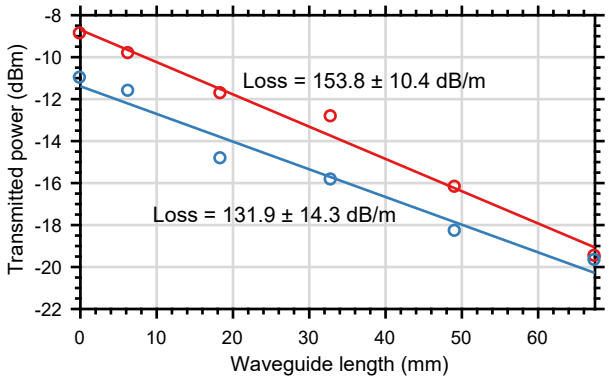

Figure 3.3: Waveguide loss extracted from transmission measurements at 780 nm wavelength for a Si_3N_4 waveguide of 500 nm width and 200 nm height. Red and blue curves correspond to transmission measurements from different chips for the same waveguide design.

3.4 Characterization

A few examples of waveguide propagation loss, taper loss, and bend loss characterizations are presented here to demonstrate the general design process for optimizing these waveguide properties. For each, a simulation is first performed to find suitable designs for the experimental characterization. Every example uses ∼780 nm wavelength and 200-nm thick Si_3N_4 waveguides.

The waveguide loss is estimated from the model discussed in Section 3.2.1. Archimedean spirals are used to form different lengths of waveguides for transmission measurements shown in Fig. 3.3. Loss is extracted from measurements on two different chips to be 153.8 ± 10.4 dB/m and 131.9 ± 14.3 dB/m. To support optical modes in the VIS to the mid-IR, this waveguide is larger than necessary for this wavelength and the longer wavelengths are expected to have less loss. These values could be reduced by increasing the waveguide aspect ratio.

The taper loss is simulated in Fig. 3.4 as a function of the taper length. Phenomenologically, the optimal taper length scales with a factor including the maximum width $w_{\max}$ and the wavelength λ as $L_{\text{taper}} = N(w_{\max}^2/\lambda)$, where N is the taper scaling factor.

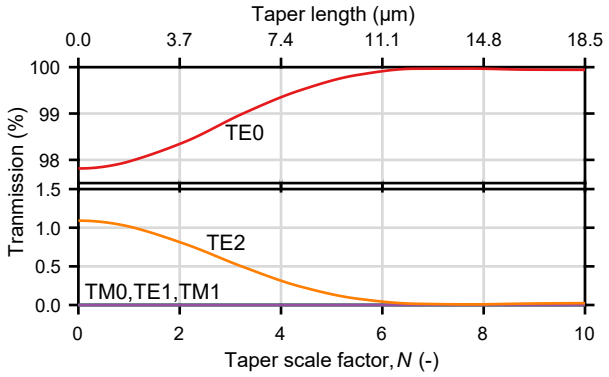

Figure 3.4: Simulated taper transmission at 780 nm wavelength for a Si_3N_4 waveguide of 500–1200 nm width and 200 nm height.

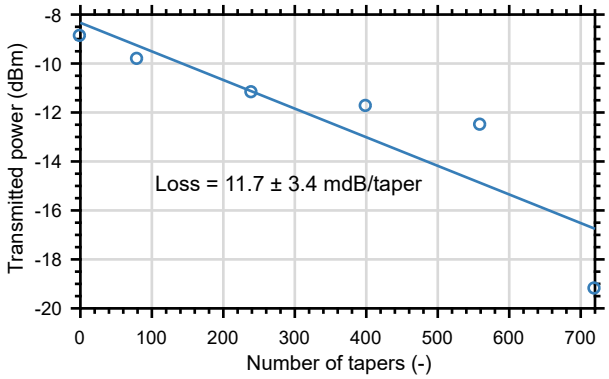

Figure 3.5: Loss per taper extracted from transmission measurements of cascaded tapers at 780 nm wavelength for a Si_3N_4 waveguide of 500–1200 nm width and 200 nm height.

The fundamental mode has close to 100 % transmission and the higher order modes have near 0 % transmission for a scaling factor of $N = 10$.

Tapers are fabricated from 0.5-µm to 1.2-µm width over a length of 27.7 µm, corresponding to $N = 15$. Transmission measurements of cascaded tapers are plotted in Fig. 3.5 and the a loss of 11.7 ± 3.4 mdB/taper is extracted from a linear fit to the data on a log-scale. The waveguide loss accounts for about 4 mdB, so the excess loss is on the order of 7.7 mdB/taper, or 0.9982 %/taper. Although this is significantly higher than the waveguide propagation loss, devices such as AWGs typically use 4–8 tapers, so this taper loss would be negligible.

Bend loss and the minimum bend radius of a particular waveguide can significantly limit the layout footprint and consequently the insertion loss of a photonic device, such as an AWG. Routing the phased array of waveguides in an AWG requires bends and making the bends on each waveguide the same can reduce the total phase error. The loss from a particular type of adiabatic bend is investigated here. This bend design is divided into a number of segments $\mathcal{S}$ for each half of the total bending angle θ_{T}. The bend radius for each segment m is calculated by:

$$R_{\mathrm{m}} = \begin{cases} R_{\min}\left[1 + 7\left(\frac{\mathcal{S}-m}{\mathcal{S}-1}\right)^7\right] & \text{for } m = 1:\mathcal{S} \text{ and } \theta < \theta_{\mathrm{T}}/2 \\ R_{\min}\left[1 + 7\left(\frac{m-1}{\mathcal{S}-1}\right)^7\right] & \text{for } m = 1:\mathcal{S} \text{ and } \theta > \theta_{\mathrm{T}}/2\,. \end{cases} \tag{3.2}$$

With this gradual transition of the bending radius, the loss and reflection associated with mode mismatch between straight and bent regions is avoided. Other works have used partial spline-bend structures to achieve the same effect and minimize the bend size [25]. For this adiabatic design in (3.2), the footprint of each bend occupies ∼1370 µm^2 for $\mathcal{S} = 25$. To determine an appropriate minimum bend radius, bend loss is simulated in Fig. 3.6. Although the loss seems negligible for radii >10 µm, a value of 20 µm is chosen for this experiment to allow for fabrication tolerances and simulation error.

Cascaded bends with a total angle of $\theta_{\mathrm{T}} = 90°$ are fabricated to estimate the loss per bend in Fig. 3.3. The extracted value is 0.00343 ± 0.00341 mdB/bend, which is very close to the uncertainty limit for this set of cascaded bends. Again, since an AWG will have two of these bends per arrayed waveguide, this loss is negligible. Further optimization can reduce the bend segments $\mathcal{S}$ and the minimum bend radius to reduce the total footprint size. Also, a similar approach to [25] could be tested to used this adiabatic bend for an angular section of the input and output with a constant bend radius in the center to reduce the total footprint.

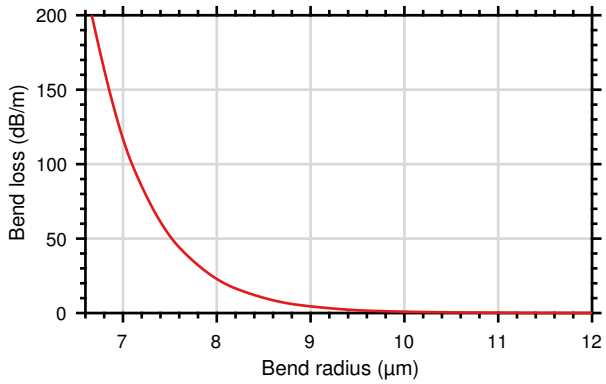

Figure 3.6: Bend loss at 780 nm wavelength for a Si_3N_4 waveguide of 1200 nm width and 200 nm height. Calculation is performed with FIMMWAVE using the finite-difference method and perfectly-matched-layer boundary condition [26].

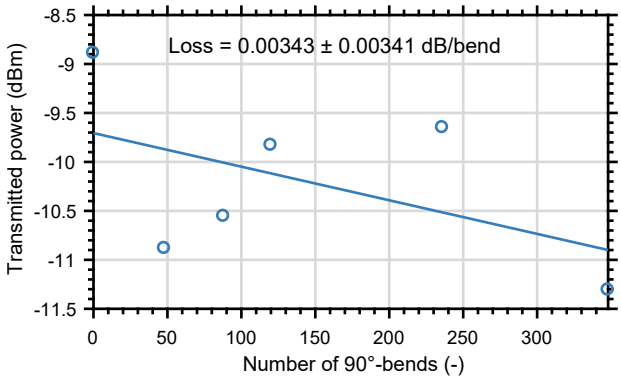

Figure 3.7: Loss per 90°-bend extracted from transmission measurements of cascaded bends at 780 nm wavelength for a Si_3N_4 waveguide of 1200 nm width and 200 nm height.

3.5 Beam quality

Far-field profiles and beam quality (M^2) values can be calculated from simulated near-field waveguide modes [27]. First the angular far-field profile is calculated from the electric field profiles of the mode at the waveguide facet for angular directions $\theta_\perp$ and $\theta_\parallel$

relative to the polarization, using the expressions:

$$P(\theta_\perp) \propto \cos^2\theta_\perp \left| \iint e^{-ikx\sin\theta_\perp} \mathcal{E}(x,y)\,\mathrm{d}x\,\mathrm{d}y \right|^2 , \tag{3.3a}$$

$$P(\theta_\parallel) \propto \cos^2\theta_\parallel \left| \iint e^{-iky\sin\theta_\parallel} \mathcal{E}(x,y)\,\mathrm{d}x\,\mathrm{d}y \right|^2 . \tag{3.3b}$$

To calculate the M^2, the near-field and far-field widths are needed. Various methods are common for calculating the mode width, including the full-width at half-maximum (FWHM) and $1/e^2$ widths. While these are relevant parameters for profiles of known shapes, such as Gaussian, Lorenztian, sech^2, and others, arbitrary profiles are not well described by the FWHM or $1/e^2$ widths. The D4σ width is the preferred method of specifying the far-field divergence. For Gaussian shapes, the D4σ width is equivalent to the $1/e^2$ width. The percent of power within the divergence angle as calculated with the D4σ method does not vary as much as the other methods when the mode shape is not Gaussian. From the far-field power profile, P, the second moment of inertia is calculated as:

$$\langle d_{\mathrm{D4}\sigma} \rangle = 4\sqrt{\frac{\int (d-\bar{d})^2 P\,\mathrm{d}d}{\int P\,\mathrm{d}d}} , \tag{3.4a}$$

$$\langle \theta_{\mathrm{D4}\sigma} \rangle = 4\sqrt{\frac{\int (\theta-\bar{\theta})^2 P\,\mathrm{d}\theta}{\int P\,\mathrm{d}\theta}} , \tag{3.4b}$$

giving the near-field spatial dimension d and the far-field angular width $\theta_{\mathrm{D4}\sigma}$. Beam quality, M^2, is calculated for each transverse dimension as:

$$M^2_{\theta_\perp} = \frac{\pi}{\lambda} \langle d_{\mathrm{D4}\sigma,\perp} \rangle \langle \theta_{\mathrm{D4}\sigma,\perp} \rangle , \tag{3.5a}$$

$$M^2_{\theta_\parallel} = \frac{\pi}{\lambda} \langle d_{\mathrm{D4}\sigma,\parallel} \rangle \langle \theta_{\mathrm{D4}\sigma,\parallel} \rangle . \tag{3.5b}$$

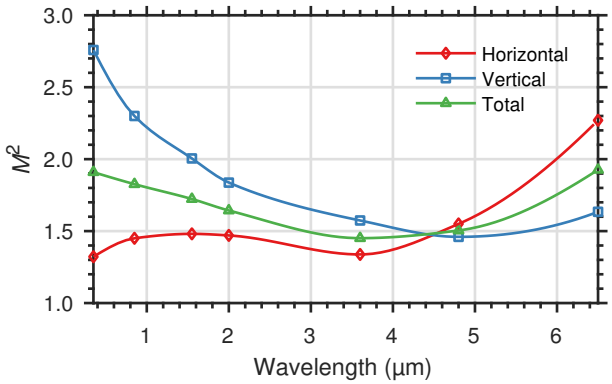

Figure 3.8: Simulated M^2 for a Si_3N_4 waveguide of 2000-nm width and 200-nm height.

The total M^2 is the geometric mean of the two angles: $M^2 = M_{\theta_\perp} M_{\theta_\parallel}$. These beam quality values are calculated for a Si_3N_4 waveguide with 200-nm thickness and 2.0-μm width in Fig. 3.8. Although these values are low (<3) relative to typical high-power diode lasers, solid-state and gas lasers can have M^2 values approaching 1.0. Also, cylindrical waveguide cores, like in optical fibers, have similarly good beam quality. By increasing the waveguide width and thickness, the M^2 can be decreased further. A different technique is used to experimentally determine the M^2 by fitting a line to the divergence angle of a focused beam, using a beam-profiling camera.

An alternative approach to beam combining is to fabricate an array of lasers with outputs in close proximity. However, a single multi-spectral output waveguide has a drastically lower M^2 value compared to this approach. To illustrate this comparison, the beam quality of SOI waveguide outputs are calculated in the near-IR, short-wave-IR, and mid-IR. Single, multi-spectral near-field power profiles near 1.5 μm, 2.0 μm, and 3.6 μm are simulated in Fig. 3.9 and the corresponding M^2 values are 2.98, 2.65, and 2.01. The Si waveguide width is 2.0 μm and the thickness is 0.5 μm. Note that the beam quality is calculated separately for each wavelength. Given that each waveguide has the same geometry, a single multi-spectral output with all of these waveguides

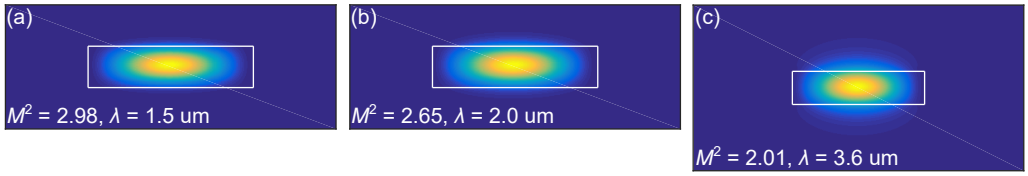

Figure 3.9: Beam quality comparison of single SOI outputs with 0.5-µm thickness and 2.0-µm width for (a) 1.5 µm, (b) 2.0 µm, and (c) 3.6 µm wavelengths.

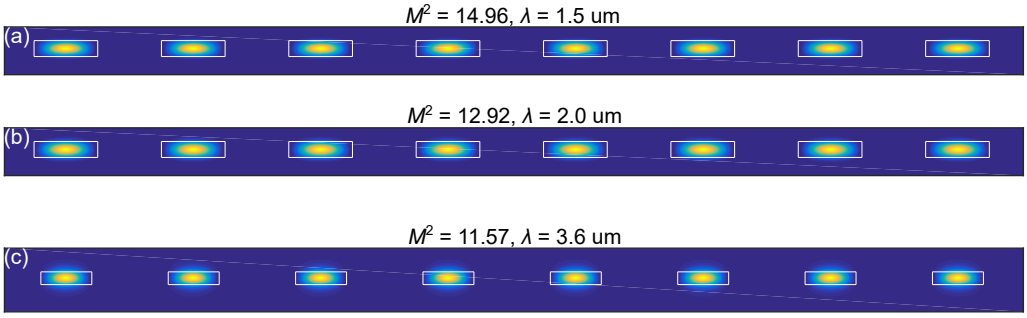

Figure 3.10: Beam quality comparison of arrays of SOI outputs with 0.5-µm thickness and 2.0-µmwidth for (a) 1.5 µm, (b) 2.0 µm, and (c) 3.6 µm wavelengths.

would have an effective $\overline{M}^2$ equal to the geometric mean of the M^2 at each wavelength: $\overline{M}^2 = (M^2_{\text{near-IR}} M^2_{\text{short-wave-IR}} M^2_{\text{mid-IR}})^{1/3} = 2.51$.

Similar calculations for the alternative approach to beam combining (output arrays) are shown in Fig. 3.10 for arrays of eight output channels. The spacing is determined such that each mode is not greatly perturbed by the adjacent waveguides. Again, the beam quality is calculated for each array at 1.5 µm, 2.0 µm, and 3.6 µm wavelengths to be 14.96, 12.92, and 11.57, respectively. An effective beam quality is found as $\overline{M}^2_{\text{array}} = (M^2_{\text{near-IR array}} M^2_{\text{short-wave-IR array}} M^2_{\text{mid-IR array}})^{1/3} = 13.08$, a $\sim$5$\times$ increase compared to the single multi-spectral output. This means that $\sim$5$\times$ less power can be coupled to a diffraction-limited beam from the arrayed output compared to the single multi-spectral output. This difference becomes greater as the number of combined wavelengths increases [28]. If the pitch between arrayed waveguides increase, then the total M^2 drastically increases.

3.6 Summary and conclusion

A set of waveguide platforms for guiding an ultra-broadband range of wavelengths on a Si substrate is presented. Fundamental design methods are highlighted that provide a foundation for AWGs, broadband combiners, and heterogeneously integrated lasers. To further improve the ultra-broadband designs, updated absorption data is desired with measurements on the actual thin-film materials used in these waveguide platforms: thin films of SiO_2 oxidized in Si, Si_3N_4 deposited by low-pressure chemical vapor deposition (LPCVD), Si from the SOI device layer, and Ge epitaxially grown on Si. Propagation, taper, and bend losses from waveguides are simulated and characterized in the VIS. These serve as examples for the similar designs and characterizations at other wavelengths in the following chapters.

Beam quality is detailed and example values of M^2 are shown for a Si_3N_4 and for a Si waveguide cores. The advantage of spectral beam combining is evident from the comparison of single multi-spectral waveguide outputs to arrays of uni-spectral waveguide outputs. In the following chapters, experiments are performed on spectral beam combining components to optimize design for high fundamental-mode transmission. These are essential foundations for integrated high-brightness lasers.

References

[1] J. F. Bauters, M. J. Heck, D. D. John, J. S. Barton, C. M. Bruinink, A. Leinse, R. G. Heideman, D. J. Blumenthal, and J. E. Bowers, "Planar waveguides with less than 0.1 dB/m propagation loss fabricated with wafer bonding," Opt. Express **19**, 24090–24101 (2011).

[2] M. A. Green and M. J. Keevers, "Optical properties of intrinsic silicon at 300 K," Prog. Photovolt. Res. Appl. **3**, 189–192 (1995).

[3] R. A. Soref, S. J. Emelett, and W. R. Buchwald, "Silicon waveguided components for the long-wave infrared region," J. Opt. A: Pure Appl. Opt. **8**, 840–848 (2006).

[4] W. Kaiser, P. H. Keck, and C. F. Lange, "Infrared absorption and oxygen content in silicon and germanium," Phys. Rev. **101**, 1264 (1956).

[5] R. Soref, "Mid-infrared photonics in silicon and germanium," Nat. Photon. **4**, 495–497 (2010).

[6] E. J. Stanton, M. J. Heck, J. Bovington, A. Spott, and J. E. Bowers, "Multi-octave spectral beam combiner on ultra-broadband photonic integrated circuit platform," Opt. Express **23**, 11272–11283 (2015).

[7] A. Spott, J. Peters, M. L. Davenport, E. J. Stanton, C. D. Merritt, W. W. Bewley, I. Vurgaftman, C. S. Kim, J. R. Meyer, J. Kirch, L. J. Mawst, D. Botez, and J. E. Bowers, "Quantum cascade laser on silicon," Optica **3**, 545–551 (2016).

[8] A. Spott, J. Peters, M. L. Davenport, E. J. Stanton, C. Zhang, C. D. Merritt, W. W. Bewley, I. Vurgaftman, C. S. Kim, J. R. Meyer, J. Kirch, L. J. Mawst, D. Botez, and J. E. Bowers, "Heterogeneously Integrated Distributed Feedback Quantum Cascade Lasers on Silicon," Photonics **3**, 35 (2016).

[9] W. Li, P. Anantha, S. Bao, K. H. Lee, X. Guo, T. Hu, L. Zhang, H. Wang, R. Soref, and C. S. Tan, "Germanium-on-silicon nitride waveguides for mid-infrared integrated photonics," Appl. Phys. Lett. **109**, 241101 (2016).

[10] J. M. Ramirez, V. Vakarin, C. Gilles, J. Frigerio, A. Ballabio, P. Chaisakul, X. Le Roux, C. Alonso-Ramos, G. Maisons, L. Vivien, M. Carras, G. Isella, and D. Marris-Morini, "Low-loss Ge-rich $Si_{0.2}Ge_{0.8}$ waveguides for mid-infrared photonics," Opt. Lett. **42**, 105–108 (2017).

[11] A. Gorin, A. Jaouad, E. Grondin, V. Aimez, and P. Charette, "Fabrication of silicon nitride waveguides for visible-light using PECVD: a study of the effect of plasma frequency on optical properties," Opt. Express **16**, 13509–13516 (2008).

[12] J. F. Bauters, M. J. Heck, D. John, D. Dai, M.-C. Tien, J. S. Barton, A. Leinse, R. G. Heideman, D. J. Blumenthal, and J. E. Bowers, "Ultra-low-loss high-aspect-ratio Si_3N_4 waveguides," Opt. Express **19**, 3163–3174 (2011).

[13] J. F. Bauters, "Ultra-Low Loss Waveguides with Application to Photonic Integrated Circuits," Ph.D. thesis, University of California Santa Barbara (2013).

[14] J. F. Bauters and D. D. John, "pyFIMM," https://github.com/demisjohn/pyFIMM (2014).

[15] T. Barwicz and H. A. Haus, "Three-dimensional analysis of scattering losses due to sidewall roughness in microphotonic waveguides," J. Lightw. Technol. **23**, 2719 (2005).

[16] D. B. Keck, R. D. Maurer, and P. C. Schultz, "On the ultimate lower limit of attenuation in glass optical waveguides," Appl. Phys. Lett. **22**, 307–309 (1973).

[17] T. Izawa, N. Shibata, and A. Takeda, "Optical attenuation in pure and doped fused silica in the IR wavelength region," Appl. Phys. Lett. **31**, 33–35 (1977).

[18] H. R. Philipp, "Optical properties of silicon nitride," J. Electrochem. Soc. **120**, 295–300 (1973).

[19] P. T. Lin, V. Singh, H.-Y. G. Lin, T. Tiwald, L. C. Kimerling, and A. M. Agarwal, "Low-Stress Silicon Nitride Platform for Mid-Infrared Broadband and Monolithically Integrated Microphotonics," Adv. Opt. Mater. **1**, 732–739 (2013).

[20] W. Sellmeier, "Zur Erkärung der abnormen Farbenfolge im Spectrum einiger. Substanzen," Ann. Phys. Chem. **219**, 272–282 (1871).

[21] B. Tatian, "Fitting refractive-index data with the Sellmeier dispersion formula," Appl. Opt. **23**, 4477–4485 (1984).

[22] C. Z. Tan, "Determination of refractive index of silica glass for infrared wavelengths by IR spectroscopy," J. Non-Cryst. Solids **223**, 158–163 (1998).

[23] K. Luke, Y. Okawachi, M. R. Lamont, A. L. Gaeta, and M. Lipson, "Broadband mid-infrared frequency comb generation in a Si_3N_4 microresonator," Opt. Lett. **40**, 4823–4826 (2015).

[24] M. Bass, E. W. Van Stryland, D. R. Williams, and W. L. Wolfe, eds., *Handbook of Optics: Devices, Measurements, and Properties*, vol. 2 (McGraw-Hill, 1994), 2nd ed.

[25] W. Bogaerts and S. K. Selvaraja, "Compact single-mode silicon hybrid rib/strip waveguide with adiabatic bends," IEEE Photon. J. **3**, 422–432 (2011).

[26] www.photond.com.

[27] A. Siegman, "Analysis of laser beam quality degradation caused by quartic phase aberrations," Appl. Opt. **32**, 5893–5901 (1993).

[28] S. Ruschin, E. Yaakobi, and E. Shekel, "Gaussian content as a laser beam quality parameter," Appl. Opt. **50**, 4376–4381 (2011).

Chapter 4

Arrayed waveguide gratings

4.1 Introduction

AWGs either combine or split closely-spaced spectral channels of light, originally developed for wavelength division multiplexing (WDM) in optical communication systems to expand network capacity [1–5]. Decades of research and development has been spent to optimize the device insertion loss, inter-channel crosstalk, and footprint, among other characteristics [1–3, 6–13]. As the field of photonics moved in new directions, enabled by integration advancements with PICs, more applications became evident for AWGs. Spectroscopic sensors [14–19] and multi-spectral high-brightness light sources [20, 21] are examples of prominent applications that rely on AWGs.

Since the total insertion loss of an AWG scales with the number of channels, devices with ultra-low loss (<2 dB loss per channel) are necessary to efficiently combine many wavelengths (*e.g.*, >5 for <10 dB cumulative loss) [22, 23]. Especially for power scaling by spectral beam combining [24] or intra-cavity AWG lasers [20, 25], this level of performance is required. These AWG lasers have not recently been pursued due to the loss-penalty from an AWG within the laser cavity. However, further development to

decrease AWG loss would enable this technology. Spectral beam combiners integrated with arrays of heterogeneously integrated lasers would enable many applications in need of either high-power, broadband, and coherent light sources [21, 26]. In particular, Si [27] and Si_3N_4 [28] AWGs with low loss and low crosstalk are desirable for CMOS-compatible PICs [10, 29, 30]. Fully-integrated transceivers have been realized with the heterogeneous integration of lasers on Si [31–33]. Aside from AWGs, WDM devices have been demonstrated with reduced footprint [34, 35]. However, they exhibit much higher loss and support fewer channels.

This chapter details a design methodology for creating ultra-low loss AWGs and reports demonstrations of AWGs in the VIS, near-IR, short-wave infrared (short-wave-IR), and mid-IR. A very low loss AWG has previously been demonstrated on SOI; however, measurement uncertainty was not discussed [36]. Uncertainty analysis in Section 4.4 and Section 4.4 find that the standard AWG normalization method is not sufficient for characterizing ultra-low loss AWGs on SOI. A new method is developed and demonstrated.

4.2 Design methodology

There are various approaches to design an AWG, since there are many inter-dependent parameters. A set of assumptions must be made to begin the design process, then iteration is required to refine the device performance. Developing an accurate transmission model that can be generated quickly is necessary to design an AWG. For the application of beam combining, achieving low loss at the peak of each channel is the most important figure-of-merit. Therefore, a unique design flow is used. Some parameters must be arbitrarily chosen while others are calculated. To generate the AWG mask layout, the following physical parameters must be determined: number of channels (N_{ch}), number of

arrayed waveguides (AWs) (N_{AW}), Rowland radius (r), length increment between AWs (ΔL), width of the AWs (w_{AW}), width of the AWs at the FPR interface ($w_{\mathrm{AW\text{-}FPR}}$), width of the i/o waveguides at the FPR interface ($w_{\mathrm{io\text{-}FPR}}$), center-to-center spacing between AWs at the FPR ($d_{\mathrm{c,AW}}$), and center-to-center spacing between i/o waveguides at the FPR ($d_{\mathrm{c,io}}$).

The center wavelength λ_{c}, channel separation Δf or $\Delta\lambda$[1], and N_{ch} are dependant on the application and can greatly affect the entire AWG design. A large number of channels will increase the AWG layout footprint area (S). Longer wavelengths and larger channel spacing both decrease the grating order. This typically reduces the loss, but at a certain extent the device size increases unreasonably, causing propagation losses to dominate[2]. The channel non-uniformity, L_{u}, defined as the ratio between the center channel peak-transmission and the outer channel peak-transmission, is a parameter that must be arbitrarily chosen. For $L_{\mathrm{u}} = 3.0$ dB, the AWG transmission spectrum is cyclic, meaning the spectral difference between grating orders, or the free spectral range (FSR), is approximately equal to $N_{\mathrm{ch}}\Delta\lambda$. To ensure low loss for all AWG channels, smaller values of L_{u} are desired, though decreasing L_{u} does increase the footprint. A value of 1.0 dB typically allows for the convergence of a low-loss AWG design.

4.2.1 Parameter design

First, the layer thickness of the lower cladding, core, and upper cladding of the waveguide need to be determined. In the case where lasers are heterogeneously integrated, these values are designed to support high confinement in the transverse hybrid mode and simultaneously provide an efficient III–V/Si taper transition. Also, because the lasers

[1]The channel separation is defined as the difference in frequency between the peaks of two adjacent channels. The approximate wavelength equivalence is also quoted, but the wavelength spacing actually varies across the channels.

[2]This effect occurs because of the radial symmetry of the input waveguide divergence, which needs to be converted to a linear symmetry in the AWs.

preferentially emit light in one polarization (TE or TM), the AWG waveguides are also only designed for one, corresponding polarization[3]. At the near-IR, the SOI platform with 0.50-µm of Si and 1.00-µm of SiO_2 is typically used.

The effective and group indices are calculated for a range of waveguide widths, starting with the lithographically limited narrow width and ending at a width that supports about four modes. An initial choice for the width of the AWs, w_{AW}, is to support only a single mode. The bend loss is then simulated, as in Section 3.2, to determine the minimum acceptable bend radius. Wider widths will typically decrease the loss and phase noise, at the expense of promoting an additional grating mode.

Waveguide widths and separations at the interface to the FPR are some of the most important parameters, and the most difficult to design. As a starting point, the i/o waveguide widths and the AW widths at this interface, $w_{\text{io-FPR}}$ and $w_{\text{AW-FPR}}$, are chosen to support only one symmetric modes, *i.e.*, two modes are supported: one symmetric and one asymmetric. Mode profiles for these two cross-sectional geometries must be calculated, since they will be used in the design and transmission simulation. The edge-to-edge separation between AWs, $d_{\text{AW-FPR}}$, is determined by the lithographic limit. For deep-UV stepper systems, this value is typically 200 nm, but this depends on the core material and thickness. Separation between the i/o waveguides $d_{\text{io-FPR}}$ affects many other design parameters, though it most directly affects the adjacent channel crosstalk. Through iteration, this parameter should be determined such that the adjacent channel crosstalk approximately equals the average crosstalk from other channels. Increasing $d_{\text{io-FPR}}$ reduces the adjacent channel crosstalk and increases the footprint. A good initial estimate is set $d_{\text{io-FPR}}$ equal to the i/o waveguide width at the FPR interface $w_{\text{io-FPR}}$.

[3]The design methodology assumes either TE or TM polarization. Therefore, when discussing the modes of a waveguide, only one polarization is taken into account. For diode lasers, the TE polarization is used, and for QCLs, the TM polarization is used.

With these considerations, the center-to-center waveguide spacing are then found by the expressions: $d_{\mathrm{c,io}} = d_{\text{io-FPR}} + w_{\text{c,io-FPR}}$ and $d_{\mathrm{c,AW}} = d_{\text{AW-FPR}} + w_{\text{c,AW-FPR}}$.

Far-field angular profiles of the i/o and AWs at the FPR interface (P_{io} and P_{AW}) are calculated from the simulated near-fields profiles for TE or TM modes:

$$P(\theta_x) \propto \cos^2\theta_x \left| \iint e^{-ikx\sin\theta_x} \mathcal{E}(x,y)\,\partial x\,\partial y \right|^2 . \tag{4.1}$$

The x-coordinate is aligned with the waveguide width and the y-coordinate is aligned with the waveguide height. From the center of the FPR, the angle of the outer channels relative to the center channel, $\theta_{\max}$, is found from the intersection between L_{u} and P_{io}. Next, the Rowland radius is calculated as:

$$r = s_{\max}/\theta_{\max}\,, \tag{4.2a}$$

where

$$s_{\max} = \frac{N_{\mathrm{ch}} - 1}{2} d_{\mathrm{c,io}}\,. \tag{4.2b}$$

This is followed by the calculation for the length increment in the AWs, expressed as:

$$\Delta L = \frac{f_{\mathrm{c}}}{\Delta f} \frac{d_{\mathrm{c,io}} d_{\mathrm{c,AW}} n_{\mathrm{FPR}}}{r n_{\mathrm{g}}}\,. \tag{4.3}$$

The number of AWs is specified by finding the angular aperture θ_{a} that encompasses most of the light from i/o waveguides. This is calculated numerically to solve the following equation:

$$t_{\mathrm{ap}} = \frac{\int_{-\theta_{\mathrm{a}}/2}^{\theta_{\mathrm{a}}/2} P_{\mathrm{io}}\,\mathrm{d}\theta}{\int_{-\pi/2}^{\pi/2} P_{\mathrm{io}}\,\mathrm{d}\theta}\,, \tag{4.4}$$

where t_{ap} is typically chosen to be 99 %, resulting in a loss $l_{\mathrm{ap}} = 1 - t_{\mathrm{g}}$ for each FPR. Finally, the number of AWs N_{a} can be calculated by rounding the following expression to the nearest integer value:

$$N_{\mathrm{a}} = 2\theta_{\mathrm{a}} \frac{r}{d_{\mathrm{c,AW}}} + 1\,, \tag{4.5}$$

All of the AWG design parameters needed to generate the layout have now been discussed. However, a few more calculations are required to model the AWG transmission.

4.2.2 Transmission model

The AWG transmission model is an important part of the design process because iteration is required to converge on the optimal design parameters for each AWG implementation. If possible, test structures are fabricated for the same waveguide geometries used in the AWG design to estimate the propagation loss coefficient, α. The length of the first AW L_1 is also needed, which is found after one round of iteration.

To estimate the transmittance from the waveguide grating to each de-multiplexed waveguide, t_{g}, the following constituent losses are considered: the side-order loss l_{side}, the aperture loss l_{ap}, and the loss from the far-field profile of the AWs l_{ff}. Side-order loss is dependent on the angular FSR, θ_{FSR}, which is defined as:

$$\theta_{\mathrm{FSR}} = \frac{\lambda}{d_{\mathrm{c,AW}} n_{\mathrm{FPR}}}\,, \tag{4.6}$$

where n_{FPR} is the effective index in the FPR region. Power transmission to the adjacent grating orders is calculated from the far-field profile P_{AW} at angles $\theta_{\mathrm{ch}} \pm \theta_{\mathrm{FSR}}$ for each channel. Similarly, the loss, l_{ff}, to each channel is calculated from P_{AW} at each angle θ_{ch}. Then, the sum is formulated as $t_{\mathrm{g}} = 1 - (l_{\mathrm{side}} + l_{\mathrm{ff}} + l_{\mathrm{ap}})$.

The electric field transfer function of the AWG, $\mathcal{A}$, is expressed as:

$$\mathcal{A} = \sqrt{t_{\mathrm{g}}} \sum_{j=1}^{N_{\mathrm{AW}}} E_j (1 + \delta_j) \exp\big(i\theta_j\big) \,, \tag{4.7a}$$

with:

$$\theta_j \equiv k_0 [n_{\mathrm{AW}} L_{\mathrm{AW},j} + n_{\mathrm{FPR}} (r + L_{\mathrm{FPR},j})] + \phi_j \,, \tag{4.7b}$$

where k_0 the free-space propagation constant and r the Rowland radius [7]. The (complex) effective refractive indices n_{AW} and n_{FPR} correspond respectively to the AWs and the FPR. Parameters E_j, δ_j and ϕ_j denote respectively the electric field amplitude at the input FPR interface, the amplitude error, and the phase error in AW j [12]. This AW has a length $L_{\mathrm{AW},j}$ and $L_{\mathrm{FPR},j}$ is the distance in the FPR from AW j to each de-multiplexed waveguide.

Scattering loss accounts for the amplitude error, δ_j, though this term is relatively uniform across each AW. In practice, imperfections from fabrication may cause large scattering points in a small subset of AWs and the effect is modeled with this parameter. Phase error, ϕ_j, arises from interfacial scattering and mask layout errors. Some mask layout imperfections can be resolved by decreasing the address unit of the mask-writing tool [11]. The scattering component of ϕ_j calculation is detailed in [37] and an example is given in Section 4.3.1.

4.2.3 Experimental setup

AWGs are characterized by measuring the transmission spectrum of each channel. Alignment of the input and output waveguides to an input light source and photo-detector is an important feature that will affects the insertion loss and crosstalk parameters.

Also, sufficient polarization control is a difficult to achieve. There are a few types of experimental setups typically used to measure passive waveguide components, such as an AWG.

Fiber coupling, or lensed-fiber coupling, is often used to reduce the complexity of the setup, while still affording a high numerical aperture for off- to on-chip coupling. The small spot-size of the lensed fiber provides a near-ideal spatial filter, which is useful for output-coupling to filter out light scattered light not coupled through the waveguide. Polarization is controlled with with fiber-based rotators. Typically, an on-chip polarization filter is designed and the transmitted power is maximized or minimized with the polarization rotator. This method is not ideal for AWGs, since the on-chip filtering is polarization dependent, so it is not trivial to determine the on-chip polarization. Furthermore, the polarization extinction ratio (PER) is usually limited to values in the range of 20–25 dB. Crosstalk measurement is also limited to this range if the AWG is polarization dependent.

Free-space coupling out-performs the lensed-fiber setup, allowing for more accurate characterization at the expense of increased complexity. Polarization filters can be placed just before the focusing lens to achieve a PER in the range of 30–45 dB. In the VIS and the near-IR, a red laser can help align the free-space setup. Also, the lensed fibers are easy to break and can potentially damage the sample under test if they come in contact. Free-space setups are much more robust and allow added space between the focusing lens and the sample. For these reasons, a free-space coupling setup is used, where practical, for input coupling and a lensed fiber is used for output coupling.

4.3 Visible arrayed waveguide grating

[4]AWGs at VIS wavelengths have historically demonstrated transmission with more than 5.0 dB insertion loss [38, 39]. In the near-VIS[5], a loss of 1.2 dB is demonstrated at 890 nm [40]. However, even lower loss is desired for many applications and more than 1 dB of loss can be prohibitive for power scaling. The main challenges involved in making high performance AWGs at VIS wavelengths stem from interfacial scattering and phase errors due to waveguide length errors. The former is similar to Rayleigh scattering with a $1/\lambda^4$ dependence and the latter scales with a $1/\lambda$ dependence of the waveguide propagation constant. Many high performance AWGs have previously been demonstrated in the near-IR [8, 12, 28], leveraging on significantly smaller interfacial scattering and phase errors compared to VIS AWGs. A low insertion loss AWG near-VIS must combine techniques to achieve state-of-the-art sidewall roughness and material absorption, low side-order grating excitation at the input and output (i/o) free propagation regions (FPRs), low loss from waveguide bends, and low phase errors in the AWs.

Ultra-low loss silicon nitride (Si_3N_4) core and silicon dioxide (SiO_2) clad waveguides have been demonstrated by minimizing interfacial scattering loss [41] or minimizing material absorption [42]. Also, phase errors due to grid snapping during the mask writing process, as shown in [11, 43], can be reduced by using the smallest possible address unit. These two techniques previously demonstrated in AWG designs are used in the present work. In addition, the AWG design technique from Section 4.2, based on simulated waveguide modes and a numerical far-field calculation, is used instead of the Gaussian-shaped mode approximation that is usually used [7]. This provides an accurate model for the transmission spectra, including insertion loss and non-uniformity,

[4]Some of the analysis and figures in this section have been reproduced from [13] © 2016 OSA.

[5]The near-VIS is often used to describe wavelengths in the near-IR band that are very close to the VIS band. Wavelengths in the range of 700–1000 nm have been reported with this label. The near-IR refers to wavelengths in the range of 1000–2000 nm.

while reducing the computation time. Also, adiabatic waveguide bend transitions are incorporated so each AW can have identical bends without introducing loss due to mode mismatch between straight and curved sections. This prevents phase errors from varying bend modes between AWs.

The challenges preventing previous demonstrations of near-VIS AWGs from achieving low insertion loss have been addressed in this work by: eliminating bend mode mismatch, using high aspect ratio waveguides, minimizing the mask address unit, and optimizing the fabrication process with photoresist re-flow to reduce interfacial roughness and high temperature baking to reduce hydrogen impurities. Using Si_3N_4 core and SiO_2 clad waveguides on Si provides a suitable platform for this low loss 760 nm AWG. It is compatible with heterogeneously integrated lasers [44] and therefore enables technologies that integrate lasers and spectral beam combiners at the near-VIS. AWG design and performance are discussed. An insertion loss smaller than 0.5 dB and a crosstalk below −23 dB are demonstrated.

4.3.1 Design

AWG design and layout parameters are listed in Table 4.1. The center wavelength is 760 nm and eight channels are spectrally separated by 0.5 nm. The waveguide core geometry is 60-nm thick and 1.0-µm wide and laterally tapers to 1.6-µm width at the FPR interfaces. The Rowland radius is 180 µm. The AWs are separated by at least 3 µm in the array and 0.4 µm at the FPR interface. There are two identical bends for each AW to minimize phase errors from varying bend modes between waveguides, as shown in Fig. 4.1. This configuration is typically avoided because two additional straight-to-bend junctions are necessary compared to the configuration with a single bend in each arm [7]. However, the bends in our design feature tapered bend radii to minimize this junction

Table 4.1: Design and layout parameters for each VIS AWG.

Number of channels	N_{ch}	8
Number of AWs	N_{AW}	52
Rowland radius	r	179.20 µm
AW length increment	ΔL	45.99 µm
AW width	w_{AW}	1.00 µm
AW width at FPR	$w_{\text{AW-FPR}}$	1.60 µm
i/o waveguide width	w_{io}	1.00 µm
i/o waveguide width at FPR	$w_{\text{io-FPR}}$	1.60 µm
AW pitch at FPR	$d_{\text{c,AW}}$	3.20 µm
i/o waveguide pitch at FPR	$d_{\text{c,io}}$	1.80 µm
Footprint area	S	1.78 mm^2
Center wavelength	λ_{c}	760 nm

loss. Each 90° bend is divided into 25 segments of varying radii to create an adiabatic transition between between straight and curved sections of the waveguide, which have a minimum radius of 150 µm. The AWG is designed for TE polarization operation, which is compatible with integrated diode lasers, so TM polarized transmission is not investigated.

Excitation of side-order grating modes in the FPRs is minimized by increasing the density of AWs at the FPR interfaces and by decreasing the far-field divergence of each grating element [36]. The waveguide density is defined as the center-to-center waveguide spacing per unit length. Two parameters affect this waveguide density. First, minimizing the waveguide separation while maintaining the waveguide width increases the density without affecting the far-field profile of the array if the waveguide mode is not significantly perturbed by the adjacent waveguides. However, the minimum waveguide separation is limited by fabrication processes. Second, decreasing the waveguide width while maintaining the waveguide separation increases the density, but also dictates the far-field profile. Fig. 4.2(a) shows the simulated far-field divergence of the TE_0 waveguide mode into the FPR. It also shows the effective refractive indices for the first three TE modes. Increasing the waveguide width decreases the far-field divergence for widths

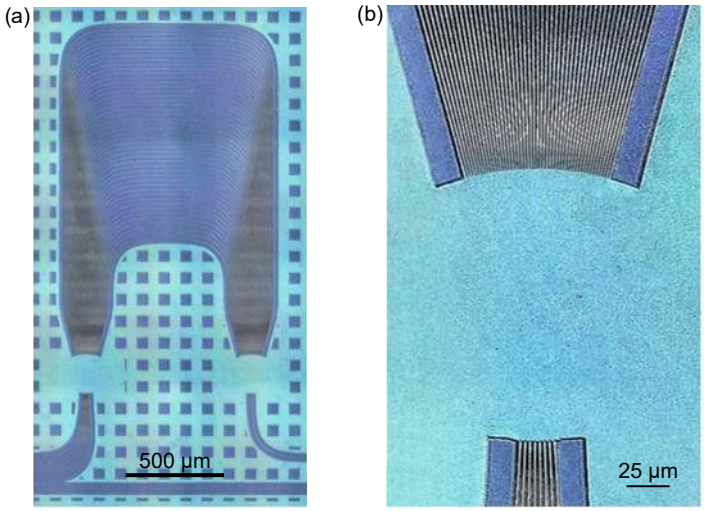

Figure 4.1: Micrographs of (a) the AWG and (b) an enlargement of the FPR.

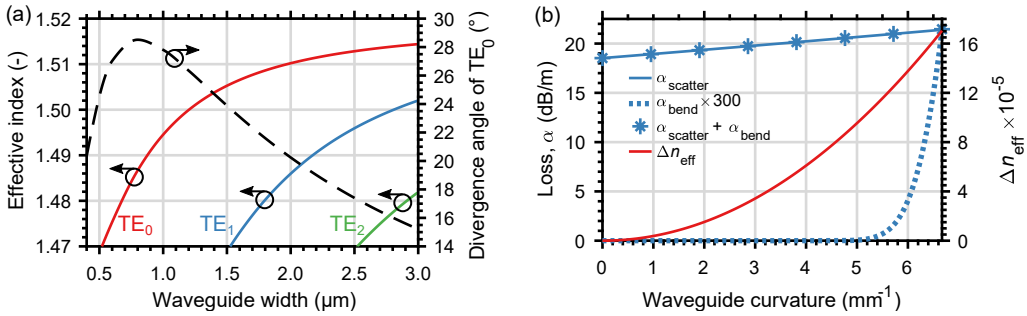

Figure 4.2: (a) Simulation of the effective indices and far-field divergence of different waveguide widths. (b) Scattering loss, bend loss, and change in effective index dependencies on the waveguide curvature.

greater than 0.8 µm, at the expense of waveguide density. It also begins to support higher order TE modes which collect some of the light, introducing loss and phase errors. Narrowing the far-field divergence may reduce the side-order excitation and, consequently, the center-channel insertion loss, but it also increases the non-uniformity. The fabricated design uses 1.6-µm wide waveguides at the FPR interface to balance these loss mechanisms. Future work is planned to develop a technique to quantify these loss contributions and optimize the waveguide width and height.

Phase errors in the AWG can be reduced by using the smallest possible address unit and minimizing the interfacial scattering, especially from the waveguide sidewall. This can also be achieved by designing the waveguides with a small value for $\partial\beta/\partial w$, where β is the waveguide propagation constant and w is the waveguide width [45]. For this design, a 5 nm address unit is used. However, a smaller address unit is desired if possible, but this was the smallest address unit available to us. From Fig. 4.2(a), $\partial\beta/\partial w$ is determined to be 0.3 rad/µm^2 for the fundamental TE_0 mode of a 1.0-µm wide and 60-nm thick AW. Scattering loss is minimized by optimizing the lithography and etching processes to reduce the waveguide sidewall roughness and by maximizing the waveguide width-to-height ratio for a desired minimum bend radius, as discussed in [41].

4.3.2 Fabrication and methods

Fabrication begins with 100 mm diameter Si wafers and growing 2 µm of thermal SiO_2. 60 nm of Si_3N_4 is deposited on both sides of the wafer by low-pressure chemical vapor deposition (LPCVD). Deep UV lithography with Shipley AR2 anti-reflectant and MicroChem UV6 photoresist defines the AWG pattern. After developing the resist, it is re-flowed at 135°C for 30 seconds to create a smooth pattern for etching the waveguides with $CF_4/CHF_3/O_2$ inductively coupled plasma (ICP). A 2 µm thick SiO_2 top cladding is deposited with plasma enhanced chemical vapor deposition (PECVD). The wafer is then diced and the facets are mechanically polished.

The waveguide sidewall and surface roughness are measured with an atomic force microscope (AFM) before the top oxide deposition, as shown in Fig. 4.3. The sidewall roughness is assumed to be non-isotropic, with a correlated roughness in the direction of the etch [45], while the surface roughness is isotropic, as expected. By measuring the sidewall position deviation and the height deviation at the center of the waveguide,

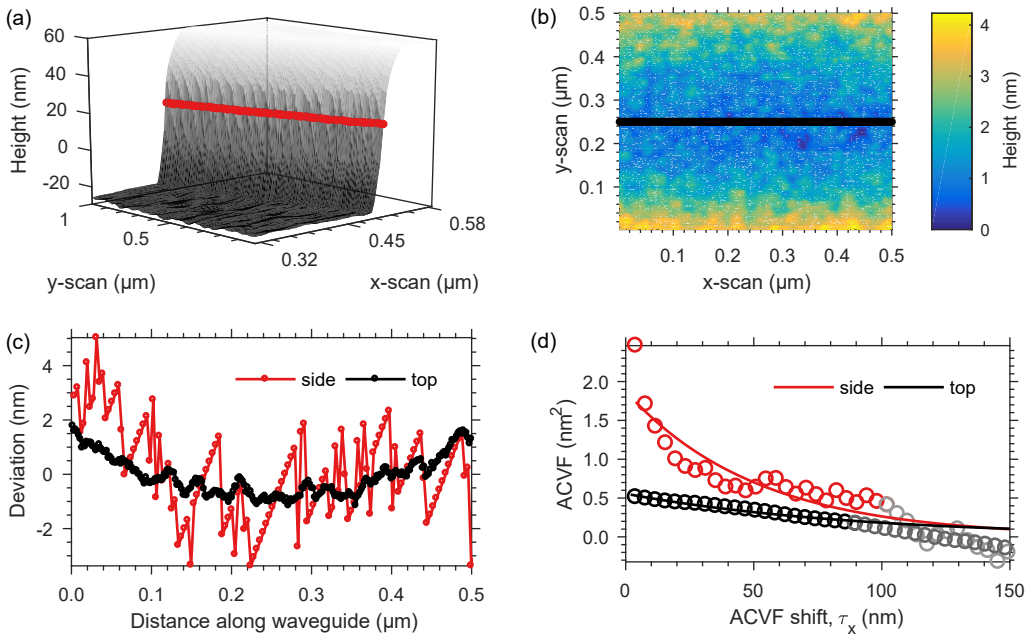

Figure 4.3: (a) AFM scan of waveguide sidewall and a red line indicating the data points used in (c). (b) AFM scan of the top surface of the waveguide and a black line indicating the data points used in (c). (c) Sidewall position deviation of the waveguide at 20 nm height (red line) and the waveguide-center height deviation (black line), both along the waveguide propagation direction. (d) Auto-covariance function (ACVF) of the AFM scans in (c) for both sidewall and top surface shown in red and black circles, respectively, with the uncorrelated data points shown in grey. The exponential fits to sidewall and top surface AVCF are shown in red and black solid lines. The grey uncorrelated data points are not used in the fit since they tend to negative values, which is not physical, while the fitting exponential function is strictly positive.

two one-dimensional (1D) scans are generated to calculate the sidewall and top surface roughness parameters. The auto-covariance function is applied to each scan and an exponential fit [37] is used to calculate the standard deviations $\sigma_{\text{side}} = 1.4$ nm and $\sigma_{\text{surface}} = 0.7$ nm and correlation lengths $L_{\text{c,side}} = 51.0$ nm and $L_{\text{c,surface}} = 89.7$ nm. AFM scans are shown in Fig. 4.3(a) and Fig. 4.3(b) of the waveguide sidewall and top surface. The corresponding 1D scan data and auto-covariance functions of these scans are shown in Fig. 4.3(c) and Fig. 4.3(d) with exponential fits.

To ensure low insertion loss, total propagation loss is estimated by calculating the bend mode radiation and interfacial scattering as a function of curvature, corresponding

to each 90° bend of the AWs. Bend modes and radiation losses are calculated with FIMMWAVE [46] and the interfacial scattering losses are calculated as in [37, 47] using the measured sidewall and surface roughness parameters. The results of these calculations are shown in Fig. 4.2(b). The minimum bend radius of 150 µm, corresponding to the maximum curvature of 6.67 mm^{-1}, has negligible radiation loss on the order of 0.05 dB/m.

It is reported in [42] that the dominating absorption loss mechanism is due to bond resonances from hydrogen impurities. In that report, the measured absorption resonances near 1540 nm are second order resonances, so the first order resonances are expected to occur near 770 nm. A method to measure the first order bond resonance absorption peaks directly is not available. Regardless, the fabrication process for this AWG is designed to reduce hydrogen impurities by baking the wafers at 1050°C for 10 hours before and after the top SiO_2 deposition. Therefore, since absorption loss is not included, the combined bend radiation and interfacial scattering loss of 21 dB/m in Fig. 4.2(b) predicts the minimum limit of the total propagation loss.

The AWG transmission spectra are measured with a tunable laser and an optical spectrum analyzer (OSA), shown in Fig. 4.4. The tunable laser free space output beam is coupled through an isolator with an isolation >25 dB. It is then coupled into an anti-reflection (AR) coated polarization maintaining (PM) fiber with an AR coated aspheric lens, both with <0.5 % reflection. The output facet of the PM fiber is connected to a 3-axis piezo-controlled input coupling stage, which holds a compact setup with an AR coated collimating lens, a linear polarizer with 45 dB extinction ratio aligned with the on-chip TE polarization, and an AR coated objective lens to focus the light to the AWG input facet. The collimating lens, the polarizer, and the objective lens, are aligned to each other and their collective position is controlled by one 3-axis stage. The AWG chip is mounted on a fixed stage and a lensed fiber is aligned to the output facet with another 3-axis piezo-controlled stage, which is then connected to the OSA. The peak

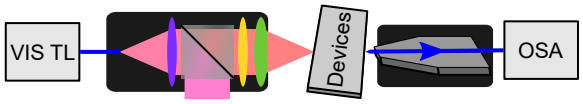

Figure 4.4: Experimental setup for the VIS AWG chip.

lasing wavelength is detected by the OSA as the laser wavelength is tuned and a 0.3 nm span centered at the lasing wavelength is integrated for each data point in the AWG transmission spectra. Using the OSA instead of a photodiode reduces side mode noise caused by the side mode suppression ratio of the laser, which is measured to be 30 ± 4 dB across the tuning range of 757–763 nm.

4.3.3 Experiment and results

Fig. 4.5 and Fig. 4.6 both show the measured and theoretical transmission spectra of the AWG, which are in good agreement. Calculations for the theoretical transmission spectra include sources of phase error, as described in [48] Eq. 5, from the measured roughness and the mask address unit. The phase error is calculated from Eq. A2 in [45] where the shortest waveguide is 1.47 mm long and the length increment is 51.16 µm. The waveguide size error is modeled by a normal distribution with standard deviation from the AFM data. The length error is modeled by a pseudo-random distribution between $\pm$ 15 nm of length in the AWs, corresponding to phase error of $\pm\ \pi/16$ radians, similar to the calculation described in [11].

The transmission spectrum of each channel is normalized to one of a straight waveguide with the same facet geometry. From the normalized transmission spectrum, the worst-case single channel crosstalk is 23 dB and the center channel insertion loss is 0.1 dB at the peak of the fifth channel, shown in yellow. The non-uniformity is 1.7 dB and the free spectral range is 6.9 nm. The fourth channel, shown in green, exhibits uniformly lower transmission, which is likely due to an undesired particle scattering light

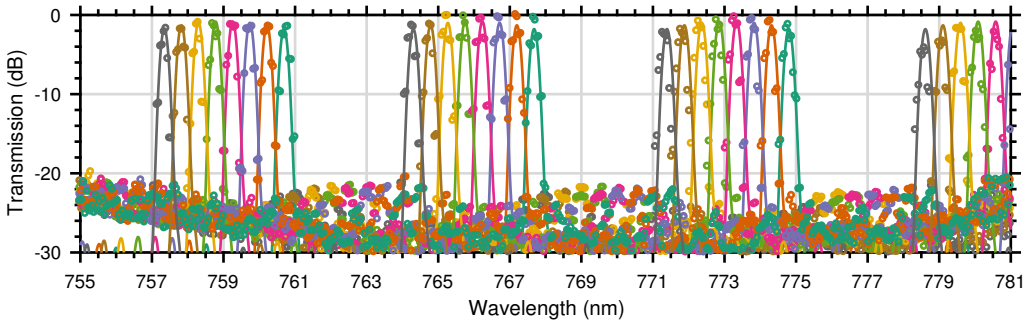

Figure 4.5: Transmission spectra of AWG channels with overlayed simulation (lower resolution), showing channel FSR.

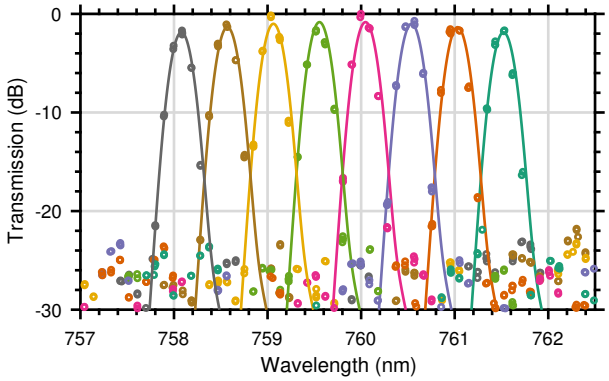

Figure 4.6: Transmission spectra of AWG channels with overlayed simulation (higher resolution).

near the demultiplexed waveguide associated with that channel. The theoretical AWG transmission spectra use an adjusted modal refractive index, which deviates from the simulated value by 3.4 %. These calculated transmission spectra predict an insertion loss of 0.83 dB and a non-uniformity of 1.04 dB. This insertion loss comes from side-order excitation of 0.59 dB, the limited aperture of AWs contributing 0.09 dB loss, predicted propagation loss of 0.10 dB, and the phase error from the sidewall roughness and length error contributing 0.05 dB loss. The most probable reason for the discrepancy between measured and theoretical insertion loss is that the actual far-field profile from the AWs is narrower than the simulated one due to perturbation from the adjacent waveguides. This would decrease the side-order excitation, resulting in lower insertion loss of the central

channel, and increase the non-uniformity of the experimental results compared to the theoretical calculations.

4.4 Near-infrared arrayed waveguide grating

[6]High-performance AWGs having loss <2 dB are prevalent with waveguide cores made of silicon dioxide (SiO_2) [8, 19] or silicon nitride (Si_3N_4) [12, 13]. In contrast, the insertion loss reported in AWGs fabricated with tantalum pentoxide [6], indium phosphide [50, 51], germanium [52–54], or Si [11, 55–57] is still prohibitively large for high-power multi-spectral lasers. In all these reports, the AWG loss was extracted by normalizing its off-chip transmittance to that of a reference waveguide with similar facet geometry and, in some cases, similar propagation length and bends. Variation in coupling efficiency coarsely limits the accuracy of this method [58], in particular for low-loss devices [59, 60].

The Si AWG demonstrated in this work with loss <2 dB is characterized by a new method using a ring resonator, proposed by the author. As schematized in Fig. 4.7(a), it contains two cascaded AWGs. This "AWG-ring" allows to drastically improve AWG characterization and rigorously define the crosstalk. The accuracy of this method is determined using data for the coupling uncertainty along with the modeled transmission spectrum of the AWG-ring. Both the waveguide method and the AWG-ring method are then compared with a statistical analysis of low-loss Si AWGs. Channel loss in the range of 1.2–1.6 dB are demonstrated, along with a crosstalk per channel near −29.1 dB. These results substantiate the accuracy of the proposed characterization method and suggest that these Si AWGs have performance comparable to state-of-the-art devices based on SiO_2 or Si_3N_4.

[6]Some of the analysis and figures in this section have been reproduced from [49] © 2017 OSA.

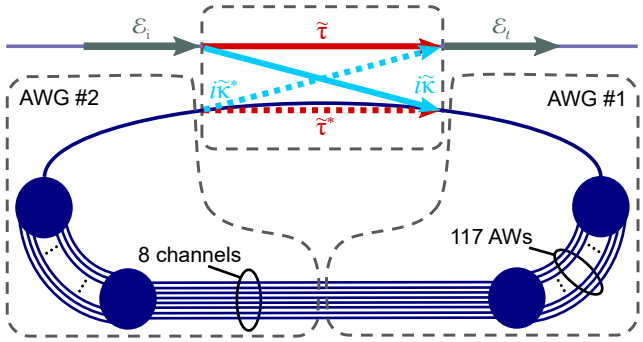

Figure 4.7: Diagram of the AWG-ring with complex amplitudes $\mathcal{E}_\mathrm{i}$ and $\mathcal{E}_\mathrm{t}$ of the input and output guided electric fields. Coupling between the bus and ring waveguides is characterized by $\tilde{\tau}$ and $\tilde{\kappa}$.

4.4.1 Transmission model

A top-view schematic of the AWG FPR is shown in Fig. 4.7(b). The AWG model developed in [12, 13] and expressed in (4.7) is extended here to account for the length L_io of the input and output waveguides and both FPRs. The electric field transfer function of an AWG is then expressed as

$$\mathcal{A}_\mathrm{extended} = \mathcal{A}\exp\left(ik_0 n_\mathrm{io} L_\mathrm{io}\right), \tag{4.8}$$

where n_io corresponds to the (complex) effective refractive index of the i/o waveguides.

Concerning the AWG-ring, coupling from the bus to the resonator can be described by the complex coefficients $\tilde{\kappa} = \kappa\exp(i\phi_{\tilde{\kappa}})$ and $\tilde{\tau} = \tau\exp(i\phi_{\tilde{\tau}})$ defined in Fig. 4.7(a). Assuming this coupling to be lossless, the following must hold [61]: $\tau^2 + \kappa^2 = 1$. Also, assuming both AWGs have the same transfer function $\mathcal{A} = \sqrt{t_\mathrm{a}}\exp(i\phi_\mathcal{A})$, the *on*-chip AWG-ring transmittance $t_\mathrm{r} = |\mathcal{E}_\mathrm{t}/\mathcal{E}_\mathrm{i}|^2$ can be expressed as:

$$t_\mathrm{r} = \left|\frac{\tilde{\tau} - \mathcal{A}^2}{1 - \tilde{\tau}^*\mathcal{A}^2}\right|^2 = \frac{\tau^2 + t_\mathrm{a}^2 - 2\tau t_\mathrm{a}\cos(\Phi)}{1 + (\tau t_\mathrm{a})^2 - 2\tau t_\mathrm{a}\cos(\Phi)}, \tag{4.9}$$

where $\Phi \equiv 2\phi_\mathcal{A} - \phi_{\tilde{\tau}}$ and t_a is the on-chip transmittance of an AWG.

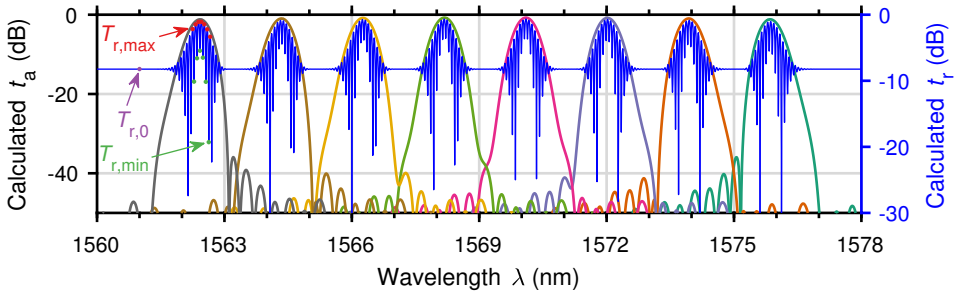

Figure 4.8: On-chip transmission spectra calculated (left axis) for each channel of an AWG and (right axis) for an AWG-ring. Colored dots show examples of the three parameters defined in (4.11), for the ideal case where $\eta = 1$.

An AWG and an AWG-ring with Si-core and SiO_2-cladding waveguides are modeled with (4.8) and (4.9), respectively. The AWG design follows the methodology detailed in [13] and the physical parameters are listed in Table 4.2. Notice that the relatively large footprint area S results from the low-loss design. This can be reduced, *e.g.*, by designing the AWs with a higher modal group index at the expense of increased loss [62]. The calculated AWG transmittance t_a is plotted in the left axis of Fig. 4.8, whereas the right axis shows the transmittance t_r of the AWG-ring for $\tau^2 = 0.15$.

The *off*-chip transmittances T_a and T_r of the AWG and of the AWG-ring, respectively, include the input and output coupling efficiency, which is defined as:

$$\eta \equiv T_r/t_r = T_a/t_a\,. \tag{4.10}$$

This quantity depends on polishing quality (for facet coupling), lithography, etch uniformity, layer thicknesses of the waveguide, and optical alignment. As illustrated in Fig. 4.8 and using (4.9), the following three parameters can be readily extracted from

the AWG-ring off-chip transmission spectrum:

$$T_{\mathrm{r}} = \begin{cases} \eta\tau^2 \equiv T_{\mathrm{r,0}} & \text{as } t_{\mathrm{a}}/\tau \to 0 \\ \eta\left(\dfrac{\tau + t_{\mathrm{a}}}{1 + \tau t_{\mathrm{a}}}\right)^2 \equiv T_{\mathrm{r,max}} & \text{for } \Phi = \pi(1+2m) \\ \eta\left(\dfrac{\tau - t_{\mathrm{a}}}{1 - \tau t_{\mathrm{a}}}\right)^2 \equiv T_{\mathrm{r,min}} & \text{for } \Phi = 2\pi m\,, \end{cases} \tag{4.11}$$

where $m \in \mathbb{Z}$. By interpolating to the same wavelength the values of T_{r} found for each case in (4.11), three expressions can be computed for t_{a}:

$$\sqrt{\frac{T_{\mathrm{r,max}}}{T_{\mathrm{r,0}}}} = \frac{\tau + t_{\mathrm{a}}}{\tau(1+\tau t_{\mathrm{a}})} \equiv R_{\mathrm{a}} \Leftrightarrow t_{\mathrm{a}} = \frac{\tau\,(R_{\mathrm{a}} - 1)}{1 - \tau^2 R_{\mathrm{a}}} \tag{4.12a}$$

$$\pm\sqrt{\frac{T_{\mathrm{r,min}}}{T_{\mathrm{r,0}}}} = \frac{\tau - t_{\mathrm{a}}}{\tau(1-\tau t_{\mathrm{a}})} \equiv R_{\mathrm{b}} \Leftrightarrow t_{\mathrm{a}} = \frac{\tau\,(1 - R_{\mathrm{b}})}{1 - \tau^2 R_{\mathrm{b}}} \tag{4.12b}$$

$$\pm\sqrt{\frac{T_{\mathrm{r,max}}}{T_{\mathrm{r,min}}}} = \frac{\tau + t_{\mathrm{a}}}{\tau - t_{\mathrm{a}}}\frac{1 - \tau t_{\mathrm{a}}}{1 + \tau t_{\mathrm{a}}} \equiv R_{\mathrm{c}} \Leftrightarrow \tau(R_{\mathrm{c}} - 1)t_{\mathrm{a}}^2 + \left[(1 + R_{\mathrm{c}})(1 - \tau^2)\right] t_{\mathrm{a}} + \tau(1 - R_{\mathrm{c}}) = 0\,. \tag{4.12c}$$

The parameters $T_{\mathrm{r,0}}$, $T_{\mathrm{r,max}}$, and $T_{\mathrm{r,min}}$, defined in (4.11), are proportional to η. In contrast, the AWG on-chip transmittance t_{a} is independent of η, as calculated from (4.12). However, other sources of uncertainty are introduced to these extracted values due the interpolation. A rigorous analysis is discussed in Sect. 4.4.4. Notice from (4.12b) and (4.12c) that both R_{b} and R_{c} are negative when $t_{\mathrm{a}} > \tau$ and positive otherwise. The correct sign is found by first evaluating R_{a} from (4.12a), since it is always positive, and then determining for which wavelengths $t_{\mathrm{a}} > \tau$. The coefficient τ should also be extracted independent of η. This is achieved in Sect. 4.4.4 by analyzing the transmittance of an unbalanced Mach-Zehnder interferometer (UMZI) with identical couplers to that of the AWG-ring [63].

Table 4.2: Design and layout parameters for each near-IR AWG.

Number of channels	N_{ch}	8
Number of AWs	N_{AW}	117
Rowland radius	r	204.42 µm
AW length increment	ΔL	15.55 µm
i/o waveguide length	L_{io}	1.60 mm
AW width	w_{AW}	1.20 µm
AW width at FPR	$w_{\mathrm{AW\text{-}FPR}}$	1.00 µm
i/o waveguide width	w_{io}	0.80 µm
i/o waveguide width at FPR	$w_{\mathrm{io\text{-}FPR}}$	1.20 µm
AW pitch at FPR	$d_{\mathrm{c,AW}}$	1.25 µm
i/o waveguide pitch at FPR	$d_{\mathrm{c,io}}$	3.60 µm
Footprint area	S	2.10 mm^2
Center wavelength	λ_{c}	1570 nm

4.4.2 Design

Three identical AWGs, AWG-rings, and UMZIs are fabricated on the same chip, along with two spiral waveguides. Fifteen straight waveguides are placed throughout the chip to study the variation in η. A cross-section scanning electron micrograph (SEM) of the bus waveguide is shown in Fig. 4.9(a). Although other reported Si AWGs use a thinner waveguide core [11], a 0.50-µm thickness is used here for compatibility with the III/V-Si heterogeneous integration platform. This supports reduced propagation loss, coupling loss to optical fiber, and phase errors in the AWG [10]. Micrographs of an AWG and of an AWG-ring are shown in Fig. 4.9(b) and Fig. 4.9(c), respectively. The input and output facet design is schematized in Fig. 4.9(d). Notice that the Si waveguide at the facet is 6.00-µm wide and tilted by 7° with respect to the normal to reduce internal reflections. The waveguide width is linearly tapered from 6.00 µm to 0.95 µm over a 200-µm length to filter out the higher-order modes arising from the angled-facet reflection of the fundamental mode. It is then bent by 7° with a 200-µm radius to align normal to the facet. The device in the center of Fig. 4.9(d) represents a straight waveguide, an AWG, a UMZI, or an AWG-ring.

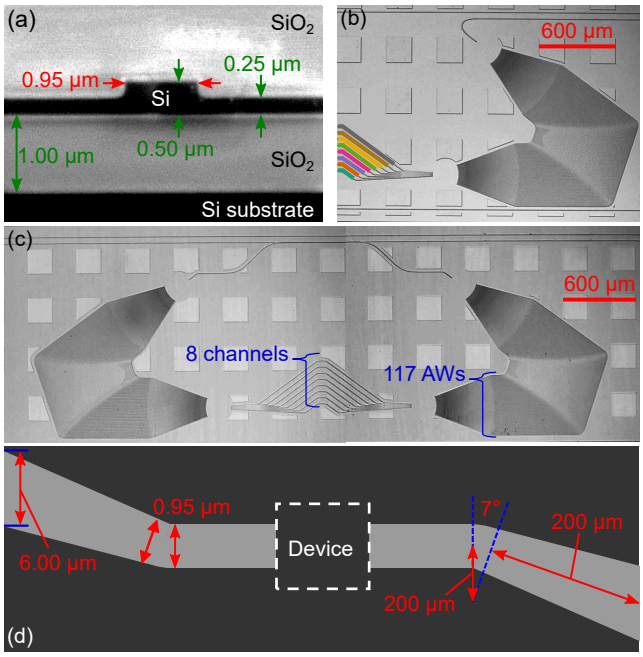

Figure 4.9: (a) Cross-section SEM of the bus waveguide. Micrographs (b) of an AWG and (c) of an AWG-ring. (d) Top-view schematic of the facet design.

4.4.3 Fabrication and methods

As seen in Fig. 4.9(a), fabrication starts with a Si-on-insulator (SOI) wafer (100-mm in diameter) containing a 0.50-µm thick Si layer on top of a 1.00-µm thick buried SiO_2 layer. Features are defined with deep-ultraviolet lithography and $SF_6/C_4F_8/Ar$ reactive ion etching to remove 0.25 µm of Si. A 4:1 mixture of sulfuric acid and hydrogen peroxide held at 80 °C strips the photoresist. A 1.00-µm thick SiO_2 layer is then sputtered to form the top cladding before dicing the wafer and polishing the facets.

Transmission spectra are measured by coupling light from a tunable laser (TL, Keysight 81680A) through each device, as depicted in Fig. 4.10. The TL is attached to a polarization-maintaining (PM) fiber (Thorlabs P5-1550PMAR) via an FC/APC connector. The other end of the PM fiber is FC/PC anti-reflective coated and connected to a collimating lens (CL, Thorlabs PAF-X-2-C). Light is then incident on a polarization beam splitter (PBS, Thorlabs CM1-PBS254) oriented to transmit on-chip transverse-

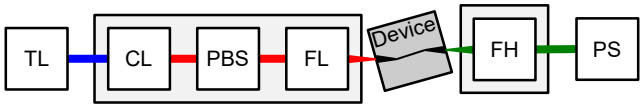

Figure 4.10: Schematic of the experimental setup to measure transmission spectra. The optical beam drawn in blue is in a PM fiber, the red one in free-space, and the green one in a single-mode fiber. Light-grey boxes represent 3-axis flexure stages.

electric polarization, which the focusing lens (FL, Thorlabs C230TM-C) directs onto the device waveguide facet. Output light is then collected with a single-mode lensed fiber (OZ Optics) attached to a v-groove fiber holder (FH, Thorlabs HFV002), and connected (FC/APC) to a power sensor (PS, Keysight 81634B). Input and output device coupling alignment is realized with 3-axis piezo-controlled flexure stages (Thorlabs MAX312). Waveguide loss characterization is accomplished by replacing the TL with an optical frequency domain reflectometry (OFDR) unit (LUNA OBR 4400) for these measurements [64].

4.4.4 Experiment and results

The blue and the black curves in Fig. 4.11(a) respectively show one off-chip transmission spectrum T_{w} and the value $\overline{T}_{\mathrm{w}}$ averaged over all straight waveguide measurements ($N_{\mathrm{w}} = 43$). These values are obtained by normalizing the straight waveguide spectra to the transmission of the TL connected directly to the PS with the PM fiber. The standard deviation σ is then extracted, along with the coefficient of variation [65]: $V_{\mathrm{w}} \equiv \sigma/\overline{T}_{\mathrm{w}}$. This parameter, plotted in Fig. 4.11(b), does not explicitly depend on the transmittance. It represents variations between samples by normalizing the standard deviation (σ) to the mean value ($\overline{T}_{\mathrm{w}}$). Therefore, it is suitable for describing the relative uncertainty on the coupling efficiency (η).

Fluctuations in T_{w} between measurements either arise from variation in η or from on-chip scattering. To investigate this, the OFDR signal of a spiral waveguide covering

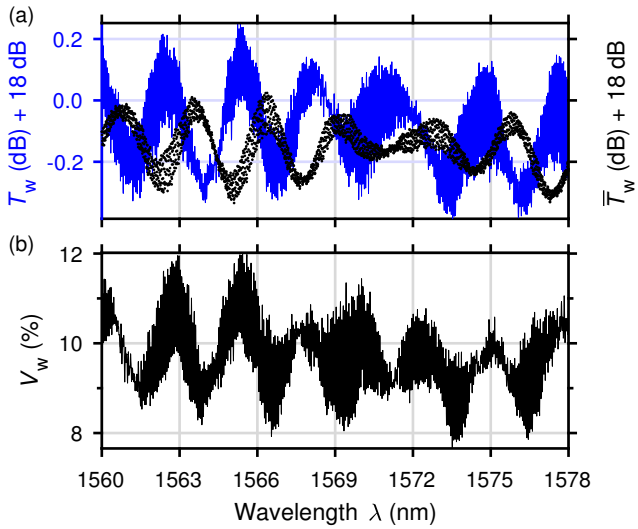

Figure 4.11: (a, left axis) One off-chip transmission spectrum T_w measured for a straight waveguide and (a, right axis) transmission spectrum $\overline{T}_w$ averaged over all straight waveguide measurements. (b) Spectrum of the coefficient of variation V_w.

5 mm^2 is acquired and plotted in Fig. 4.12. These data suggest that on-chip scattering is completely uniform. Consequently, the values of V_w obtained in Fig. 4.11(b) are only due to variation in η between measurements. A dual fit with logarithmic and constant dependencies is used to extract a loss coefficient $\alpha = 70.9(2.0)$ dB/m, where the number in parentheses is the standard uncertainty referred to the corresponding last digits of the quoted result. Although this value is comparable to similar Si waveguides [63], a fabrication process with reduced impurities and sidewall roughness is accessible and likely to improve it [66].

On-chip transmission spectra t_a are extracted for each channel of an AWG using the waveguide normalization method [11]. Results are presented in Fig. 4.13(a). A more accurate extraction by the AWG-ring method of the same data is plotted in Fig. 4.13(b).

The dynamic range of each AWG channel is usually characterized in terms of the loosely defined crosstalk (XT) [3]. A more rigorous and relevant figure-of-merit is the

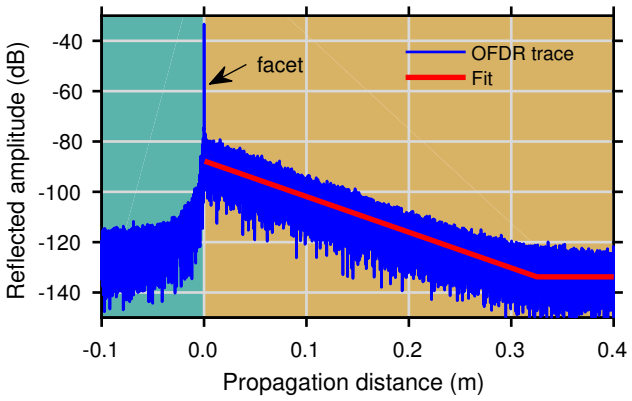

Figure 4.12: OFDR signal (in blue) of a spiral waveguide with a dual fit (in red).

3-dB *cumulative crosstalk* (CXT). For channel x, it is defined as:

$$\mathrm{CXT}_x \equiv \frac{\int_{3\mathrm{dB},x} t_{\mathrm{a},x}\,\mathrm{d}\lambda}{\int_{3\mathrm{dB},x}\left(\sum_{y=1}^{N_\mathrm{ch}} t_{\mathrm{a},y} - t_{\mathrm{a},x}\right)\mathrm{d}\lambda}\,, \tag{4.13}$$

where the integrals span the 3-dB spectral bandwidth around the peak of each channel denoted by x or y. This parameter is indicated with disks in Fig. 4.13 for each AWG channel $x = 1, 2, \ldots, N_\mathrm{ch}$. Another convenient quantity is the mean 3-dB CXT per channel, defined as:

$$\overline{\mathrm{XT}} \equiv \frac{1}{N_\mathrm{ch} - 1}\sum_{x=1}^{N_\mathrm{ch}} \mathrm{CXT}_x\,. \tag{4.14}$$

The crosstalk scales with the number of channels, so $\overline{\mathrm{XT}}$ is suitable for comparing different AWG designs.

With the waveguide normalization method [11], on-chip transmission of an AWG is extracted as:

$$t_\mathrm{a} = T_\mathrm{a}/T_\mathrm{w}\,, \tag{4.15}$$

where T_a is its off-chip transmission and T_w is the off-chip transmission of a nearby straight waveguide (see Fig. 4.11). The coefficient of variation V_w has a spectral average

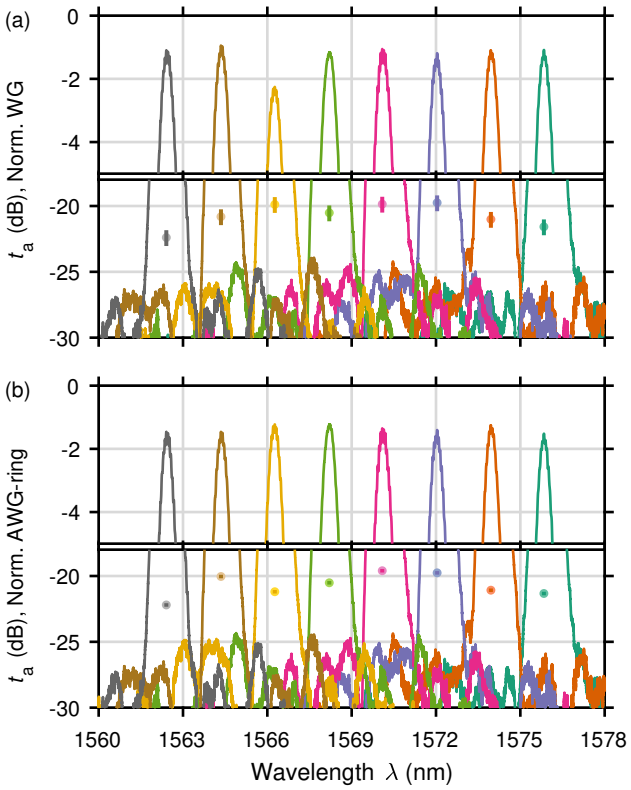

Figure 4.13: On-chip transmission spectra t_a extracted for each channel of a single AWG. Normalization is performed (a) with the waveguide method and (b) with the AWG-ring method. Disks indicate the 3-dB CXT for each channel with their respective uncertainty.

given by:

$$\langle V_w \rangle = \frac{1}{\lambda_f - \lambda_0} \int_{\lambda_0}^{\lambda_f} V_w \, d\lambda \,, \tag{4.16}$$

with $\lambda_0 = 1560$ nm and $\lambda_f = 1578$ nm. The uncertainty on t_a is then [65]: $\Delta t_a|_{(4.15)} = \sqrt{2}\langle V_w \rangle$. Values for Δt_a, $\overline{\text{XT}}$, the minimum peak channel loss (L_{min}), and the maximum peak channel loss (L_{max}) are listed in Table 4.3. While these values reveal good performance of this Si AWG, the relative uncertainties are large.

With the AWG-ring method, t_a is extracted from (4.12). Its uncertainty can be evaluated once those on $T_{r,0}$, $T_{r,max}$, $T_{r,min}$, and τ are found. The transmission $T_{w,l}$ of a straight waveguide denoted l has a coefficient of variation $V_{w,l}$, calculated within a

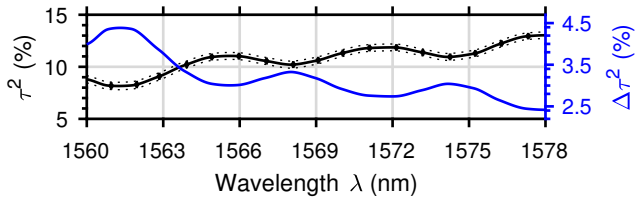

Figure 4.14: Coupling parameter τ^2 (left axis) extracted from the UMZI transmission spectra. The uncertainty $\Delta\tau^2$ is plotted on the left axis in dotted black lines and on the right axis in blue.

spectral range $\delta\lambda$. The uncertainty on each T_r is given by:

$$\Delta T_\mathrm{r} = \frac{1}{N_\mathrm{w} N_\mathrm{s}} \sum_{l=1}^{N_\mathrm{w}} \sum_{m=1}^{N_\mathrm{s}} V_{\mathrm{w},l}\left(\lambda_{m-1}; \lambda_m\right) , \tag{4.17}$$

where $N_\mathrm{s} \equiv (\lambda_\mathrm{f} - \lambda_0)/\delta\lambda$ and $\lambda_m = \lambda_0 + m\delta\lambda$. For (4.12a) and (4.12b), $\delta\lambda$ is 3/2 the AWG channel spacing, and for (4.12c), it is 3/2 the AWG-ring free spectral range (FSR). These values correspond to the spectral range that is necessary to interpolate each expression in (4.12). When evaluating (4.17) for each T_r appearing in (4.12a) and (4.12b), the spectral range is $\delta\lambda = 3.0$ nm and $\Delta T_\mathrm{r} \approx 2.95$ %. For (4.12c), $\delta\lambda = 0.1$ nm and $\Delta T_\mathrm{r} \approx 2.93$ %.

The coupling parameter τ^2 is extracted from the UMZI transmission spectra [63] and plotted in Fig. 4.14 along with its uncertainty $\Delta\tau^2$. This includes uncertainty due to η and additional variation arising from fabrication. The parameter $\Delta\tau^2$ has a spectral average $\langle\Delta\tau^2\rangle \approx 2.92$ %.

Near critical coupling, where $\tau = t_\mathrm{a}^2$ [61], additional uncertainty is introduced when interpolating the $T_\mathrm{r,min}$ values, which should vanish. Due to the finite FSR of the AWG-ring, interpolated values for $T_\mathrm{r,min}$ are not accurate as t_a^2 approaches τ. The value of τ should thus be smaller than t_a for a ∼2-dB bandwidth within the peak transmission of each channel to provide sufficient extracted data of t_a. However, decreasing τ increases $T_\mathrm{r,min}$ near the peak channel transmittance and subsequently increases the absolute uncertainty on t_a. From these considerations, the following is

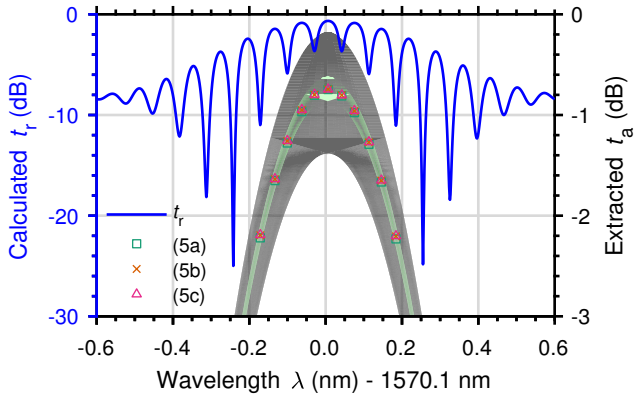

Figure 4.15: Calculated AWG-ring on-chip transmission spectrum (left axis) and (right axis) extracted AWG on-chip transmittance. The grey and the light-green areas respectively delimit the uncertainties from the conventional and the present methods.

Table 4.3: Summary of on-chip AWG transmission t_a.

Method	Δt_a (%)	$\overline{\text{XT}}$ (dB)	$L_{\min}$ (dB)	$L_{\max}$ (dB)
(4.12a)	6.65	−29.05(28)	0.98(29)	1.72(29)
(4.12b)	2.74	−29.08(12)	1.18(12)	1.60(12)
(4.12c)	3.07	−29.09(13)	1.22(13)	1.52(13)
(4.15)	13.74	−29.09(56)	0.95(60)	2.26(60)

chosen: $\tau = \sqrt{0.15} \approx -4.12$ dB. This allows to resolve a ∼2-dB bandwidth for channels with −2-dB peak transmittance.

The AWG on-chip transmittance t_a is extracted in Fig. 4.15, using the model expressed in (4.9). Substituting the values of $\Delta\tau^2$, $\Delta T_{r,0}$, $\Delta T_{r,max}$, and $\Delta T_{r,min}$ in the uncertainty propagation equation [65] obtained from (4.12) allows to extract Δt_a for each case of the AWG-ring method. These values are listed in Table 4.3.

On-chip AWG transmittance is extracted by applying (4.12) to the measured AWG-ring off-chip transmission spectrum. This is illustrated in Fig. 4.16, where the transmittance near the peak of channel #5 is plotted. The AWG transmittance extracted using (4.12a), (4.12b), and (4.12c) have overlapping uncertainty ranges, as expected, and (4.12b) is the most accurate. Outside a 1-dB bandwidth from the resonance,

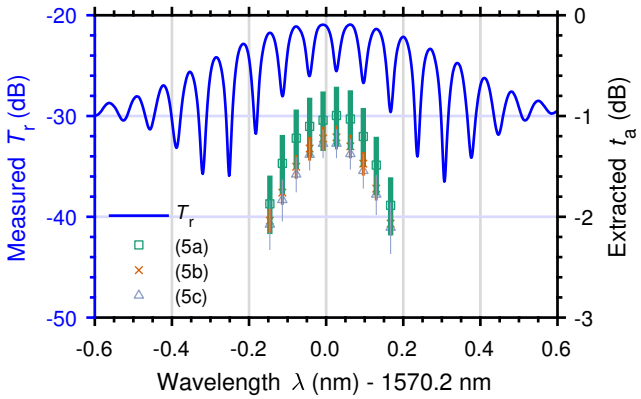

Figure 4.16: (Left axis) Measured AWG-ring off-chip transmission spectrum T_r and (right axis) AWG on-chip transmission spectrum t_a extracted using the 3 expressions introduced in (4.12).

the uncertainties increase drastically as critical coupling occurs and t_a^2 approaches τ. However, these data are not needed for normalization.

The entire transmission spectrum of an AWG-ring is now used to extract t_a for each AWG channel. From AWG-ring data shown in Fig. 4.17, the transmission within ∼1 dB of the peak for each channel of t_a are extracted. Normalization is performed in Fig. 4.13(b) on transmission data of a single AWG with the peak channel transmission obtained from (4.12b), shown in Fig. 4.17. Results are listed in Table 4.3. The peak channel wavelength is measured in three AWGs, revealing a standard deviation of ∼138 pm. Therefore, the loss may be overestimated with the AWG-ring method due to misalignment of the channels, *i.e.* the values in Table 4.3 may be at most 0.16 dB higher than the actual loss. In addition, the value for $\overline{\text{XT}}$ is, to our knowledge, the lowest reported for a Si AWG [11]. This crosstalk level is likely limited by the thickness variation of the Si core [10, 67]. Contributions to L_{min} are due to reflections at the FPR-AW transition (∼0.55 dB), the grating side-order excitations (∼0.47 dB), the limited grating aperture (∼0.09 dB), and scattering loss (∼0.08 dB).

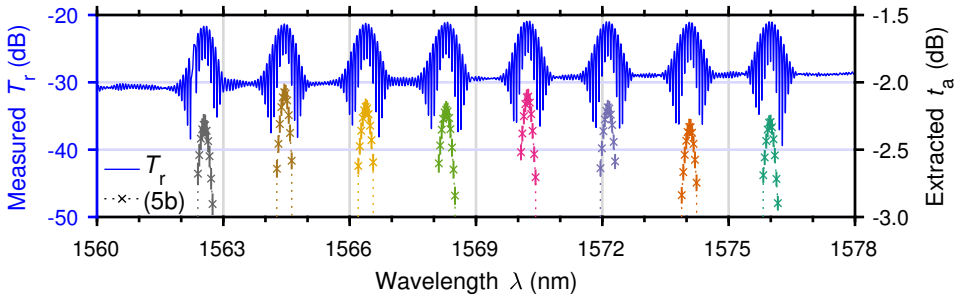

Figure 4.17: (Left axis) Measured AWG-ring off-chip transmission spectrum T_r and (right axis) on-chip transmission spectra t_a extracted for each AWG channel using (4.12b).

4.5 Short-wave infrared arrayed waveguide grating

[7]Low-loss AWGs are demonstrated at 2.0-µm wavelength. These devices promote rapidly developing photonic applications, supported by the recent development of mid-IR lasers integrated on silicon (Si). Multi-spectral photonic integrated circuits at 2.0-µm are envisioned since the AWGs are fabricated with the 500-nm thick Si-on-insulator platform, compatible with recently demonstrated lasers and semiconductor optical amplifiers on Si. Characterization with the AWG-ring method improves the on-chip transmission uncertainty to ∼6 % compared to the conventional method with an uncertainty of ∼53 %. Channel losses of ∼2.4 dB are found, with −31 dB crosstalk per channel. Fully integrated multi-spectral sources at 2.0 µm, with pump lasers, low-loss multiplexers, modulators, and an output amplifier are now feasible.

Integrated multi-spectral lasers are an important topic of interest for wavelengths spanning the near- to mid-IR [25, 69]. Such devices have application near 2-µm wavelength for communication systems with hollow-core photonic-bandgap fibers (HC-PBFs) [70, 71], gas detection and quantification [72], remote sensing [73, 74], and infrared countermeasures (IRCM). Water absorption near 2-µm also makes this

[7]Some of the analysis and figures in this section have been reproduced from [68] © 2018 OSA.

wavelength important for medical applications [75], such as for non-invasive blood glucose measurements [76] and laser surgery [77].

In this scope, an ideal optical source consists of a compact single chip with no free-space optics that emits high optical power into a near-diffraction-limited beam, and covers many spectral bands of interest. Because they are compact, efficient, reliable, and relatively inexpensive, semiconductor lasers are used in nearly every application for which they can meet the system requirements. Yet, until recently they were too immature for transitioning to advanced applications such as IRCM, except in limited spectral ranges restricted to the short-wave-IR [78] and the near-VIS [79]. This has rapidly changed over the past decade, however, with the advent of aluminum gallium nitride (AlGaN) lasers emitting in the ultra-violet [80], interband cascade lasers (ICLs) in the mid-IR [81, 82], and quantum cascade lasers in the mid-IR and long-wave infrared (long-wave-IR) [83]. Nonetheless, even an all-semiconductor source may become complex and cumbersome if free space optics are required to combine multiple beams from several spectral bands. However, on-chip multiplexers with low loss can combine an array of integrated lasers spanning many spectral bands into a single output waveguide to circumvent free-space optics [21].

AWGs have proven to have the lowest loss and crosstalk for dense channel spacing (<400 GHz) integrated optical multiplexers. An optical communication system near 2.0-µm wavelength has been demonstrated with AWGs based on indium phosphide (InP) waveguides, utilizing the minimum loss window of hollow-core photonic bandgap fibers [71, 84]. Communication systems on the Si-on-insulator (SOI) platform could reduce cost and improve performance [33]. Si is an ideal material for high-power 2-µm photonic integrated circuits (PICs) thanks to the low two-photon absorption and high Kerr coefficient [85, 86]. Low-loss Si AWGs have been reported in the near- and mid-IR at different wavelengths (1.6 µm [49], 2.3 µm [87], 3.3 µm [88], and 3.8 µm [56]).

To meet requirements for more advanced applications, lower loss AWGs are necessary. Improved characterization is also a requisite for evaluating on-chip loss lower than the typical chip-coupling uncertainties (∼2 dB).

4.5.1 Design

The layout is generated with a unique design process that emphasizes low peak channel loss over other design parameters, such as the center wavelength of each channel or footprint size (∼3.7 mm^2 for this design) [13]. This is in contrast to AWGs typically designed for communication systems, since this design begins with a different set of assumed parameters. In particular, the number of channels, the channel non-uniformity, the center wavelength, and the approximate channel wavelength spacing are decided for the application. All other parameters are derived from these first assumptions, then the device layout is drawn. Multiple design iterations are performed based on the physical layout dimensions to optimize for low insertion loss. The number of AWs is calculated from the angle that encompasses 99 % of the power from the input/output (IO) channel waveguide propagation into the FPR. Widths of the AWs and IO waveguides at the FPR interface ($w_{\text{AW-FPR}}$ and $w_{\text{io-FPR}}$) are chose to support only one symmetric TE mode. For optimizing the insertion loss, it is important to minimize the excitation from the grating aside from the designed interference order. For these SOI waveguides, $w_{\text{AW-FPR}}$ can be reduced further to decrease the pitch of the AWs, since the separation of the AWs is set to the minimum feature size of the lithography process: 0.3 µm. The pitch between i/o waveguides ($d_{\text{io-FPR}}$) is initially approximated to be twice $w_{\text{io-FPR}}$. Reducing $d_{\text{io-FPR}}$ during the iterative optimization increases the adjacent channel crosstalk, but also decreases the number of AWs, and consequently the accumulated phase and amplitude errors. These effects are then balanced to achieve a minimum loss. The channel

Table 4.4: Design and layout parameters for each 2.0-µm AWG.

Number of channels	N_{ch}	8
Number of AWs	N_{AW}	157
Rowland radius	r	241.69 µm
AW length increment	ΔL	19.56 µm
i/o waveguide length	L_{io}	1.60 mm
AW width	w_{AW}	1.20 µm
AW width at FPR	$w_{\text{AW-FPR}}$	1.00 µm
i/o waveguide width	w_{io}	0.80 µm
i/o waveguide width at FPR	$w_{\text{io-FPR}}$	1.40 µm
AW pitch at FPR	$d_{\text{c,AW}}$	1.25 µm
i/o waveguide pitch at FPR	$d_{\text{c,io}}$	4.20 µm
Footprint area	S	$\sim$3.68 mm^2
Center wavelength	λ_{c}	2012 nm

uniformity is another parameter that can be modified, since this value also affects the number of waveguides and a similar optimization process can be implemented to further reduce the total on-chip loss.

4.5.2 Fabrication and methods

The devices are fabricated on a Si-on-insulator (SOI) platform [89]. As shown in Fig. 4.18(a), a 0.50-µm thick Si layer is used with a 1.00-µm thick SiO_2 bottom cladding. Features are defined with deep-ultraviolet lithography and reactive ion etching with sulfur hexafluoride, oxygen, and argon ($SF_6/O_2/Ar$) to remove 0.25 µm of Si. A 4:1 mixture of sulfuric acid and hydrogen peroxide held at 80 °C strips the photoresist. A 1.00-µm thick SiO_2 layer is then sputtered to form the top cladding before dicing the wafer and polishing the facets. Micrographs of the AWG and AWG-ring are shown in Fig. 4.18(b) and Fig. 4.18(c), respectively. The free propagation region (FPR) with the de-multiplexed and the AWs is schematized in Fig. 4.18(d), defining the design parameters that are listed in Table 4.4. Other parameters include the number of channels (8) and AWs (157). A flared and angled facet waveguide, schematized in Fig. 4.18(e), reduces the fundamental

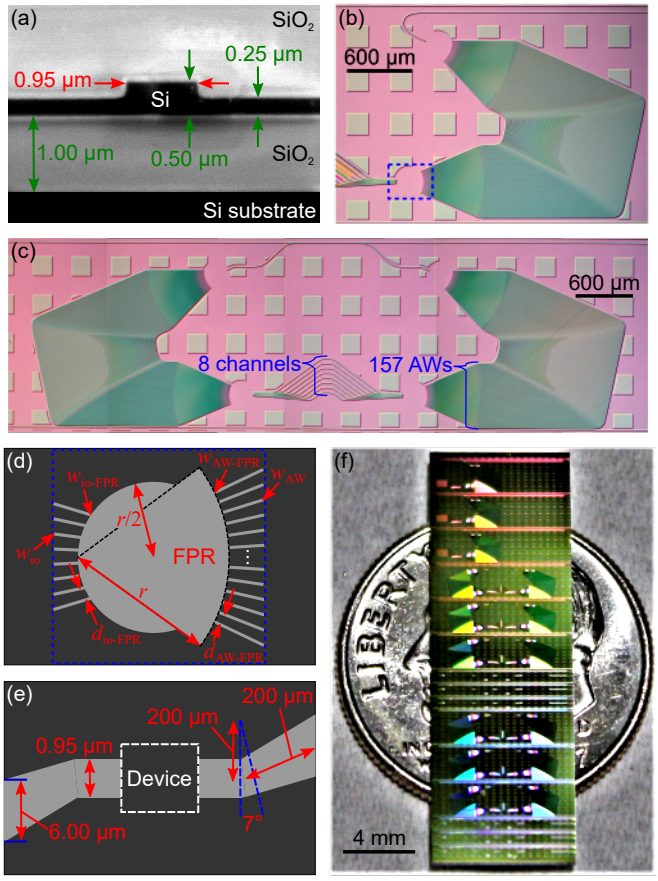

Figure 4.18: (a) Cross-section SEM of a single-mode Si waveguide. Micrographs (b) of an AWG and (c) of an AWG-ring. The FPR region outlined with blue in (b) is schematized in (d). (e) Top-view schematic of the facet coupling design. (f) Photograph of the chip on top of a U.S. dime for scale.

mode reflection compared to a normal angle at the facet. This suppresses the Fabry-Perot resonance amplitude so it does not affect the AWG and AWG-ring transmission spectra. Three copies of each device are photographed on a single chip in Fig. 4.18(f).

The experimental setup is shown in Fig. 4.19. Light from a diode tunable laser (TL, Newport Velocity TLB-6736) in the wavelength range 2.004–2.022 μm (driven by a Keithley 2400 SourceMeter) is coupled to a single-mode fiber with an aspheric lens. A polarization controller (PC, Thorlabs PLC-900) is used to excite a transverse-electric (TE) on-chip mode. The light is launched into the integrated waveguide from a

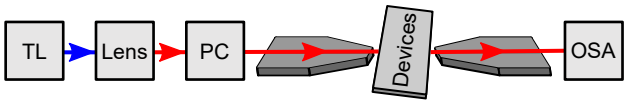

Figure 4.19: Schematic of the experimental setup used to measure the transmission spectra of the devices. The red lines indicate single-mode fibers and the blue one represents a free-space collimated beam.

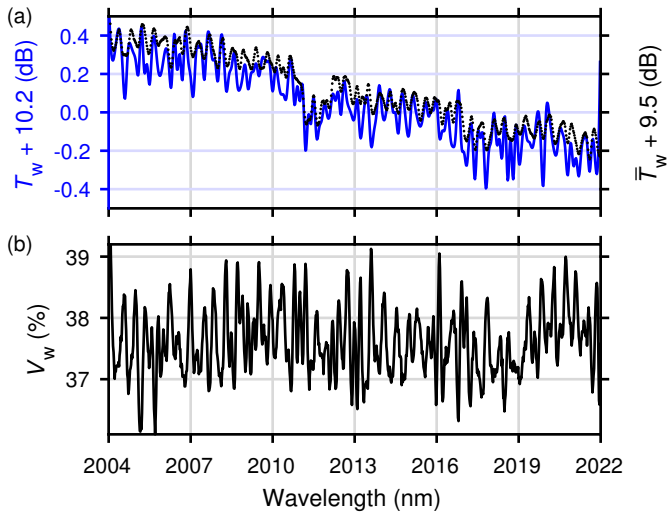

Figure 4.20: (a) Transmission spectrum (in black) averaged over thirteen straight waveguides, and example (in blue). (b) Spectrum of the coefficient of variation V_{w}, calculated from all straight waveguide transmission spectra.

lensed fiber (OZ Optics) with an anti-reflective coating centered at 2.0-µm wavelength. A temperature controller (Newport LDT-5948) holds the chip at 25 °C. The transmitted light is collected with another lensed fiber and measured with an optical spectrum analyzer (OSA, Yokogawa AQ6375).

4.5.3 Experiment and results

The transmission spectra of thirteen straight waveguides are measured to investigate the off- to on-chip coupling efficiency and variation. One example transmission spectrum of these waveguides is presented in Fig. 4.20(a) in blue and the mean transmission spectrum is shown in black, from which a coupling loss of ∼4.5 dB per facet is extracted.

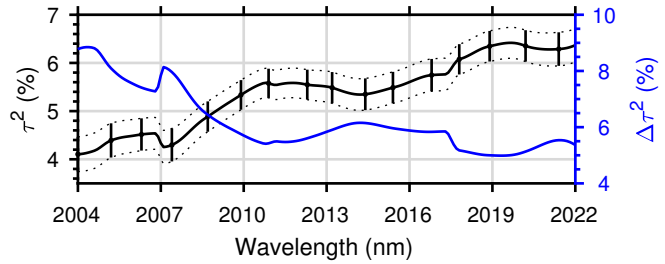

Figure 4.21: Spectrum of the transmission coefficient τ^2 for coupling to the AWG-ring, extracted from the spectra of a UMZI, is plotted in black. The uncertainty on this parameter is plotted in blue.

Table 4.5: Summary of on-chip SWIR AWG transmission t_a.

Method	Δt_a (%)	$\overline{\text{XT}}$ (dB)	L_{min} (dB)	L_{max} (dB)
(4.12a)	9.02	−30.82(0.39)	2.12(0.39)	1.85(1.42)
(4.12b)	6.00	−30.91(0.26)	2.26(0.26)	0.88(0.61)
(4.12c)	26.34	−30.92(1.19)	2.28(1.17)	0.56(1.70)
(4.15)	53.20	−30.94(2.60)	0.07(2.58)	0.87(4.25)

The coefficient of variation (V_w), in Fig. 4.20(b), represents the normalized standard deviation of the straight waveguide transmission. Another measurement of back-scattered light along waveguide spirals near 1.6-µm wavelength indicates that this variation is dominated by the uncertainty of the facet coupling efficiency [49]. Hence, V_w indicates the normalized uncertainty introduced by the facet coupling, which is used to extract the uncertainty of the on-chip insertion loss from the conventional and AWG-ring methods.

Transmission spectra from two ports of a chip-based unbalanced Mach-Zehnder interferometer (UMZI) are analyzed to characterize the coupler design used in the AWG-ring devices [63]. The extracted transmission coefficient, τ^2, in Fig. 4.21, is defined by the ratio of the transmitted power to the input power.

On-chip AWG transmission spectra, in Fig. 4.22, are normalized at the peak of each channel to the on-chip transmission values calculated from three separate AWG-rings. An example AWG-ring transmission is shown in Fig. 4.24, which is used along with the τ^2 values of the coupler to calculate the peak transmission of each AWG channel.

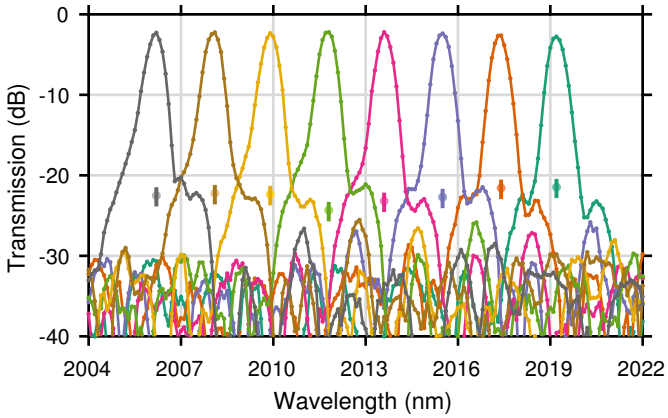

Figure 4.22: On-chip transmission spectra measured for the AWG channels, normalized using the AWG-ring method. The cumulative crosstalk within a 3-dB bandwidth of each channel peak is indicated with dots and the corresponding standard uncertainty is plotted with a vertical line.

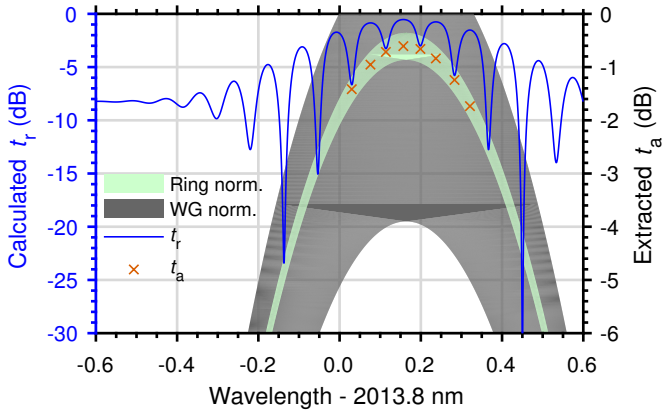

Figure 4.23: Uncertainty comparison between the waveguide normalization method and the AWG-ring method.

When cascading two AWGs, the misalignment of the channels increases the peak-channel loss relative to twice the peak-channel loss of a single AWG. The AWG-ring loss characterization method and derived uncertainty is valid and accurately characterizes the loss of the cascaded AWG structure. However, to know how the cascaded AWG loss relates to the loss of a single AWG, the misalignment must be determined. In the first analysis, measurements from other AWG test structures are used to measure this misalignment by tracking the variation of the peak-channel wavelengths. However, this

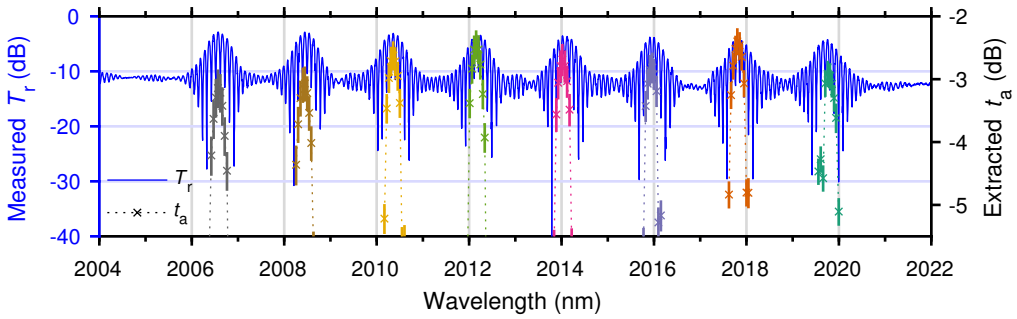

Figure 4.24: Measured transmission T_r of an AWG-ring and the extracted transmission t_a of each AWG channel.

information may also be derived directly from the AWG-ring transmission measurement by comparing the shape of the channel transmission as extracted from the AWG-ring to the shape of the single AWG channel transmission. The widening of a channel measured with the AWG-ring relative to the width of a single AWG channel is equal to twice the channel misalignment between the two AWGs in the ring. This second analysis is performed. For each channel, half of the difference between the full width at half maximum (FWHM) of the AWG-ring fit and the single AWG fit is the calculated channel misalignment. The FHWM, R^2, and misalignment values are also listed in Table 4.6. The average value is 10 pm with a standard deviation of 18 pm. These values correspond to an uncertainty of 0.1 % in the transmission, which is less than the uncertainty found with the previous method (1.6 %). Process variation across the chip can shift the channel peaks between the AWG and the AWG-ring devices. This further emphasizes that the new method of fitting the data extracted AWG-ring is more accurate than the previous method of calculating the variation from the individual AWGs.

To summarize, the central channels of the AWG have an on-chip loss of 2.2(3) dB and the uniformity across all eight channels is 0.6(5) dB, where the numbers in parentheses are the standard uncertainties referred to the corresponding last digits of the quoted results. Channel crosstalk is calculated across the 3-dB bandwidth of each channel, and

Table 4.6: Analysis of AWG channel misalignment and its affect on the transmission uncertainty.

Channel #	1	2	3	4	5	6	7	8
AWG FWHM (pm)	347	389	373	413	338	406	337	402
AWG R^2 (%)	99.1	96.6	99.5	99.7	99.4	99.9	99.4	99.8
AWG-ring FWHM (pm)	381	380	392	366	388	410	398	448
AWG-ring R^2 (%)	99.7	99.8	99.6	99.7	98.8	99.5	99.9	74.8
Misalignment (pm)	17	−5	10	−24	25	2	30	23

the average crosstalk per channel is −31 dB. The conventional normalization method is found to have ∼53.2 % relative uncertainty and the AWG-ring method reduces this value to ∼6.0 %. Channel misalignment is analyzed and found to contribute only 0.1 % to the total transmission uncertainty due to a 10-pm average misalignment between the two AWGs in the AWG-ring.

4.6 Mid-infrared arrayed waveguide grating

AWGs have been successfully demonstrated at many wavelengths in the mid-IR, including 3.8 µm [56], 5.4 µm [53], and 7.6 µm [90]. This work aims to demonstrate an AWG that is compatible with heterogeneously integrated ICLs [91].

4.6.1 Design

The mid-IR AWG on SOI design and layout parameters are list in Table 4.7. The grating order is 12, which is relatively low and is due to the long wavelength. A channel spacing of ∼8.2 nm and an FSR of ∼194 nm are designed. Grating side-order loss is estimated at 0.36 dB and the grating aperture loss is 0.09 dB.

This AWG was originally designed for ∼3.6-µm center wavelength operation for compatibility with heterogeneously integrated ICLs near that wavelength. However, a tunable laser source was not available at that wavelength to measure the transmission

Table 4.7: Design and layout parameters for each mid-IR AWG.

Number of channels	N_{ch}	8
Number of AWs	N_{AW}	119
Rowland radius	r	181.78 µm
AW length increment	ΔL	21.55 µm
AW width	w_{AW}	2.20 µm
AW width at FPR	$w_{\text{AW-FPR}}$	2.00 µm
i/o waveguide width	w_{io}	1.80 µm
i/o waveguide width at FPR	$w_{\text{io-FPR}}$	2.80 µm
AW pitch at FPR	$d_{\text{c,AW}}$	2.30 µm
i/o waveguide pitch at FPR	$d_{\text{c,io}}$	5.60 µm
Footprint area	S	3.88 mm^2
Center wavelength	λ_{c}	3965 nm

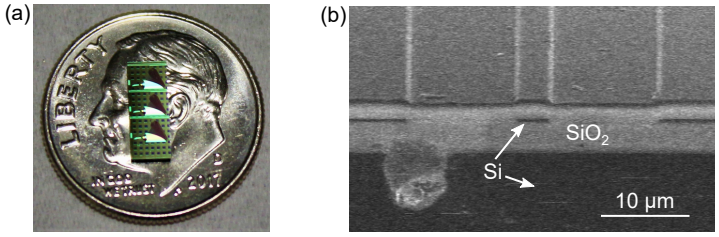

Figure 4.25: (a) Micrograph and (b) SEM of mid-IR AWG on SOI for 4.0 µm wavelength.

spectra. By operating at the 10$^{\text{th}}$ grating order, an available tunable laser in the range of 3.9–4.0 µm can be used to characterize this device.

4.6.2 Fabrication and methods

The devices in this work are fabricated on the SOI platform with a similar process flow to the near-IR and short-wave-IR AWG devices. The major difference is that a 0.22-µm thick Si layer and a 1.00-µm thick SiO_2 bottom cladding are used. This is because a multi-project fabrication run with these standard layer thicknesses was used to make these devices. An image of the AWG chip and an SEM of the output facet waveguide are shown in Fig. 4.25.

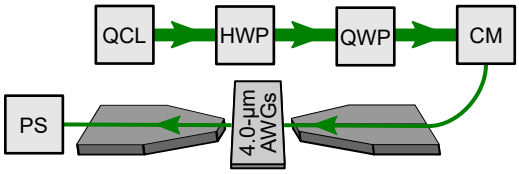

Figure 4.26: (a) Micrograph and (b) SEM of mid-IR AWG on SOI for 4.0 µm wavelength.

The test setup for the ∼4.0-µm devices is shown in Fig. 4.26(b). Light is output from a tunable quantum cascade laser (QCL, Daylight Solutions MIRcat) in the range of ∼3.92–4.01 µm and the polarization is controlled with free-space half- and quarter-wave plates (HWP, QWP) before coupling into an indium fluoride fiber via a fiber coupling mirror (FCM). The fiber is then aligned to the integrated waveguide facet using a 3-axis piezo-controlled flexure stage (Thorlabs MAX312). The transmitted light is collected with another fiber and measured measured with a power sensor (PS, Vigo PVI-4TE).

4.6.3 Experiment and results

The transmission spectra of the AWG are plotted in Fig. 4.27 with points connected by solid lines. Since the AWG is designed for 3.6 µm rather than 4.0 µm, the channels with shorter wavelength peak transmission have lower loss than the channels with longer wavelength peak transmission. This is due to a number of wavelength-dependent loss mechanisms: absorption loss in the SiO_2, substrate leakage loss, bend loss, and interfacial scattering loss. Because of this, the channel with the shortest peak-wavelength has the minimum loss of 3.36 dB and the channel with the longest peak-wavelength has the highest loss of 6.96 dB, and the non-uniformity is 3.60 dB. The average cumulative crosstalk in the 3-dB bandwidth of each channel is −23.2 dB.

The loss due material absorption and substrate leakage losses are calculated to estimate the inherent loss of the AWG design at this wavelength. Literature values of SiO_2 absorption [92] are used along with the optical confinement in the cladding

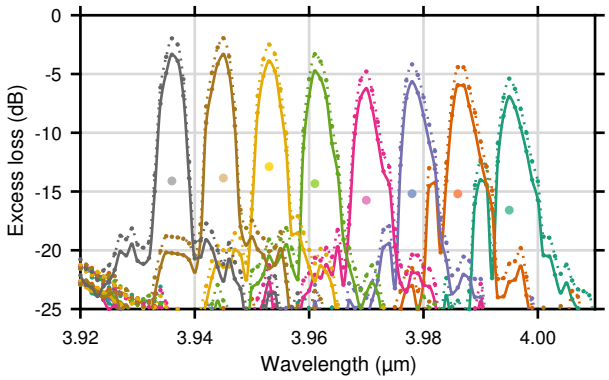

Figure 4.27: Mid-IR AWG transmission spectra.

of 49 %. Substrate leakage losses are simulated with FIMMWAVE [46]. The points connected by dashed lines in Fig. 4.27 represent the AWG transmission spectra reduced by the SiO_2 absorption and the substrate leakage loss. For these data, the minimum loss is 1.95 dB, the maximum loss is 5.40 dB, the non-uniformity is 3.45 dB, and the 3-dB cumulative crosstalk is −21.0 dB. Because of the limited mask-layout space, an investigation into the coupling loss uncertainty was not performed and only the straight-waveguide normalization was used to extract the on-chip AWG transmission.

4.7 Summary and conclusion

A comprehensive AWG design methodology is presented that prioritizes low-loss over other performance characteristics. This method is independent of the waveguide material platform and is applicable to a wide range of wavelengths, especially from the UV to the mid-IR. An important feature of this method is that the transmission spectra of the AWG can be quickly and accurately modeled, including phase and amplitude noise in the arrayed waveguides. Iteration through the design, transmission calculation, and mask layout steps allows for many inter-related design parameters to converge on an optimal set of values to minimize the AWG loss.

An AWG is demonstrated with center-wavelength at ∼760 nm with a minimum insertion loss smaller than 0.5 dB and a crosstalk of ∼23 dB. This proves the feasibility of integrated spectral beam combiners on the NOS platform in the VIS. Low insertion loss is achieved by minimizing side-order grating excitation, interfacial scattering, material absorption, and multiple sources of phase errors in the AWG. These techniques are first demonstrated at this wavelength, though they can be applied to AWG design in general to achieve low-loss beam combining at other wavelengths. Measurements of this device reveal the need to reduce measurement uncertainty so very low-loss peak channel transmissions can be characterized.

A low-loss Si AWG operating in the near-IR is demonstrated and the peak channel transmittance and crosstalk level are accurately reported. An AWG-ring is proposed and used to characterize the peak transmittance of each AWG channel. Compared to the uncertainty on t_{a} obtained with the waveguide normalization method, an improvement by 80.1 % is demonstrated with (4.12b). On-chip transmission is demonstrated in the range of 69–76 % with crosstalk per channel of −29 dB. While this work reports on a low-loss AWG, more advanced design [8] and improved fabrication [66] are expected to further reduce the loss and the crosstalk. The AWG-ring method proposed here should be used to measure incremental progress on AWG design, thus yielding significant improvements in total transmission efficiency for AWGs with large numbers of channels.

From the same process run, a low loss and crosstalk short-wave-IR AWG is demonstrated near 2.0-µm wavelength. With 500-nm thick Si waveguides [68], these AWGs are compatible with the previously demonstrated CW laser [93] and SOA [94] on Si at 2.0-µm. Additional analysis is performed to drastically reduce the measurement uncertainty by using an AWG-ring [49] to normalize the transmission of each channel. The on-chip transmission is extracted in the range of 0.49–0.59 %.

A mid-IR AWG is also demonstrated on SOI near 4.0 µm. Although the waveguide platform is not ideal for this wavelength, on-chip transmission spectra are measured with losses in the range of 3.4–7.0 dB. These devices are suitable for integration with the recently demonstrated ICL on SOI [91].

The main contributions to the field of AWGs design include the AWG-ring concept for reducing measurement uncertainty and the optimized design methodology for minimizing loss and crosstalk rather than obtaining exact channel spacing or FSR, minimizing footprint, or meeting other characteristics. One important design feature is that the AW density at the FPR interface is maximized and cross-coupling between AWs is not avoided. This differs from many other AWG designs, though simulations and experiments that the cross-coupling is not detrimental, but rather helps keep the transition between the FPR and the AWs adiabatic. Also, a new and rigorous definition of channel crosstalk has been proposed that helps to compare AWG designs with different channel numbers.

References

[1] M. K. Smit, "New focusing and dispersive planar component based on an optical phased array," Electron. Lett. **24**, 385–386 (1988).

[2] H. Takahashi, S. Suzuki, K. Kato, and I. Nishi, "Arrayed-waveguide grating for wavelength division multi/demultiplexer with nanometre resolution," Electron. Lett. **26**, 87–88 (1990).

[3] C. Dragone, "An $N \times N$ optical multiplexer using a planar arrangement of two star couplers," IEEE Photon. Technol. Lett. **3**, 812–815 (1991).

[4] K. Okamoto, K. Takiguchi, and Y. Ohmori, "16-channel optical add/drop multiplexer using silica-based arrayed-waveguide gratings," Electron. Lett. **31**, 723–724 (1995).

[5] M. J. O'Mahony, D. Simeonidou, D. K. Hunter, and A. Tzanakaki, "The application of optical packet switching in future communication networks," IEEE Commun. Mag. **39**, 128–135 (2001).

[6] H. Takahashi, S. Suzuki, and I. Nishi, "Wavelength multiplexer based on SiO_2-Ta_2O_5 arrayed-waveguide grating," J. Lightw. Technol. **12**, 989–995 (1994).

[7] M. K. Smit and C. Van Dam, "PHASAR-based WDM-devices: Principles, design and applications," IEEE J. Sel. Topics Quantum Electron. **2**, 236–250 (1996).

[8] A. Sugita, A. Kaneko, K. Okamoto, M. Itoh, A. Himeno, and Y. Ohmori, "Very low insertion loss arrayed-waveguide grating with vertically tapered waveguides," IEEE Photon. Technol. Lett. **12**, 1180–1182 (2000).

[9] K. Sasaki, F. Ohno, A. Motegi, and T. Baba, "Arrayed waveguide grating of 70 $\times$ 60 μm^2 size based on Si photonic wire waveguides," Electron. Lett. **41**, 801–802 (2005).

[10] K. Okamoto, "Progress and technical challenge for planar waveguide devices: silica and silicon waveguides," Laser Photon. Rev. **6**, 14–23 (2012).

[11] S. Pathak, M. Vanslembrouck, P. Dumon, D. Van Thourhout, P. Verheyen, G. Lepage, P. Absil, and W. Bogaerts, "Effect of mask discretization on performance of silicon arrayed waveguide gratings," IEEE Photon. Technol. Lett. **26**, 718–721 (2014).

[12] J. F. Bauters, J. R. Adleman, M. J. Heck, and J. E. Bowers, "Design and characterization of arrayed waveguide gratings using ultra-low loss si3n4 waveguides," Appl. Phys. A **116**, 427–432 (2014).

[13] E. Stanton, A. Spott, M. Davenport, N. Volet, and J. Bowers, "Low-loss arrayed waveguide grating at 760 nm," Opt. Lett. **41**, 1785–1788 (2016).

[14] P. Cheben, J. Schmid, A. Delâge, A. Densmore, S. Janz, B. Lamontagne, J. Lapointe, E. Post, P. Waldron, and D.-X. Xu, "A high-resolution silicon-on-insulator arrayed waveguide grating microspectrometer with sub-micrometer aperture waveguides," Opt. Express **15**, 2299–2306 (2007).

[15] B. G. Lee, J. Kansky, A. K. Goyal, C. Pflügl, L. Diehl, M. A. Belkin, A. Sanchez, and F. A. Capasso, "Beam combining of quantum cascade laser arrays," Opt. Express **17**, 16216–16224 (2009).

[16] Z. Hu, A. Glidle, C. N. Ironside, M. Sorel, M. J. Strain, J. Cooper, and H. Yin, "Integrated microspectrometer for fluorescence based analysis in a microfluidic format," Lab Chip **12**, 2850–2857 (2012).

[17] B. I. Akca, B. Považay, A. Alex, K. Wörhoff, R. M. de Ridder, W. Drexler, and M. Pollnau, "Miniature spectrometer and beam splitter for an optical coherence tomography on a silicon chip," Opt. Express **21**, 16648–16656 (2013).

[18] A. Z. Subramanian, E. Ryckeboer, A. Dhakal, F. Peyskens, A. Malik, B. Kuyken, H. Zhao, S. Pathak, A. Ruocco, A. De Groote, P. Wuytens, D. Martens, F. Leo, W. Xie, U. D. Dave, M. Muneeb, P. Van Dorpe, J. Van Campenhout, W. Bogaerts, P. Bienstman, N. Le Thomas, D. Van Thourhout, Z. Hens, G. Roelkens, and R. Baets, "Silicon and silicon nitride photonic circuits for spectroscopic sensing on-a-chip," Photon. Res. **3**, B47–B59 (2015).

[19] A. Stoll, Z. Zhang, R. Haynes, and M. Roth, "High-Resolution Arrayed-Waveguide-Gratings in Astronomy: Design and Fabrication Challenges," Photonics **4**, 30 (2017).

[20] G. Carpintero, E. Rouvalis, K. Ławniczuk, M. Fice, C. C. Renaud, X. J. Leijtens, E. A. Bente, M. Chitoui, F. Van Dijk, and A. J. Seeds, "95 GHz millimeter wave signal generation using an arrayed waveguide grating dual wavelength semiconductor laser," Opt. Lett. **37**, 3657–3659 (2012).

[21] E. J. Stanton, M. J. Heck, J. Bovington, A. Spott, and J. E. Bowers, "Multi-octave spectral beam combiner on ultra-broadband photonic integrated circuit platform," Opt. Express **23**, 11272–11283 (2015).

[22] M. Kohtoku, H. Sanjoh, S. Oku, Y. Kadota, Y. Yoshikuni, and Y. Shibata, "InP-based 64-channel arrayed waveguide grating with 50 GHz channel spacing and up to −20 dB crosstalk," Electron. Lett. **33**, 1786–1787 (1997).

[23] B. I. Akca, C. R. Doerr, G. Sengo, K. Wörhoff, M. Pollnau, and R. M. de Ridder, "Broad-spectral-range synchronized flat-top arrayed-waveguide grating applied in a 225-channel cascaded spectrometer," Opt. Express **20**, 18313–18318 (2012).

[24] T. Y. Fan, "Laser beam combining for high-power, high-radiance sources," IEEE J. Sel. Topics Quantum Electron. **11**, 567–577 (2005).

[25] G. Kurczveil, M. J. R. Heck, J. D. Peters, J. M. Garcia, D. Spencer, and J. E. Bowers, "An integrated hybrid silicon multiwavelength AWG laser," IEEE J. Sel. Topics Quantum Electron. **17**, 1521–1527 (2011).

[26] G. Roelkens, U. Dave, A. Gassenq, N. Hattasan, C. Hu, B. Kuyken, F. Leo, A. Malik, M. Muneeb, E. Ryckeboer, D. Sanchez, S. Uvin, R. Wang, Z. Hens, R. Baets, Y. Shimura, F. Gencarelli, B. Vincent, R. Loo, J. Van Campenhout, L. Cerutti, J.-B. Rodriguez, E. Tournie, X. Chen, M. Nedeljkovic, G. Mashanovich, L. Shen, N. Healy, A. Peacock, X. Liu, R. Osgood, and W. Green, "Silicon-Based Photonic Integration Beyond the Telecommunication Wavelength Range," IEEE J. Sel. Topics Quantum Electron. **20**, 394–404 (2014).

[27] P. Trinh, S. Yegnanarayanan, F. Coppinger, and B. Jalali, "Silicon-on-insulator (SOI) phased-array wavelength multi/demultiplexer with extremely low-polarization sensitivity," IEEE Photon. Technol. Lett. **9**, 940–942 (1997).

[28] D. Dai, Z. Wang, J. F. Bauters, M.-C. Tien, M. J. R. Heck, D. J. Blumenthal, and J. E. Bowers, "Low-loss si_3n_4 arrayed-waveguide grating (de)multiplexer using nano-core optical waveguides," Opt. Express **19**, 14130–14136 (2011).

[29] M. J. Heck, J. F. Bauters, M. L. Davenport, J. K. Doylend, S. Jain, G. Kurczveil, S. Srinivasan, Y. Tang, and J. E. Bowers, "Hybrid silicon photonic integrated circuit technology," IEEE J. Sel. Topics Quantum Electron. **19**, 6100117 (2013).

[30] P. Dong, Y.-K. Chen, G.-H. Duan, and D. T. Neilson, "Silicon photonic devices and integrated circuits," Nanophotonics **3**, 215–228 (2014).

[31] A. W. Fang, H. Park, O. Cohen, R. Jones, M. J. Paniccia, and J. E. Bowers, "Electrically pumped hybrid AlGaInAs-silicon evanescent laser," Opt. Express **14**, 9203–9210 (2006).

[32] D. Liang and J. E. Bowers, "Recent progress in lasers on silicon," Nat. Phot. **4**, 511–517 (2010).

[33] G. Roelkens, A. Abassi, P. Cardile, U. Dave, A. De Groote, Y. De Koninck, S. Dhoore, X. Fu, A. Gassenq, N. Hattasan, Q. Huang, S. Kumari, S. Keyvaninia, B. Kuyken, L. Li, P. Mechet, M. Muneeb, D. Sanchez, H. Shao, T. Spuesens, A. Z. Subramanian, S. Uvin, M. Tassaert, K. van Gasse, J. Verbist, R. Wang, Z. Wang, J. Zhang, J. van Campenhout, X. Yin, J. Bauwelinck, G. Morthier, R. Baets, and D. van Thourhout, "III-V-on-Silicon Photonic Devices for Optical Communication and Sensing," Photonics **2**, 969–1004 (2015).

[34] P. Pottier, M. J. Strain, and M. Packirisamy, "Integrated microspectrometer with elliptical Bragg mirror enhanced diffraction grating on silicon on insulator," ACS Photonics **1**, 430–436 (2014).

[35] A. Y. Piggott, J. Lu, K. G. Lagoudakis, J. Petykiewicz, T. M. Babinec, and J. Vučković, "Inverse design and demonstration of a compact and broadband on-chip wavelength demultiplexer," Nat. Photon. **9**, 374–377 (2015).

[36] S. Pathak, D. Van Thourhout, and W. Bogaerts, "Design trade-offs for silicon-on-insulator-based AWGs for (de)multiplexer applications," Opt. Lett. **38**, 2961–2964 (2013).

[37] T. Barwicz and H. A. Haus, "Three-dimensional analysis of scattering losses due to sidewall roughness in microphotonic waveguides," J. Lightw. Technol. **23**, 2719 (2005).

[38] Y. Komai, H. Nagano, K. Okamoto, and K. Kodate, "Compact spectroscopic sensor using a visible arrayed waveguide grating," Jpn. J. Appl. Phys. **45**, 6742 (2006).

[39] B. Schauwecker, G. Przyrembel, B. Kuhlow, and C. Radehaus, "Small-size silicon-oxynitride AWG demultiplexer operating around 725 nm," IEEE Photon. Technol. Lett. **12**, 1645–1646 (2000).

[40] D. Martens, A. Z. Subramanian, S. Pathak, M. Vanslembrouck, P. Bienstman, W. Bogaerts, and R. G. Baets, "Compact Silicon Nitride Arrayed Waveguide Gratings for Very Near-Infrared Wavelengths," IEEE Photon. Technol. Lett. **27**, 137–140 (2015).

[41] J. F. Bauters, M. J. Heck, D. John, D. Dai, M.-C. Tien, J. S. Barton, A. Leinse, R. G. Heideman, D. J. Blumenthal, and J. E. Bowers, "Ultra-low-loss high-aspect-ratio Si_3N_4 waveguides," Opt. Express **19**, 3163–3174 (2011).

[42] J. F. Bauters, M. J. Heck, D. D. John, J. S. Barton, C. M. Bruinink, A. Leinse, R. G. Heideman, D. J. Blumenthal, and J. E. Bowers, "Planar waveguides with less than 0.1 dB/m propagation loss fabricated with wafer bonding," Opt. Express **19**, 24090–24101 (2011).

[43] C. D. Lee, W. Chen, Q. Wang, Y.-J. Chen, W. T. Beard, D. Stone, R. F. Smith, R. Mincher, and I. R. Stewart, "The role of photomask resolution on the performance of arrayed-waveguide grating devices," J. Lightw. Technol. **19**, 1726 (2001).

[44] J. T. Bovington, M. J. R. Heck, and J. E. Bowers, "Heterogeneous lasers and coupling to Si_3N_4 near 1060 nm," Opt. Lett. **39**, 6017–6020 (2014).

[45] T. Goh, S. Suzuki, and A. Sugita, "Estimation of waveguide phase error in silica-based waveguides," J. Lightw. Technol. **15**, 2107–2113 (1997).

[46] www.photond.com.

[47] C. Ciminelli, V. M. Passaro, F. Dell'Olio, and M. N. Armenise, "Three-dimensional modelling of scattering loss in InGaAsP/InP and silica-on-silicon bent waveguides," J. Eur. Opt. Soc. Rapid Publ. **4** (2009).

[48] J. K. Hsiao, "Normalized relationship among errors and sidelobe levels," Radio Sci. **19**, 292–302 (1984).

[49] E. J. Stanton, N. Volet, and J. E. Bowers, "Low-loss demonstration and refined characterization of silicon arrayed waveguide gratings in the near-infrared," Opt. Express **25**, 30651–30663 (2017).

[50] J. H. den Besten, M. P. Dessens, C. G. P. Herben, X. J. M. Leijtens, F. H. Groen, M. R. Leys, and M. K. Smit, "Low-loss, compact, and polarization independent PHASAR demultiplexer fabricated by using a double-etch process," IEEE Photon. Technol. Lett. **14**, 62–64 (2002).

[51] C. R. Doerr, L. Zhang, and P. J. Winzer, "Monolithic InP multiwavelength coherent receiver using a chirped arrayed waveguide grating," J. Lightw. Technol. **29**, 536–541 (2011).

[52] S. Janz, D.-X. Xu, J.-M. Baribeau, A. Delage, and R. L. Williams, "$Si/Si_{1-x}Ge_x$ waveguide components for WDM demultiplexing," Proc. SPIE **3630**, 106–114 (1999).

[53] A. Malik, M. Muneeb, S. Pathak, Y. Shimura, J. Van Campenhout, R. Loo, and G. Roelkens, "Germanium-on-Silicon Mid-Infrared Arrayed Waveguide Grating Multiplexers," IEEE Photon. Technol. Lett. **25**, 1805–1808 (2013).

[54] P. Barritault, M. Brun, P. Labeye, J.-M. Hartmann, F. Boulila, M. Carras, and S. Nicoletti, "Design, fabrication and characterization of an AWG at 4.5 µm," Opt. Express **23**, 26168–26181 (2015).

[55] W. Bogaerts, S. K. Selvaraja, P. Dumon, J. Brouckaert, K. De Vos, D. Van Thourhout, and R. Baets, "Silicon-on-Insulator Spectral Filters Fabricated With CMOS Technology," IEEE J. Sel. Topics Quantum Electron. **16**, 33–44 (2010).

[56] M. Muneeb, X. Chen, P. Verheyen, G. Lepage, S. Pathak, E. Ryckeboer, A. Malik, B. Kuyken, M. Nedeljkovic, J. Van Campenhout, G. Z. Mashanovich, and G. Roelkens, "Demonstration of Silicon-on-insulator mid-infrared spectrometers operating at 3.8 µm," Opt. Express **21**, 11659–11669 (2013).

[57] J. Wang, Z. Sheng, L. Li, A. Pang, A. Wu, W. Li, X. Wang, S. Zou, M. Qi, and F. Gan, "Low-loss and low-crosstalk 8×8 silicon nanowire AWG routers fabricated with CMOS technology," Opt. Express **22**, 9395–9403 (2014).

[58] G. Tittelbach, B. Richter, and W. Karthe, "Comparison of three transmission methods for integrated optical waveguide propagation loss measurement," Pure Appl. Opt. **2**, 683–706 (1993).

[59] R. Adar, Y. Shani, C. H. Henry, R. C. Kistler, G. E. Blonder, and N. A. Olsson, "Measurement of very low-loss silica on silicon waveguides with a ring resonator," Appl. Phys. Lett. **58**, 444–445 (1991).

[60] D. J. W. Klunder, F. S. Tan, T. van der Veen, H. F. Bulthuis, G. Sengo, B. Docter, H. J. W. M. Hoekstra, and A. Driessen, "Experimental and numerical study of SiON microresonators with air and polymer cladding," J. Lightw. Technol. **21**, 1099–1110 (2003).

[61] A. Yariv, "Universal relations for coupling of optical power between microresonators and dielectric waveguides," Electron. Lett. **36**, 321–322 (2000).

[62] Z. Shi and R. W. Boyd, "Fundamental limits to slow-light arrayed-waveguide-grating spectrometers," Opt. Express **21**, 7793–7798 (2013).

[63] M. A. Tran, T. Komljenovic, J. C. Hulme, M. L. Davenport, and J. E. Bowers, "A robust method for characterization of optical waveguides and couplers," IEEE Photon. Technol. Lett. **28**, 1517–1520 (2016).

[64] W. Eickhoff and R. Ulrich, "Optical frequency domain reflectometry in single-mode fiber," Appl. Phys. Lett. **39**, 693–695 (1981).

[65] W. Hürlimann, "Coefficient of variation–I, II," in "Encyclopedia of Statistical Sciences," vol. 2, S. Kotz, C. B. Read, N. Balakrishnan, and B. Vidakovic, eds. (John Wiley & Sons, Inc., 2006), pp. 1031–1035, 2nd ed.

[66] G. Li, J. Yao, H. Thacker, A. Mekis, X. Zheng, I. Shubin, Y. Luo, J.-H. Lee, K. Raj, J. E. Cunningham, and A. V. Krishnamoorthy, "Ultralow-loss, high-density SOI optical waveguide routing for macrochip interconnects," Opt. Express **20**, 12035–12039 (2012).

[67] W. A. Zortman, D. C. Trotter, and M. R. Watts, "Silicon photonics manufacturing," Opt. Express **18**, 23598–23607 (2010).

[68] E. J. Stanton, N. Volet, and J. E. Bowers, "Silicon arrayed waveguide gratings at 2.0-µm wavelength characterized with an on-chip resonator," Opt. Lett. **in press** (2017).

[69] C. Gilles, L. J. Orbe, G. Carpintero, G. Maisons, and M. Carras, "Mid-infrared wavelength multiplexer in InGaAs/InP waveguides using a Rowland circle grating," Opt. Express **23**, 20288–20296 (2015).

[70] P. J. Roberts, F. Couny, H. Sabert, B. J. Mangan, D. P. Williams, L. Farr, M. W. Mason, A. Tomlinson, T. A. Birks, J. C. Knight, and P. St. J. Russell, "Ultimate low loss of hollow-core photonic crystal fibres," Opt. Express **13**, 236–244 (2005).

[71] Y. Chen, Z. Liu, S. R. Sandoghchi, G. T. Jasion, T. D. Bradley, E. N. Fokoua, J. R. Hayes, N. V. Wheeler, D. R. Gray, B. J. Mangan, R. Slavìk, F. Poletti, M. N. Petrovich, and D. J. Richardson, "Multi-kilometer long, longitudinally uniform hollow core photonic bandgap fibers for broadband low latency data transmission," J. Lightw. Technol. **34**, 104–113 (2016).

[72] A. Khan, D. Schaefer, L. Tao, D. J. Miller, K. Sun, M. A. Zondlo, W. A. Harrison, B. Roscoe, and D. J. Lary, "Low power greenhouse gas sensors for unmanned aerial vehicles," Remote Sens. **4**, 1355–1368 (2012).

[73] R. J. De Young and N. P. Barnes, "Profiling atmospheric water vapor using a fiber laser lidar system," Appl. Opt. **49**, 562–567 (2010).

[74] S. Ishii, K. Mizutani, H. Fukuoka, T. Ishikawa, B. Philippe, H. Iwai, T. Aoki, T. Itabe, A. Sato, and K. Asai, "Coherent 2 µm differential absorption and wind lidar with conductively cooled laser and two-axis scanning device," Appl. Opt. **49**, 1809–1817 (2010).

[75] K. Scholle, S. Lamrini, P. Koopmann, and P. Fuhrberg, "2 µm laser sources and their possible applications," in "Frontiers in Guided Wave Optics and Optoelectronics," B. Pal, ed. (InTech, 2010), chap. 21, pp. 471–500.

[76] N. V. Alexeeva and M. A. Arnold, "Near-infrared microspectroscopic analysis of rat skin tissue heterogeneity in relation to noninvasive glucose sensing," J. Diabetes Sci. Technol. **3**, 219–232 (2009).

[77] B. Chen, S. L. Thomsen, R. J. Thomas, J. Oliver, and A. J. Welch, "Histological and modeling study of skin thermal injury to 2.0 µm laser irradiation," Lasers Surg. Med. **40**, 358–370 (2008).

[78] H. K. Choi and S. J. Eglash, "High-power multiple-quantum-well GaInAsSb/-AlGaAsSb diode lasers emitting at 2.1 µm with low threshold current density," Appl. Phys. Lett. **61**, 1154–1156 (1992).

[79] M. Sakamoto, J. G. Endriz, and D. R. Scifres, "120 W CW output power from monolithic AlGaAs (800 nm) laser diode array mounted on diamond heatsink," Electron. Lett. **28**, 197–199 (1992).

[80] H. Yoshida, Y. Yamashita, M. Kuwabara, and H. Kan, "A 342-nm ultraviolet AlGaN multiple-quantum-well laser diode," Nat. Photon. **2**, 551–554 (2008).

[81] M. Kim, C. L. Canedy, W. W. Bewley, C. S. Kim, J. R. Lindle, J. Abell, I. Vurgaftman, and J. R. Meyer, "Interband cascade laser emitting at $\lambda = 3.75$ µm in continuous wave above room temperature," Appl. Phys. Lett. **92**, 191110 (2008).

[82] W. W. Bewley, C. L. Canedy, C. S. Kim, M. Kim, C. D. Merritt, J. Abell, I. Vurgaftman, and J. R. Meyer, "High-power room-temperature continuous-wave mid-infrared interband cascade lasers," Opt. Express **20**, 20894–20901 (2012).

[83] Y. Yao, A. J. Hoffman, and C. F. Gmachl, "Mid-infrared quantum cascade lasers," Nat. Photon. **6**, 432–439 (2012).

[84] H. Zhang, M. Gleeson, N. Ye, N. Pavarelli, X. Ouyang, J. Zhao, N. Kavanagh, C. Robert, H. Yang, P. Morrissey, T. K, A. Gocalinska, Y. Chen, T. Bradley, J. Wooler, J. Hayes, E. Numkam Fokoua, Z. Li, S. Alam, F. Poletti, M. Petrovich, D. Richardson, B. Kelly, J. O'Carrol, R. Phelan, E. Pelucchi, P. O'Brian, F. Peters, B. Corbett, and F. Gunning, "Dense WDM transmission at 2 µm enabled by an arrayed waveguide grating," Opt. Lett. **40**, 3308–3311 (2015).

[85] R. A. Soref, S. J. Emelett, and W. R. Buchwald, "Silicon waveguided components for the long-wave infrared region," J. Opt. A: Pure Appl. Opt. **8**, 840–848 (2006).

[86] A. D. Bristow, N. Rotenberg, and H. M. Van Driel, "Two-photon absorption and Kerr coefficients of silicon for 850–2200 nm," Appl. Phys. Lett. **90**, 191104 (2007).

[87] R. Wang, M. Muneeb, S. Sprengel, G. Boehm, A. Malik, R. Baets, M.-C. Amann, and G. Roelkens, "III-V-on-silicon 2-µm-wavelength-range wavelength demultiplexers with heterogeneously integrated InP-based type-II photodetectors," Opt. Express **24**, 8480–8490 (2016).

[88] R. Wang, A. Vasiliev, M. Muneeb, A. Malik, S. Sprengel, G. Boehm, M.-C. Amann, I. Šimonytė, A. Vizbaras, K. Vizbaras, R. Baets, and G. Roelkens, "III–V-on-Silicon Photonic Integrated Circuits for Spectroscopic Sensing in the 2–4 µm Wavelength Range," Sensors **17**, 1788 (2017).

[89] K. Okamoto, "Wavelength-division-multiplexing devices in thin SOI: Advances and prospects," IEEE J. Sel. Topics Quantum Electron. **20**, 1–10 (2014).

[90] A. Koshkinbayeva, P. Barritault, S. Ortiz, S. Boutami, M. Brun, J.-M. Hartmann, P. Brianceau, O. Lartigue, F. Boulila, R. Orobtchouk, and P. Labeye, "Impact of Non-Central Input in $N \times M$ Mid-IR Arrayed Waveguide Gratings Integrated on Si," IEEE Photon. Technol. Lett. **28**, 2191–2194 (2016).

[91] A. Spott, E. J. Stanton, A. Torres, M. L. Davenport, C. L. Canedy, I. Vurgaftman, M. Kim, C. S. Kim, C. D. Merritt, W. W. Bewley, J. R. Meyer, and J. E. Bowers, "Interband Cascade Laser on Silicon," in "2017 IEEE Photonics Conference (IPC)," (Lake Buena Vista, Florida), Post-Deadline Paper.

[92] S. A. Miller, M. Yu, X. Ji, A. G. Griffith, J. Cardenas, A. L. Gaeta, and M. Lipson, "Low-loss silicon platform for broadband mid-infrared photonics," Optica **4**, 707–712 (2017).

[93] A. Spott, M. Davenport, J. Peters, J. Bovington, M. J. R. Heck, E. J. Stanton, I. Vurgaftman, J. Meyer, and J. Bowers, "Heterogeneously integrated 2.0 µm CW hybrid silicon lasers at room temperature," Opt. Lett. **40**, 1480–1483 (2015).

[94] N. Volet, A. Spott, E. J. Stanton, M. L. Davenport, L. Chang, J. D. Peters, T. C. Briles, I. Vurgaftman, J. R. Meyer, and J. E. Bowers, "Semiconductor optical amplifiers at 2.0-µm wavelength on silicon," Laser Photon. Rev. **11**, 1600165 (2017).

Chapter 5

Star couplers

5.1 Introduction

[1]High-performance integrated light detection and ranging (LIDAR) systems have recently become feasible due to advances in large-scale photonic and electronic integration [2]. In particular, CMOS-compatible Si photonics is the most promising material platform. A recent demonstration of optical beam steering reports a 0.142° spot steered $> 80°$ with 128 output channels [3]. This high-etendue light source is achieved with a large emission area and tunable angle. A star coupler [4] is one approach to create such a large array of emitters, while a tree of 1:2 splitters [5–7] is another common approach. This work demonstrates increased emission area while maintaining densely spaced emitter elements with a 1:480 star coupler using Si waveguides, which is suitable for integrated LIDAR applications.

A 1:480 star coupler is designed for high-etendue LIDAR applications and demonstrated using Si waveguides. A large 0.96-mm output aperture and dense output waveguide spacing of 2 µm allows for a narrow 0.072° far-field spot.

[1]Some of the analysis and figures in this section have been reproduced from [1] © 2017 OSA.

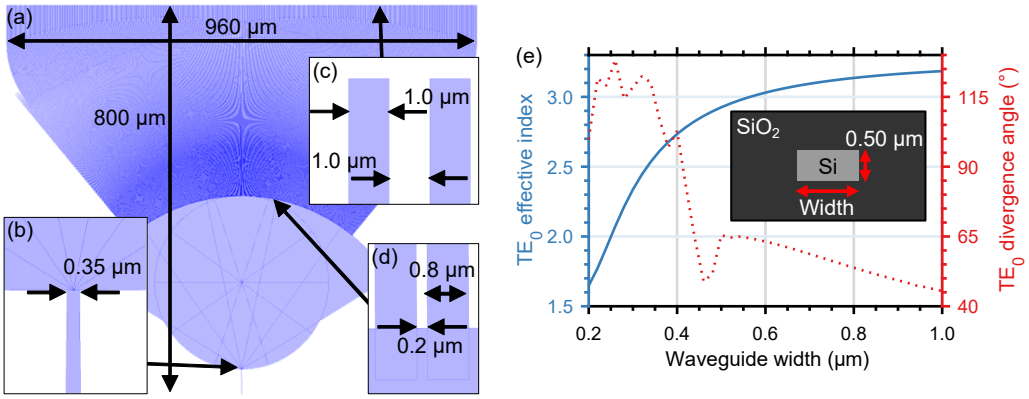

Figure 5.1: (a) Top-view of the star coupler with enlargements of the (b) input waveguide, (c) output waveguides, and (d) AWs at the FPR. (e) Calculation of the effective index and far-field 3-dB bandwidth at 1550-nm wavelength for the waveguide cross-section in the inset.

5.2 Design

The star coupler layout is detailed in Fig. 5.1(a). The input waveguide width determines the divergence angle in the free propagation region (FPR), shown in Fig. 5.1(b). With a large far-field divergence angle the device footprint is minimized to 0.77 mm^2. This initial design consideration was to maximize the far-field divergence, while avoiding a high sensitivity to fabrication variation. The angular aperture of the AWs on the opposite side of the FPR is then specified for two designs in this work at 80 % and 95 % of the far-field power. The 480 star coupler outputs with pitch of 2.00 µm, creating an output aperture of 0.96 mm, is designed for compatibility to a photonic-electronic integrated LIDAR system with a laser, phase shifters, photo-receiver, and driving electronics.

5.3 Fabrication and methods

Fabrication begins with a 100-mm diameter Si-on-insulator (SOI) wafer containing a 0.50-µm thick Si layer on top of a 1.00-µm thick buried SiO_2 layer. Features are defined

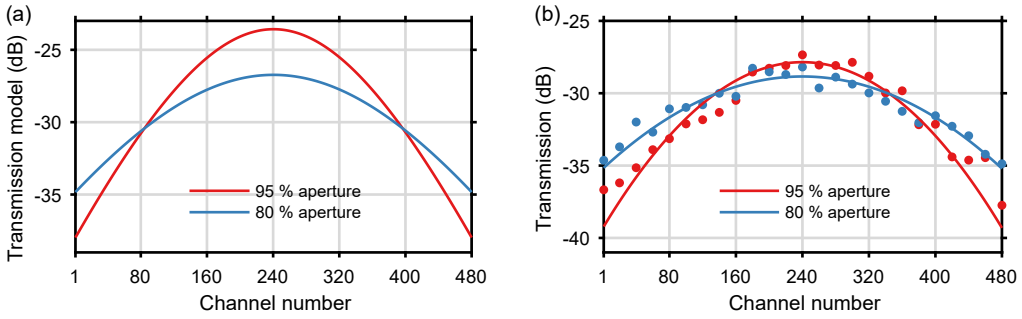

Figure 5.2: (a) Simulated transmission and (b) spectral average of measured transmission with a Gaussian fit for each of the star coupler two designs: 95 % and 80 % apertures.

with deep-ultraviolet lithography and SF_6/Ar reactive ion etching of Si. A 4:1 mixture of sulfuric acid and hydrogen peroxide held at 80 °C strips the photoresist. A 1.00-µm thick SiO_2 layer is then sputtered to form the top cladding before dicing the wafer and polishing the facets.

5.4 Experiment and results

Transmission spectra from 25 channels of the 1:480 star couplers are measured with TE light input from a tunable laser and detected with a photo-diode. For AWs at the FPR with uniform widths of 0.8 µm and pitch of 1.0 µm, varying the aperture angle changes the channel power uniformity, shown in Fig. 5.2(a). An example off-chip transmission spectra of every 20^{th} channel is plotted in Fig. 5.3. The spectral average from these data of the 95 % and 80 % aperture designs are shown in Fig. 5.2(b) with Gaussian fits to the data.

The measured non-uniformities for the 95 % and 80 % aperture designs are 11.5 dB and 6.4 dB, respectively, which agree well with the modeled values of 14.4 dB and 8.1 dB. The difference could be due to variation of the input waveguide width or continued divergence in the AWs after the FPR interface.

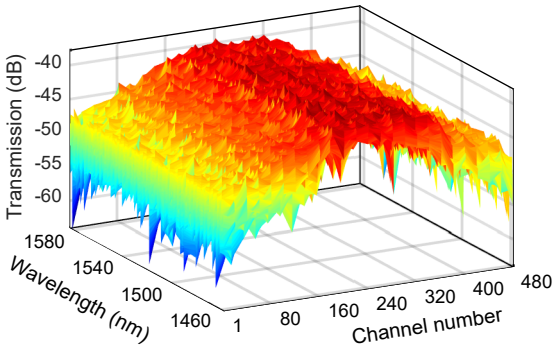

Figure 5.3: Transmission of star coupler.

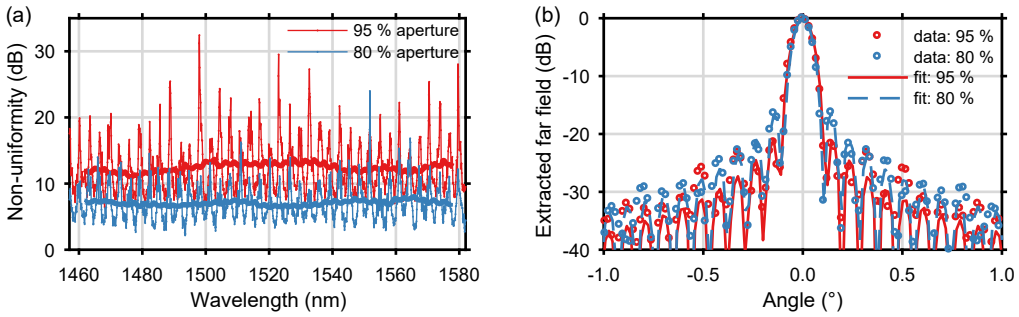

Figure 5.4: (a) Wavelength dependence of non-uniformity for each design. (b) Extracted far fields from the measured transmission (dots) and Gaussian fit (lines) at 1553 nm for each design.

In Fig. 5.4(a), a Gaussian fit is applied to the output power distribution to extract the non-uniformity across the wavelength scan. A 1-nm wide moving average, shown with thick lines in Fig. 5.4(a), indicates less than 2.7-dB. The periodic dependence is under investigation and may be due to internal reflections or cross-coupling among the AWs. The extracted far-field profiles in Fig. 5.4(b) show good agreement between the measured data and Gaussian fits at 1553-nm wavelength with $\sim$0.072° 3-dB bandwidth for each design.

The wavelength dependence on the far-field divergence angle is investigated with simulations, shown in Fig. 5.5, to determine the cause of the periodic non-uniformity. These plots suggest that for narrow waveguide widths, the far-field divergence varies sig-

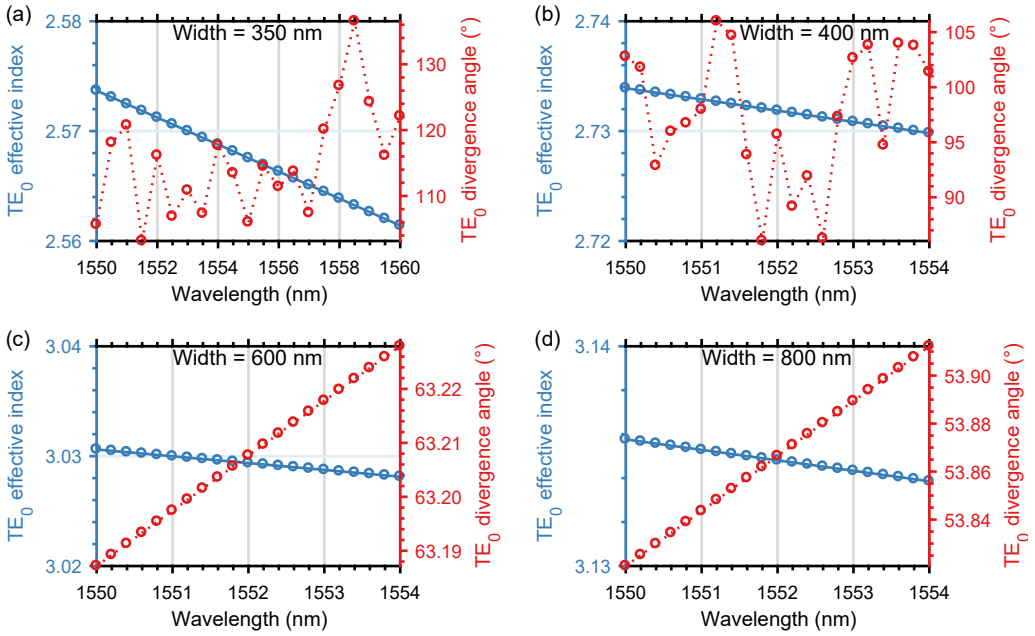

Figure 5.5: Effective indices and corresponding far-field divergence angles for (a) 350 nm, (b) 400 nm, (c) 600 nm, and (d) 800 nm waveguide widths.

nificantly with wavelength. The periodicity also matches the non-uniformity periodicity, shown in Fig. 5.4(a). A changing divergence into the FPR directly correlates to an output non-uniformity variation. Further experiments are needed to identify the exact cause of the output non-uniformity spectral dependence.

5.5 Summary and conclusion

A Si star coupler with a large, densely-spaced output aperture is demonstrated. Although a narrow input waveguide reduces the star coupler size, the non-uniformity wavelength-dependence may be a compromising feature for this device and a wider input waveguide may be necessary. Future work should investigate the output spectral dependence for wider waveguides to find the optimal value. However, this low-loss design is suitable for LIDAR application by integrating phase shifters and gratings for vertical emission.

References

[1] E. J. Stanton, N. Volet, T. Komljenovic, and J. E. Bowers, "Star coupler for high-etendue LIDAR," in "Conference on Lasers and Electro-Optics," (Optical Society of America, 2017), p. STh1M.4.

[2] T. Baehr-Jones, T. Pinguet, P. L. Guo-Qiang, S. Danziger, D. Prather, and M. Hochberg, "Myths and rumours of silicon photonics," Nat. Photon. **6**, 206–208 (2012).

[3] D. N. Hutchison, J. Sun, J. K. Doylend, R. Kumar, J. Heck, W. Kim, C. T. Phare, A. Feshali, and H. Rong, "High-resolution aliasing-free optical beam steering," Optica **3**, 887–890 (2016).

[4] C. Dragone, "Efficient $N \times N$ star couplers using Fourier optics," J. Lightw. Technol. **7**, 479–489 (1989).

[5] K. Van Acoleyen, W. Bogaerts, J. Jágerská, N. Le Thomas, R. Houdré, and R. Baets, "Off-chip beam steering with a one-dimensional optical phased array on silicon-on-insulator," Opt. Lett. **34**, 1477–1479 (2009).

[6] C. V. Poulton, M. J. Byrd, M. Raval, Z. Su, N. Li, E. Timurdogan, D. Coolbaugh, D. Vermeulen, and M. R. Watts, "Large-scale silicon nitride nanophotonic phased arrays at infrared and visible wavelengths," Opt. Lett. **42**, 21–24 (2017).

[7] J. Notaros, C. V. Poulton, M. J. Byrd, M. Raval, and M. R. Watts, "Integrated optical phased arrays for quasi-Bessel-beam generation," Opt. Lett. **42**, 3510–3513 (2017).

Chapter 6

Broadband combiners

6.1 Introduction

Integrated spectral beam combining technologies for high power broadband light sources enable technologies such as integrated spectroscopy systems [1, 2] and wide-band wavelength division multiplexing [3]. New high performance broadband technologies are also important for developments in free space communications, remote sensing, medical radiation therapy, and a host of other applications [4]. Current competitive technologies for high power broadband sources with low M^2 output use supercontinuum generation [5] or spectral beam combining [6]. Supercontinuum generation requires a high power pump to generate output through nonlinear processes. Such sources have output power and bandwidth limited by the pump power and require components that are challenging to integrate. Existing spectral beam combining technologies use free space optics to externally combine laser array output beams [7], but only narrow bandwidths are achieved. To cover multi-octave bandwidths, separate discrete laser sources are used [8].

By integrating spectral beam combining components along with multi-spectral laser sources on a single photonic chip, a broadband and scalable power source can be realized

with the advantages of photonic integration, including reduced cost, compact size, and high efficiency. Existing integration technologies cannot provide multi-spectral light generation and low loss beam combining in a single photonic chip. Different gain materials and mechanisms must be used to generate UV to mid-IR wavelengths with integrated lasers, specifically between 350 nm and 6500 nm for the application of this work. Also, no single waveguide platform practically provides low loss waveguides and spectral beam combining components across this multi-octave bandwidth. To address these challenges, multiple die bonding [9] with heterogeneous integration can be used to create multi-spectral laser sources on chip and two waveguide designs for long and short wavelength regimes. Heterogeneous integration of light sources has been demonstrated on Si spanning very-near-infrared (very-near-IR) [10], near-IR [11], and mid-IR [12]. These platforms enable such a broad spectrum of sources to be processed on a single chip [13, 14].

The multi-octave spectral beam combiner that is proposed in this work uses three stages of spectral combining: intra-band, inter-band, and ultra-broadband combining as shown in Fig. 2.1. The intra- and inter-band stages utilize common integrated photonic architectures, but the final ultra-broadband stage involves a novel approach to combine long and short wavelength regimes to a single output. By ensuring maximum fundamental mode excitation, the output will have the highest beam quality with a low M^2 value, spanning multiple octaves. Details of the standard adiabatic combiner and the multi-octave spectral beam combiner design, fabrication, experimental testing, and analysis are presented. A low insertion loss spectral beam combining is demonstrated for wavelengths spanning more than two octaves. The ultra-broadband combiner is the key element for the integrated multi-octave spectral beam combiner. Its design and demonstration shows supports the feasibility of the ultra-broadband platform.

The design of a novel platform is presented that is able to combine optical frequency bands spanning 4.2 octaves from UV to mid-IR into a single, low M^2 output waveguide.

Also, the design and realization of a key component is presented in this platform that combines the wavelength bands of 350–1500 nm and 1500–6500 nm with demonstrated efficiency greater than 90 % in near-IR and mid-IR. The multi-octave spectral beam combiner concept is realized using an integrated platform with Si_3N_4 waveguides and Si waveguides. Simulated bandwidth is shown to be over four octaves, and measured bandwidth is shown over two octaves, limited by the availability of sources.

The design of adiabatic beam combiners is introduced and demonstrated with a standard adiabatic coupler architecture for inter-band combining. This design is modified to create an ultra-broadband stage capable of combining optical frequency bands spanning 4.2 octaves from UV to mid-IR into a single, low M^2 output waveguide. Wavelength bands of 350–1500 nm and 1500–6500 nm are demonstrated with efficiency greater than 90 % in near-IR and mid-IR. The multi-octave spectral beam combiner concept is realized using an integrated platform with Si_3N_4 waveguides and Si waveguides. Simulated bandwidth is shown to be over four octaves, and measured bandwidth is shown over two octaves, limited by the availability of sources.

6.2 Design

Tapering the waveguide propagation constants along the length of a directional coupler was first proposed and analysis for microwaves [15–17]. Soon after directional couplers were first used with integrated optics [18], the tapered directional coupler, or adiabatic coupler, was demonstrated [19]. Further analysis of the tapered coupler for integrated optics obtained a criterion for the maximum permissible rate of change of the propagation constant for an efficient coupler by calculating the mode conversion between local normal modes [20, 21].

Adiabatic couplers are designed by first choosing waveguide widths that support modes across the desired wavelength range. Typically, the longest wavelength will have the highest loss since the mode will be largest and be at the threshold for incurring substrate leakage loss. The shortest wavelengths will have many cross-sectional modes in the coupler. By simulating the unperturbed modes along the length of the coupler, the mode coupling can be estimated. Finally, the design is determined after beam-propagation method (BPM) simulations to investigate the fundamental mode transmission dependence on coupler length and gap. Also, one input needs to incorporate a bend at the beginning of the device. This bend must be included in the coupler BPM simulations since coupling does start before the end of the bend region.

Adiabatic couplers that do not strongly violate the approximations of coupled mode theory [22][1] can have the transmission characteristics approximated by a closed-form calculation. However, rigorous simulations are needed to accurately predict the transmission of adiabatic couplers that do violate coupled mode theory assumptions. Beam propagation method is useful for low index contrast structures and the eigenmode expansion method is accurate and fast for calculating both low and high index contrast waveguides [23].

6.3 Adiabatic spectral duplexer

The schematic layout of an adiabatic duplexer is shown in Fig. 6.1. This basic device will couple light with a longer wavelength across the waveguide gap, and shorter wavelengths input to the other port are affected by the adjacent waveguide. Similar devices are used as 3-dB couplers by terminating the coupling section at the point where both waveguide widths equal w_{avg}. In both cases, the coupler length must be long enough

[1] These include low confinement and low mode perturbations.

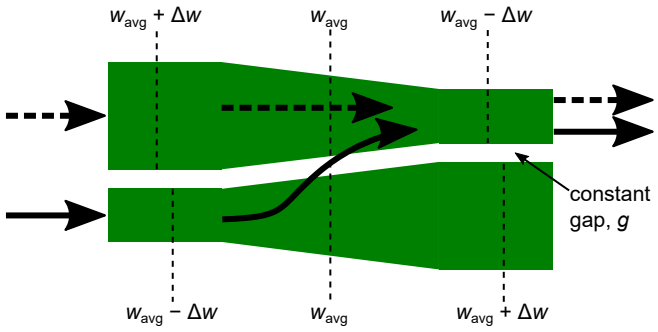

Figure 6.1: Diagram of adiabatic combiner with width designations and the general light-coupling route shown with arrows.

to exhibit the desired transmission spectra. Ideally, the transmission through the short-wavelength input T_{short} and the long-wavelength input T_{long} of an adiabatic coupler can be estimated by

$$T_{\text{short}} = \exp\left(\frac{-\pi\kappa^2}{\partial\beta/\partial z}\right), \tag{6.1a}$$

$$T_{\text{long}} = 1 - \exp\left(\frac{-\pi\kappa^2}{\partial\beta/\partial z}\right), \tag{6.1b}$$

where κ is the coupling coefficient and $\partial\beta/\partial z$ is the change in propagation constant with the length L_{coupler} along the propagation direction in the coupler. This ideal condition is only met within a limited bandwidth where coupled-mode theory approximations are valid. These assumptions break down as the wavelength is increased beyond a certain point and the transmission begins to decrease and oscillate. Simulations are used to determine these limitations.

One way to visualize the coupling between modes along the device is to plot the effective indices for each port along the length of the coupler. Two examples of these plots are given in Fig. 6.2 for 780-nm and 1550-nm wavelengths. Higher values of κ are found where effective index values match between the two waveguides. However, the mode shapes and polarization also effect this value.

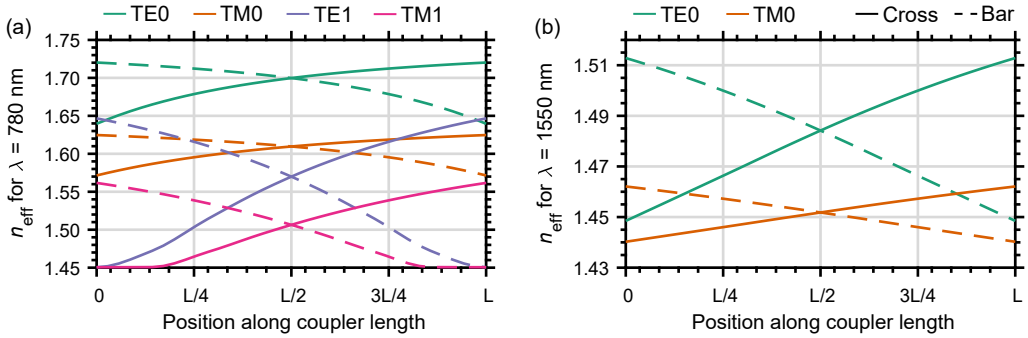

Figure 6.2: Effective indices in the bar (dashed lines) and cross (solid lines) waveguides of the adiabatic coupler as a function of position along the coupler length for (a) 780 nm and (b) 1550 nm. Each position along the coupler length corresponds to the tapered bar and cross waveguide widths as shown in Fig. 6.1 for $w_{\text{avg}} = 750$ nm and $\Delta w = 400$ nm.

Two trends of the transmission of adiabatic couplers from (6.1) are plotted in Fig. 6.3 to investigate the effect on the cross-over wavelength, which the wavelength at which the transmission through each port is equal[2]. The waveguides are based on the NOI waveguide platform with 200-nm thick Si_3N_4 and 2.0 µm thick SiO_2 bottom and top cladding layers. As the gap between waveguides increases, Fig. 6.3(a) shows how the cross-over wavelength increases and the bandwidth simultaneously decreases. To more closely analyze the bandwidth dependence, transmission spectra for various values of Δw are plotted in Fig. 6.3(b) against the deviation in frequency from the cross-over frequency. Clearly, larger values of Δw increase the cross-over bandwidth, and this occurs at the expense of increasing the coupler length to maintain adiabatic operation.

An adiabatic coupler is designed and fabricated. More details on this fabrication process and on the experimental setups are given in Section 6.4. The measured transmission spectra in the VIS at 760 nm and in the near-IR in the range of 1.3–1.6 µm are plotted along with the transmission from (6.1) in Fig. 6.4. The adiabatic coupler design parameters are $w_{\text{avg}} = 750$ nm, $\Delta w = 400$ nm, $g = 1.6$ µm, and $L_{\text{coupler}} = 1000$ µm.

[2]The transmission level at the cross-over wavelength is ideally 50 %, but this is not always observed experimentally. In some cases, this is due to excitation of higher order modes. It can also be due to loss in the coupler.

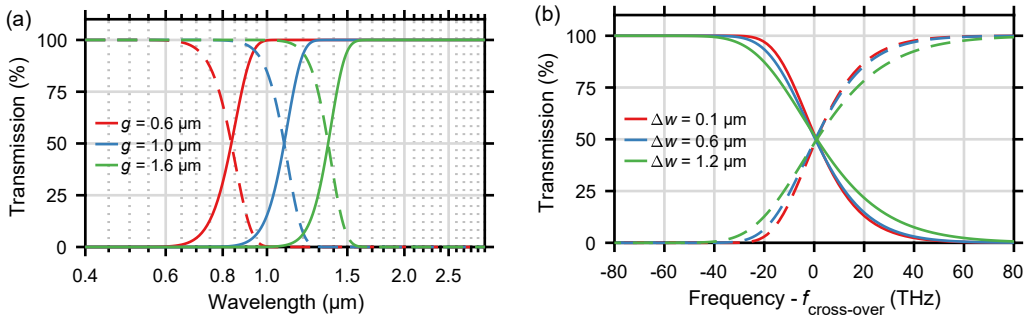

Figure 6.3: Calculated transmission of adiabatic couplers with $w_{\text{avg}} = 750$ nm and $L_{\text{coupler}} = 1000$ µm for (a) g variation and $\Delta w = 400$ nm and (b) Δw variation and $g = 1.6$ µm.

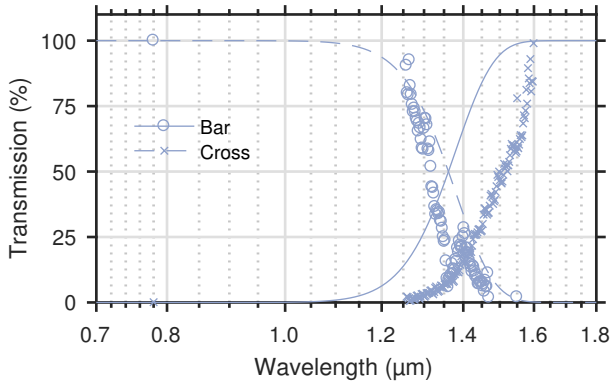

Figure 6.4: Transmission of an adiabatic coupler in the VIS and near-IR. The design parameters are $w_{\text{avg}} = 750$ nm, $\Delta w = 400$ nm, $g = 1.6$ µm, and $L_{\text{coupler}} = 1000$ µm.

There is good agreement between the experimental data and the model at 760 nm, but a lower transmission is observed in the near-IR relative to the model. A cross-over wavelength is evident at ∼1.40 µm, though the transmission is ∼19 % and the model predicts a cross-over wavelength of 1.38 µm. The cross-over bandwidth in the range of 1.20–1.45 µm also agrees well with the transmission model.

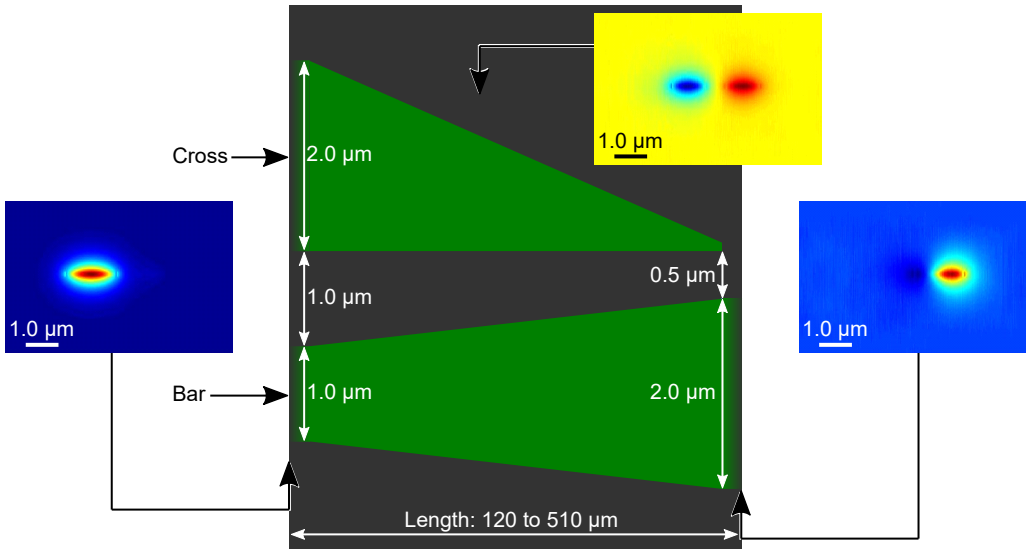

Figure 6.5: Diagram of ultra-broadband combiner with selected cross-sectional mode images shown along the length of the coupler assuming an input excitation of the fundamental mode of the "cross" port.

6.4 Ultra-broadband combiner

[3]The ultra-broadband combiner design is based on the adiabatic tapered mode coupler [20], but it also includes a tapered coupler gap to decrease the total coupler length. Analysis of the structure in Fig. 6.5, shows that there is a short wavelength spectrum and long wavelength spectrum of high TE fundamental mode transmission for the bar and cross inputs, respectively. The long wavelength cross input operates similarly to the previously demonstrated adiabatic coupling devices [20, 25], but the short wavelength bar input propagates light that does not have high enough coupling strength to be perturbed by the inversely tapering waveguide from the cross input. The TE fundamental mode transmission trend shows a cross-over wavelength where the transmission from each input is equivalent. Wavelengths longer than this cross-over wavelength have high transmission through the cross input and wavelengths shorter than the cross-over wavelength have high transmission through the bar input.

[3]Some of the analysis and figures in this section have been reproduced from [24] © 2015 OSA.

Previous examples of adiabatic couplers, as in [20, 25], approach the design with a theoretical model treating the waveguide propagation constant as slowly varying along the coupler length. For this ultra-broadband combiner, a theoretical modal would need to include propagation constants with a finite derivative with respect to the propagation distance since previously derived expressions do not agree with the performance of this coupler. Therefore, beam propagation method (BPM) simulation software was used to design this coupler and predict coupling efficiency trends versus coupler length and wavelength.

The primary design trade-off for such a broadband device is to choose waveguide geometries that guide the longest wavelengths without excessive loss and guide the shortest wavelengths while minimizing the number of guided modes. Considering that the application of this device involves an array of integrated diode lasers, any of the diode laser wavelengths will preferably lase into the fundamental TE mode. Therefore, even though the input waveguide may support TM modes and higher order TE modes, it is assumed that only the fundamental TE is excited. Similarly, other laser sources for mid-IR light, such as interband cascade lasers (ICLs) or quantum cascade lasers (QCLs), also lase in a fundamental mode, either TE or TM, and a fundamental TM mode can be rotated to a fundamental TE polarized mode [26]. The guided mode eigenvalues for 780 nm, 1550 nm, and 3600 nm wavelengths are shown in Fig. 6.6 for the cross and bar waveguides of the ultra-broadband combiner as a function of position along the couplers length.

The wavelengths sources used in the experiment are chosen to evaluate the three wavelength regimes of interest: high transmission of short wavelengths (very-near-IR), transmission near the cross-over wavelength (near-IR), and high transmission of long wavelengths (mid-IR). Along the length of the coupler, propagation constant β matching between coupling waveguides occurs for various modes as shown in Fig. 6.6. Strong

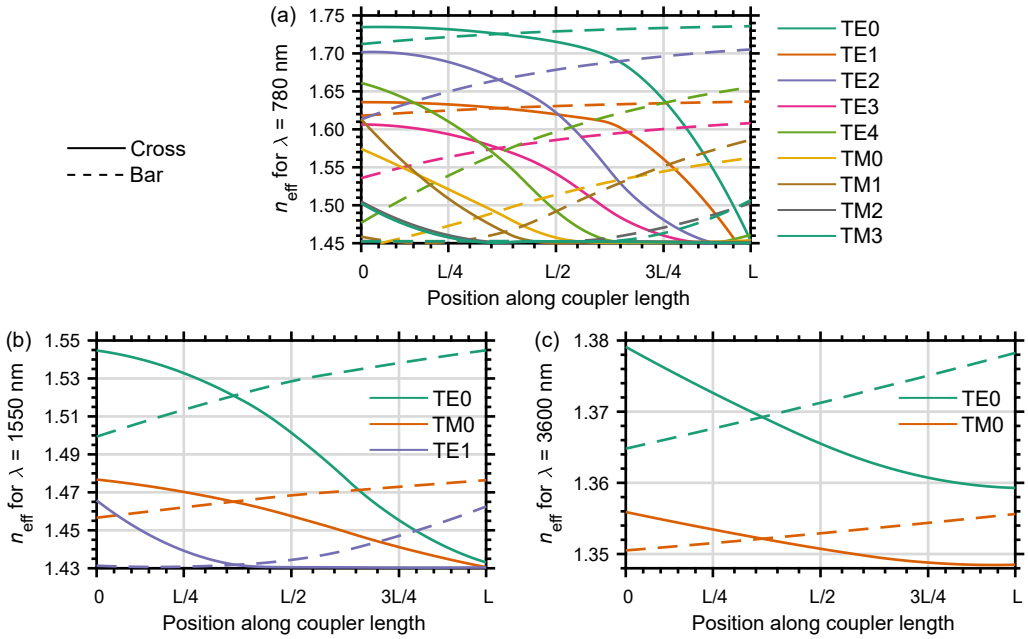

Figure 6.6: Effective indices in the bar (dashed lines) and cross (solid lines) waveguides of the ultra-broadband combiner as a function of position along the coupler length for (a) 780 nm, (b) 1550 nm, and (c) 3600 nm. Each position along the coupler length corresponds to the tapered bar and cross waveguide widths as shown in Fig. 6.5.

coupling between modes is achieved with β matching, high percentage modal overlap, and slowly varying β along the coupler length. For high fundamental mode transmission from each input the short wavelength bar input should not be perturbed along the coupler and the cross input should completely couple into the output waveguide. The β matching between the 780 nm fundamental modes in Fig. 6.6(a) occurs when the modal overlap is low so the overall coupling is low. For 1550 nm, the modal overlap is higher in the β matching region and some coupling occurs. The largest 3600 nm mode has a high mode overlap and high coupling occurs where there is β matching.

Since the coupler will have decreased fundamental mode transmission near the cross-over wavelength, this wavelength regime is not an ideal operating point. This work investigates the parameters that affect the cross-over wavelength to enable engineering of a particular cross-over wavelength by measuring transmission for various lengths of

the ultra-broadband combiner and three wavelength spectra in the near-IR: 1310 nm, 1430 nm, and 1550 nm.

To experimentally test the ultra-broadband combiner the fundamental TE mode must be excited for each input and wavelength. An input mode filter is designed in the fabricated devices with partially etched waveguides to minimize higher order TE mode excitation. Light is coupled into the cross and bar inputs via partially etched waveguides at the facets, which are adiabatically tapered to fully etched waveguides of 2 µm and 1 µm widths for the cross and bar inputs, respectively, to the ultra-broadband coupler as shown in Fig. 6.7. At the labeled region "I", the bar and cross inputs at the facet are initially 0.4 µm and 2.0 µm wide partially etched waveguides, respectively, in order to minimize higher order mode excitation. Next, at region "II", the buried rib waveguide adiabatically tapers to a buried channel waveguide as in Fig. 6.8. At region "III" the 0.4 µm wide waveguide is then laterally tapered to a 1.0 µm wide waveguide for the input to the ultra-broadband combiner. The cross waveguide is already the appropriate 2.0 µm width after the bi-level taper in region "II" so there is not another lateral taper for this waveguide.

The guided mode eigenvalues in region "I" of Fig. 6.7 for 780 nm, 1550 nm, and 3600 nm wavelengths are shown in Table 6.1. TM mode excitation is avoided by polarization filtering at the input. Since the 1550 nm cross input has a TE1 mode, it is incorporated in the BPM simulations. All other waveguides do not guide higher order TE modes for these wavelengths.

For the bi-level taper in region "II" of Fig. 6.7, the TE mode transmission is also shown in Table 6.1. The TM mode excitation is not shown since the TE modes can be efficiently excited with high polarization extinction ratio, which is discussed further in Section 3. The 3600 nm taper transmission is not shown since this input taper is removed for 3600 nm transmission simulations and measurements since it is not necessary to isolate

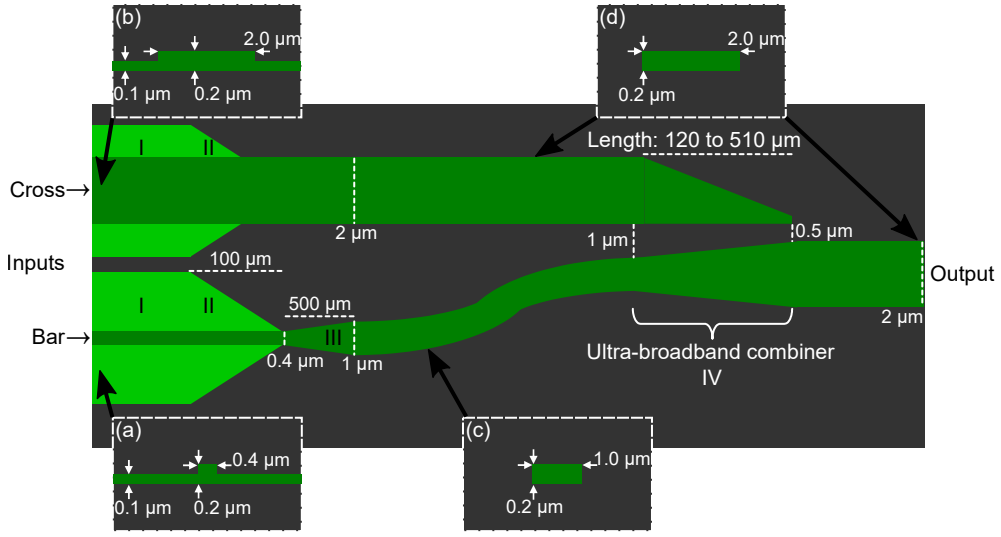

Figure 6.7: Ultra-broadband combiner and input tapered waveguide schematic. Green colors represent1 100 nm (light) and 200 nm (dark)tall Si_3N_4.

Table 6.1: Bi-level taper transmission for applicable wavelengths of each input waveguide, simulated with FIMMPROP [23].

Input mode	Wavelength (nm)	TE0 (%)	TM0 (%)	TE1 (%)
Bar TE0	780	100.0	0.0	-
Bar TE0	1550	94.1	0.0	-
Cross TE0	1550	100.0	0.0	0.0
Cross TE1	1550	0.0	91.4	8.6
Cross TE0	3600	100.0	0.0	-

the fundamental TE mode and only adds more loss. The taper in region "III" of Fig. 6.7 is completely adiabatic and simulations show no loss for each mode present in the bar waveguide.

The ultra-broadband combiner, shown in region "IV" of Fig. 6.7, linearly tapers each waveguide along the length of the coupler. The width of the cross input tapers from 2 µm to 100 nm, which is the narrowest achievable taper width with the deep-UV lithography process used here, and the width of the bar input tapers from 1 µm to 2 µm. The coupler gap is tapered from 1 µm to 0.5 µm.

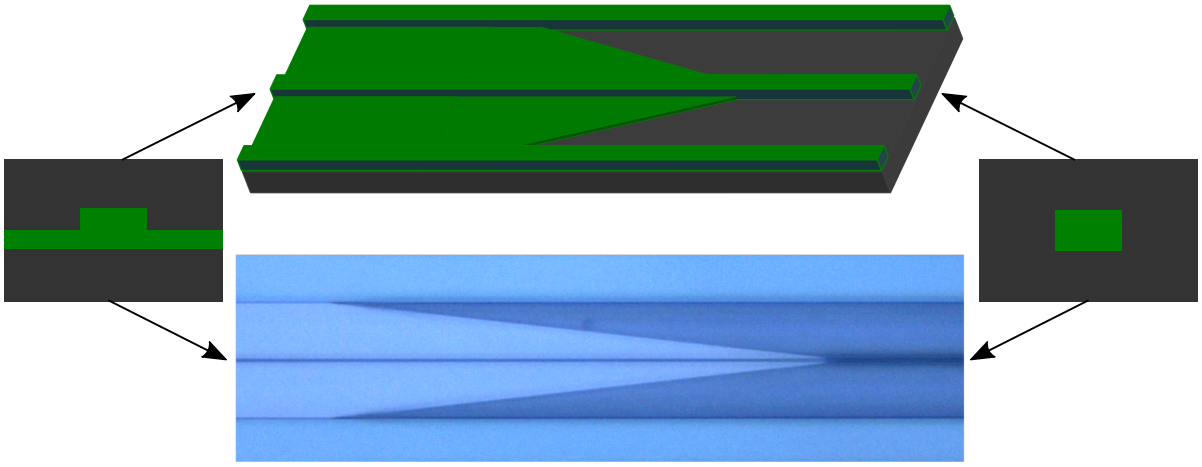

Figure 6.8: Bi-level taper schematic and micrograph.

In Fig. 6.9 simulation trends are shown for fundamental mode transmission as a function of wavelength and coupler length. A 3D semi-vectorial BPM simulation is configured for each wavelength. The simulation window size varies as a function of wavelength from 14.5 µm to 70 µm in the horizontal direction and 4.5 µm to 16 µm in the vertical direction. Similarly, the step size in each transverse direction increases from 0.005 µm to 0.1 µm and in the propagation direction from 0.01 µm to 0.2 µm. The smaller window and step sizes correspond to the shortest wavelength of 350 nm and increase with wavelength to the largest window and step size for the longest wavelength of 6500 nm. An example BPM simulation is shown in Fig. 6.10 for TE and TM modes.

The cross-over wavelength trend is investigated for various coupler lengths. As the coupler length decreases the cross-over wavelength increases. A variety of other factors, such as coupler gap, taper rate, material indices, waveguide geometries, and modal excitation, also affect the cross-over wavelength, but these are not varied. The coupler length is most easily controllable parameter that can provide the widest range of cross-over wavelength tuning. To achieve cross-over wavelengths outside of this tuning range,

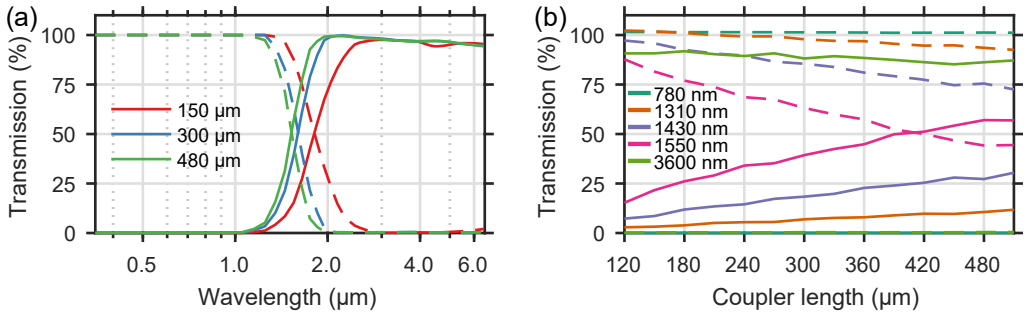

Figure 6.9: Simulations of fundamental mode transmission (a) wavelength dependence and (b) coupler length dependence.

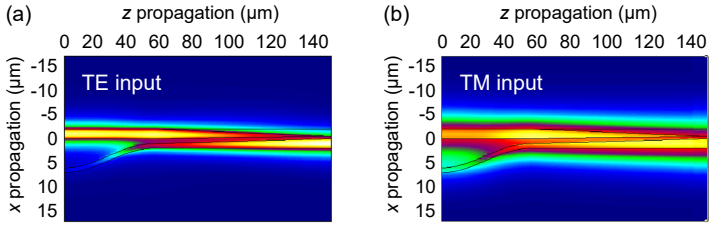

Figure 6.10: Example simulation of cross-port propagation for (a) TE and (b) TM modes of 4.5-µm input light. Black boxes indicate 3-axes piezo-controlled translation stages used for alignment.

the coupler gap and taper rate can also be easily tuned, but this is not investigated in this work.

Mode excitation and measurement is a critical issue for (very)-near-IR wavelengths since multiple TE modes exist in the bar waveguide. In order to simulate and measure fundamental mode transmission the performance of the higher order TE mode must be characterized so the measurement setup can be designed to represent the fundamental mode transmission. The TE0 and TE1 mode transmission is shown in Fig. 6.11 for an ultra-broadband combiner with a 300 µm coupler length. Both TE0 and TE1 modes are separately launched and each mode overlap integral with both TE0 and TE1 modes is measured for the transmission of the combiner.

These devices are fabricated on Si substrate wafers with 2 µm of thermally grown SiO_2. A 200 nm layer of low-pressure chemical vapor deposition (LPCVD) stoichiometric

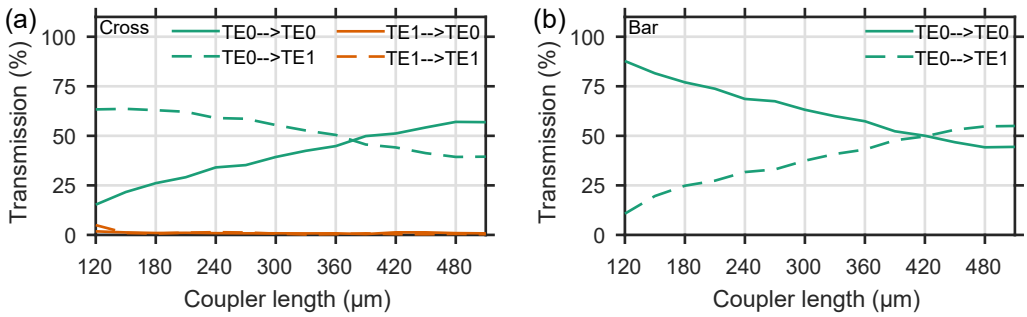

Figure 6.11: Simulation for the (a) cross and (b) bar ports at 1550 nm launching TE0 and TE1 modes and measuring transmission to the TE0 and TE1 modes at the output.

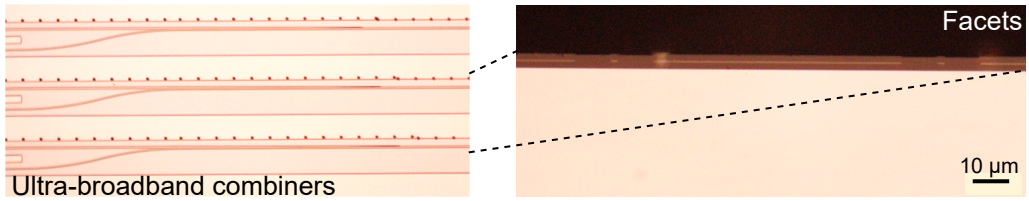

Figure 6.12: Micrographs picture of fabricated ultra-broadband combiners top view and facet view.

Si_3N_4 is deposited on top of the SiO_2 and deep-UV lithography with carbon tetrafluoride and oxygen inductively coupled plasma (ICP) etching defines the waveguides. A second lithography and etch step defines the fully etched Si_3N_4 regions shown in Fig. 6.7. Finally, a 2 μm plasma-enhanced chemical vapor deposition (PECVD) SiO_2 layer forms the top cladding layer and the wafer is annealed at 1050 °C for 8 hours to improve SiO_2 index uniformity. An optical photograph in Fig. 6.12 shows devices and polished facets of 2 out of the 1680 devices processed on one 4-inch wafer. The device yield was 100 % for the 90 measured devices. Etched channels in the cladding SiO_2, visible along the side of the coupler in Fig. 6.12, are unused in this work, but allow for future investigation of an undercut substrate to reduce substrate leakage loss of the mid-IR band wavelengths.

Insertion losses were measured in three different wavelength bands to demonstrate ultra-broadband operation. A tunable laser at 780 nm is used as the very-near-IR source. An incoherent broadband light source with peaks at 1310 nm, 1430 nm, and 1550 nm is

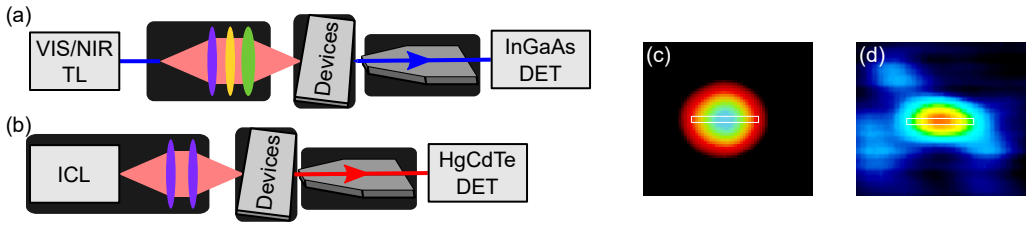

Figure 6.13: Experimental setup for (a) near-IR and (b) mid-IR transmission measurements. Output mode images shown for (c) 1550 nm and (d) 3600 nm wavelengths.

used as the near-IR source. An interband cascade laser (ICL) at 3600 nm is used at the mid-IR source. Figure 6.13 shows the measurement setup schematics for the (very)-near-IR measurements and the mid-IR measurements. Both setups free space couple light from a source to the input waveguide. High TE polarized input with polarization extinction ratio >45 dB is ensured for the (very)-near-IR setup in Fig. 6.13(a) with a dichroic film polarizer. The mid-IR setup in Fig. 6.13(b) has a high polarization extinction ratio of >20 dB due to the lasing polarization in the ICL. The output waveguide couples light into a single mode fiber and the output of the fiber is measured by a photodetector. Output modes were imaged on infrared cameras to obtain the near field modes in Fig. 6.13(c–d).

For the mid-IR transmission measurements, the devices were diced and polished to remove regions I, II, and III (see Fig. 6.7). However, not shown in Fig. 6.7) is a large s-bend for both waveguides that was put in the mask layout to decrease detection from substrate coupling. This large bend was removed in this step because there was a high bending loss for the mid-IR wavelengths.

The fundamental mode transmission is measured for coupler lengths from 120 µm to 510 µm in steps of the 30 µm. For very-near-IR, high transmission near 100 % is shown invariant of coupler length in Fig. 6.14(a), which matches the overlaid simulation trend. The transmission data is normalized to the transmission from a device with the same input and output waveguides as the ultra-broadband combiner, but with only a straight

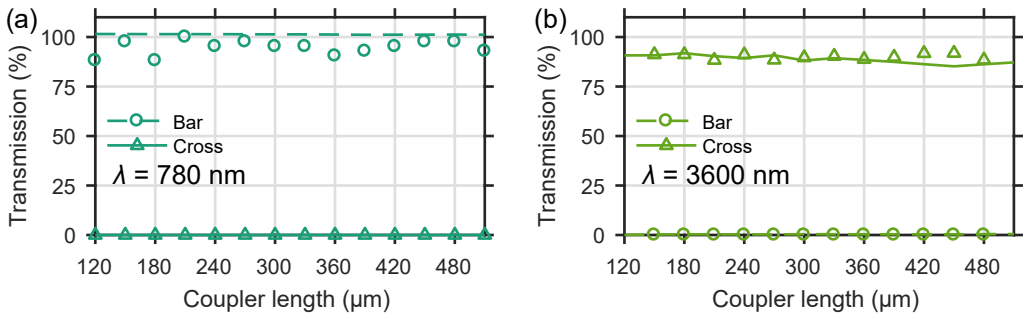

Figure 6.14: Transmission dependence on coupler length for (a) 780 nm and (b) 3600 nm wavelengths input including overlaid simulations for each.

or tapered waveguide in between. Only the device insertion loss is presented since the input and output coupling losses, material absorption losses, waveguide scattering loss, and waveguide bend losses are all normalized.

For the mid-IR, the normalized transmission dependence on coupler length is shown in Fig. 6.14(b), where the simulation data is overlaid. The high transmission invariant of coupler length agrees with the simulation data. By measuring series of identical devices, an RMS error is calculated as 5 % for the normalized data in both very-near-IR and mid-IR measurements.

Fundamental mode transmission data for the 1310 nm, 1430 nm, and 1550 nm bands show the complete trend of high to low and low to high transmission through the cross-over wavelength from the bar and cross inputs, respectively. The 1310 nm measurements in Fig. 6.15(a) show high transmission from the bar input, decreasing as coupler length increases, and low transmission from the cross input, increasing as coupler length increases. This indicates that 1310 nm is shorter than the cross-over wavelength.

Measurements in Fig. 6.15(b) show equivalent transmission at 300 μm, indicating the cross-over wavelength is near 1430 nm. Fundamental mode transmission in Fig. 6.15(c) shows a trend of increasing cross transmission with increasing coupler length and decreasing bar transmission with increasing coupler length suggesting the cross-over

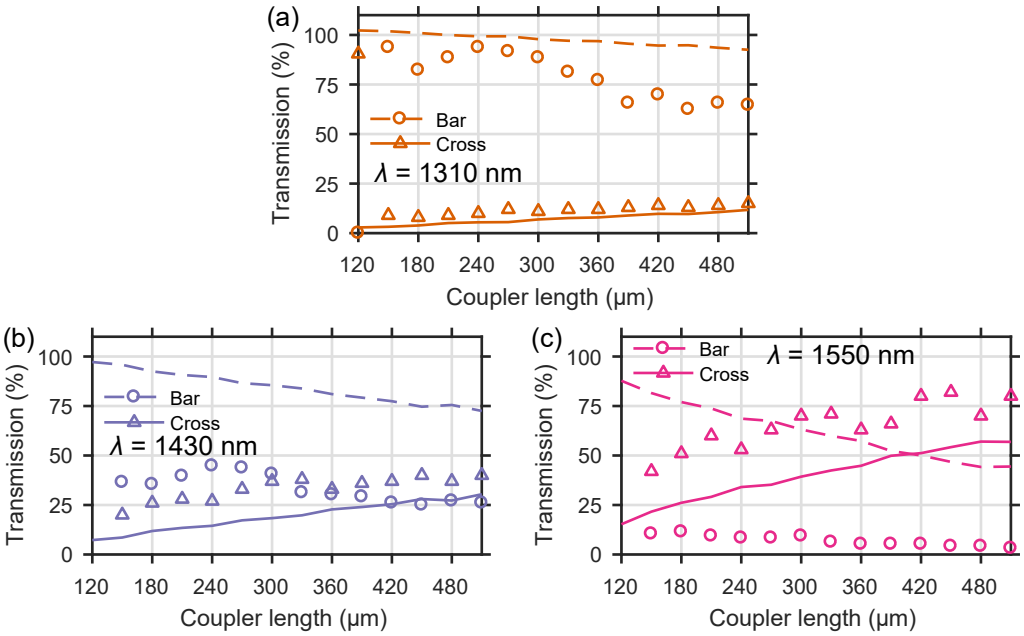

Figure 6.15: Transmission dependence on coupler length for (a) 1310 nm, (b) 1430 nm, and (c) 1550 nm wavelengths input including overlaid simulations for each.

wavelength is shorter than 1550 nm. Although data in Fig. 6.15 does not match corresponding simulations, the trends indicate the dependence of cross-over wavelength to coupler length and a cross-over wavelength shift.

By combining transmission data from each spectral band measurement together, the transmission spectrum of the ultra-broadband coupler is shown in Fig. 6.16 for the bar and cross input excitations. The very-near-IR and mid-IR data points show high transmission as predicted and the cross-over wavelength is about 1430 nm, as shown from the near-IR measurements. As simulations suggest, the very-near-IR cross transmission and the mid-IR bar transmission are low and these data points are both lower than the measurement dynamic range, which is 35 dB for the near-IR setup and 30 dB for the mid-IR setup.

Although the measured transmission above and below the cross-over wavelength corresponds well with the BPM simulation, Fig. 6.16 shows the measured cross-over wavelength is blue-shifted relative to simulations. Also, the slope of transmission versus

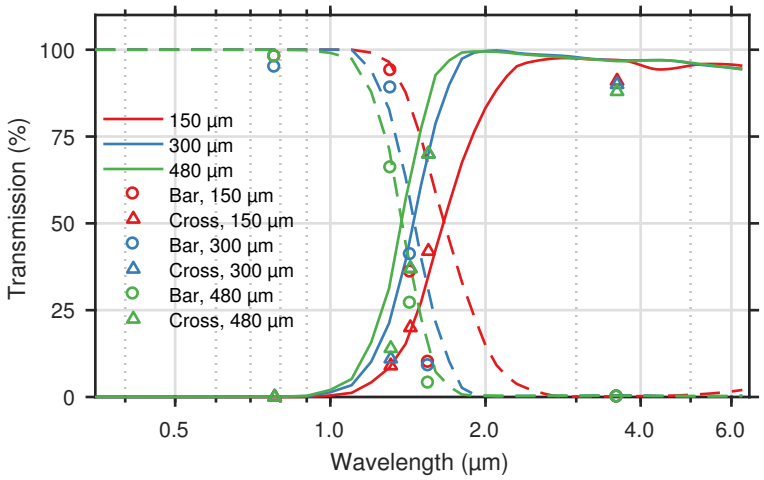

Figure 6.16: Transmission spectra for 150 µm, 300 µm, and 480 µm coupler lengths through the bar and cross ports with simulated transmissions.

wavelength is steeper near the cross-over wavelength for both cross and bar inputs. At the cross-over wavelength in Fig. 6.15, it is evident that the sum of the measured cross and bar fundamental mode transmission is less than the sum of the simulated cross and bar fundamental mode transmission. Therefore, either more light is coupled into the higher order mode or the light is scattering at this wavelength. A number of fabrication related issues could have affected these discrepancies including the formation of air gaps and strain from PECVD top cladding deposition, affecting the material indices, which were not accounted for in this simulation. Air gaps did develop from the PECVD top cladding deposition at the waveguide facets, but air gaps were no longer visible in SEM images after the anneal. Further analysis to dice and polish the devices will reveal if air gaps still exist along the coupler.

Another factor that affects the accuracy of the measurement data is how much the measurement data represents the fundamental mode transmission. Especially in the cross-over wavelength regime, the higher order TE mode becomes excited in the coupler and can skew the measurement data if the TE1 mode has a high overlap integral with the output coupling, which can be increased if the fiber is not aligned to the geometric center

of the waveguide. An incoherent broadband source is used for the near-IR measurement and alignment to the waveguide center is ensured by monitoring the output spectrum. If the normalized spectrum flat, then the fiber is aligned to the waveguide center since higher order modes are least excited and mode beating is minimized. Since the input and output coupling are roughly Gaussian shapes with $1/e^2$ width of 2 µm, the overlap integral with the TE0 and TE1 modes is calculated to be 94 % and 6 %, respectively, for a fiber aligned to the center of the waveguide. Using the mode transmission results incorporating the TE0 and TE1 modes from Table 6.1 and Fig. 6.11, the transmission for a 300 µm long coupler is predicted to be 58.8 % including normalization compared to the fundamental mode simulated transmission of 63.2 % for the bar input. For the cross input the normalized transmission including both modes is 42.8 % compared to the fundamental mode simulated transmission of 39.3 %. These predicted values are only 4.4 % point higher and 3.5 % point lower, respectively. Although this is a relatively small error in transmission, this would result in a blue-shift of the cross-over wavelength relative to the fundamental mode simulations shown in Fig. 6.16. Therefore, the higher order TE mode excitation does contribute to the cross-over wavelength blue-shift by approximately 15 nm. This shift is small compared to the measured shift of about 160 nm so this error is not the only factor contributing to the cross-over wavelength shift.

Since higher order modal excitation does not contribute all of the cross-over wavelength error, it is expected that air gaps and strain have significantly altered the material indices to cause this discrepancy. Formation of air gaps, schematized in Fig. 6.17(a), are found in the cross-sectional SEM of the waveguide, in Fig. 6.17(b). Both air gaps and altered indices could contribute to higher order mode coupling, explaining the decrease in fundamental mode transmission at the cross-over wavelength. Since strain affects are not likely isotropic, further three-dimensional analysis of strain in this design

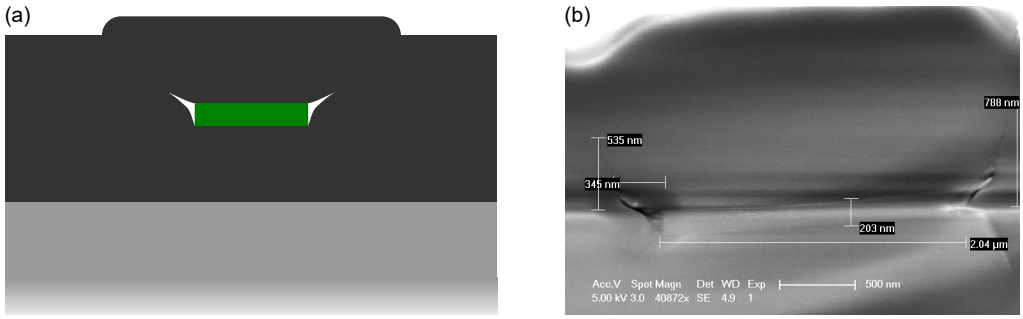

Figure 6.17: (a) Schematic and (b) SEM of air-gap "bunny ear" formation from sputtered SiO_2 at the corners of the waveguide.

is necessary to characterize the possible effects of strain on the cross-over wavelength shift.

For wavelengths longer than ∼3.0 µm, substrate leakage becomes the dominating effect in the propagation loss for this waveguide design. One solution is to increase the lower cladding thickness. If lasers are integrated on this waveguide platform, then an increased lower cladding thickness would degrade the laser performance due to increase thermal resistance to the substrate and heat-sink. Another solution is to undercut the Si substrate in selective areas beneath the waveguide. The added benefit of this solution is the decreased confinement of the long-wavelength photons in the SiO_2, which has high absorption loss for wavelengths longer than ∼3.4 µm. This can be achieved by etching holes through the $SiO_2/Si_3N_4/SiO_2$ layer stack to expose the Si substrate. Using xenon difluoride (XeF_2), the Si can be isotropically etched, as shown in Fig. 6.18(a). An unsuccessful etch is also shown in Fig. 6.18(b) to highlight the catastrophic damage that can occur if the density of hole is too high or if the etch depth is too long.

6.5 Summary and conclusion

A feasible design for an integrated multi-octave spectral beam combiner design has been presented including a novel ultra-broadband combiner. High transmission greater

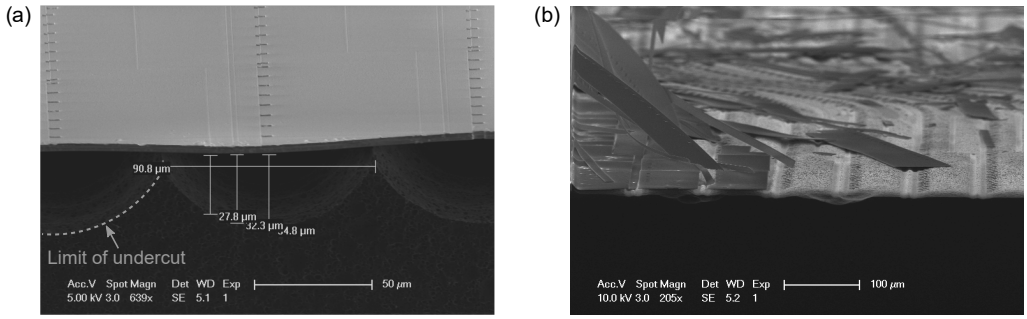

Figure 6.18: SEMs of the XeF_2 undercut of the Si substrate: (a) successful undercut and (b) failure do to excessive undercut at the facets.

than 90 % for 780 nm and 3600 nm wavelengths has been demonstrated, and the cross-over wavelength is found in the near-IR, although it was spectrally shifted relative to the simulation results. This technology uses an ultra-broadband platform compatible with previously demonstrated spectral combining technologies and lasers bonded to Si. This demonstration culminates the three passive stages of spectral beam combining, envisioned in the ultra-broadband multi-spectral laser architecture described in Chapter 2.

References

[1] B. G. Lee, J. Kansky, A. K. Goyal, C. Pflügl, L. Diehl, M. A. Belkin, A. Sanchez, and F. A. Capasso, "Beam combining of quantum cascade laser arrays," Opt. Express **17**, 16216–16224 (2009).

[2] A. A. Kosterev and F. K. Tittel, "Chemical sensors based on quantum cascade lasers," IEEE J. Quantum Electron. **38**, 582–591 (2002).

[3] I. H. White, "A multichannel grating cavity laser for wavelength division multiplexing applications," J. Lightw. Technol. **9**, 893–899 (1991).

[4] T. Y. Fan, "Laser beam combining for high-power, high-radiance sources," IEEE J. Sel. Topics Quantum Electron. **11**, 567–577 (2005).

[5] F. Silva, D. R. Austin, A. Thai, M. Baudisch, M. Hemmer, D. Faccio, A. Couairon, and J. Biegert, "Multi-octave supercontinuum generation from mid-infrared filamentation in a bulk crystal," Nat. Commun. **3**, 807 (2012).

[6] E. J. Bochove, "Theory of spectral beam combining of fiber lasers," IEEE J. Quantum Electron. **38**, 432–445 (2002).

[7] V. Daneu, A. Sanchez, T. Y. Fan, H. K. Choi, G. W. Turner, and C. C. Cook, "Spectral beam combining of a broad-stripe diode laser array in an external cavity," Opt. Lett. **25**, 405–407 (2000).

[8] C. D. Stacey, C. Stace, and R. G. Clarke, "Ultrabroadband spectral beam combiner spanning over three octaves," Appl. Opt. **52**, 7200–7205 (2013).

[9] H.-H. Chang, Y.-h. Kuo, R. Jones, A. Barkai, and J. E. Bowers, "Integrated hybrid silicon triplexer," Opt. Express **18**, 23891–23899 (2010).

[10] J. T. Bovington, M. J. R. Heck, and J. E. Bowers, "Heterogeneous lasers and coupling to Si_3N_4 near 1060 nm," Opt. Lett. **39**, 6017–6020 (2014).

[11] A. W. Fang, H. Park, O. Cohen, R. Jones, M. J. Paniccia, and J. E. Bowers, "Electrically pumped hybrid AlGaInAs-silicon evanescent laser," Opt. Express **14**, 9203–9210 (2006).

[12] A. Spott, M. Davenport, J. Peters, J. Bovington, M. J. R. Heck, E. J. Stanton, I. Vurgaftman, J. Meyer, and J. Bowers, "Heterogeneously integrated 2.0 µm CW hybrid silicon lasers at room temperature," Opt. Lett. **40**, 1480–1483 (2015).

[13] M. J. Heck, J. F. Bauters, M. L. Davenport, J. K. Doylend, S. Jain, G. Kurczveil, S. Srinivasan, Y. Tang, and J. E. Bowers, "Hybrid silicon photonic integrated circuit technology," IEEE J. Sel. Topics Quantum Electron. **19**, 6100117 (2013).

[14] T. Komljenovic, M. Davenport, J. Hulme, A. Y. Liu, C. T. Santis, A. Spott, S. Srinivasan, E. J. Stanton, C. Zhang, and J. E. Bowers, "Heterogeneous silicon photonic integrated circuits," J. Lightw. Technol. **34**, 20–35 (2016).

[15] J. S. Cook, "Tapered velocity couplers," Bell Labs Tech. J. **34**, 807–822 (1955).

[16] A. G. Fox, "Wave coupling by warped normal modes," Bell Labs Tech. Jo. **34**, 823–852 (1955).

[17] W. H. Louisell, "Analysis of the single tapered mode coupler," Bell Labs Tech. J. **34**, 853–870 (1955).

[18] E. A. J. Marcatili, "Dielectric rectangular waveguide and directional coupler for integrated optics," Bell Labs Techn. J. **48**, 2071–2102 (1969).

[19] M. G. F. Wilson and G. A. Teh, "Improved tolerance in optical directional couplers," Electron. Lett. **9**, 453–455 (1973).

[20] A. F. Milton and W. K. Burns, "Tapered velocity couplers for integrated optics: design," Appl. Opt. **14**, 1207–1212 (1975).

[21] R. B. Smith, "Coupling efficiency of the tapered coupler," Electron. Lett. **11**, 204–206 (1975).

[22] A. Yariv, "Coupled-mode theory for guided-wave optics," IEEE J. Quantum Electron. **9**, 919–933 (1973).

[23] www.photond.com.

[24] E. J. Stanton, M. J. Heck, J. Bovington, A. Spott, and J. E. Bowers, "Multi-octave spectral beam combiner on ultra-broadband photonic integrated circuit platform," Opt. Express **23**, 11272–11283 (2015).

[25] X. Sun, H.-C. Liu, and A. Yariv, "Adiabaticity criterion and the shortest adiabatic mode transformer in a coupled-waveguide system," Opt. Lett. **34**, 280–282 (2009).

[26] Z. Wang and D. Dai, "Ultrasmall Si-nanowire-based polarization rotator," J. Opt. Soc. Am. B **25**, 747–753 (2008).

Chapter 7

Multi-spectral quantum cascade lasers

7.1 Introduction

QCLs are the highest power semiconductor lasers in the mid-IR. Optical gain is created in a fundamentally different way than in typical diode lasers. Rather than electron-hole pairs recombining across the band-gap (interband transitions), photons are generated from intersubband transitions. A QCL active region consists of a unipolar superlattice of semiconductor materials. The emitted photon energies are determined only by the thickness of the epitaxially grown layers. Diode laser emission wavelength relies on the inherent bandgap, which can only be tuned in a limited range due by changing the material composition or the lattice strain. QCLs can be designed to emit light in the mid-IR, as short as ∼2.6 µm [1], to the long-wave-IR and the THz regime, around ∼250 µm [2]. Typically, many repetitions of the same gain material are incorporated in the QCL active region, hence the "cascade" part of the name. An operating bias voltage in the range of 15–20 V is common, and this varies depending on

the number of gain stages [3]. CW output power up to 5.1 W with wall-plug efficiency of 21 % has been reported for devices emitting at 4.9 µm [4].

Multi-spectral QCLs provide a means for molecular fingerprinting by absorption spectroscopy. Beam combining of QCLs has been an important topic of research to support this application, though state-of-the-art devices use a free-space multiplexer [5, 6]. The only integrated demonstration of beam combining QCLs uses an inherently high-loss y-junction duplexer tree [7].

Recent development of QCLs integrated on a Si substrates allows for more complex photonic circuits in the mid-IR [8, 9]. This work aims to reproduce this initial demonstration and integrate arrays of these laser with AWGs to spectrally combine them on a single chip. Minor changes are made to the fabrication process and to the laser design in efforts to improve fabrication yield, thermal dissipation, and output power. The largest modification is that the laser epitaxial material (EPI) is supplied from a different source, thus the active region, claddings, and contact layers are different. The previous demonstrations of QCLs heterogeneously integrated on Si substrates used the SONOI platform [8, 9]. Another recent demonstration integrates QCLs on a Si-on-sapphire platform via transfer-printing [10]. Literature reports, especially within the last decade, have indicated that Si_3N_4 has lower absorption loss than SiO_2 in the range of 2.5–5.0 µm. This motivated the SONOI platform, but further literature search shows that this may not be true. Since high-quality SOI is commercially available, while SONOI is not, there is a large advantage to switching to this waveguide platform. Also, SOI has better thermal conduction to the Si substrate since the lower cladding is thinner. For these reasons, this experiment uses SOI.

Spectral beam combining has been proposed to create an on-chip ultra-broadband multi-spectra and high-brightness source [11, 12]. This mid-IR demonstration is part of the more complex multi-band system and its waveguide platform is suitable for

bonding other EPI to combine a broader wavelength range. Previous AWGs have been demonstrated in the mid-IR, including a Ge waveguide AWG near 5 µm [13] and an SOI AWG near 3.8 µm [14]. The AWG in this design is unique because it the longest wavelength AWG on SOI, at 4.7 µm. Recent revelations indicate that the transparency range of SOI, which is limited by the SiO_2 absorption, can be extended by increasing the Si thickness compared to conventional designs [15].

This chapter describes the first fully-integrated multi-spectral QCL demonstration. An array of QCLs emits light near 4.7 µm wavelength and outputs are coupled to an on-chip multiplexer with the SOI waveguide platform. Low-loss spectral beam combining allows for brightness scaling by coupling TM light from the QCLs to the lowest order TM mode of a single output waveguide. The laser design is separated from the output facet waveguide design, which allows for the output mode to be independently tailored for a low M^2 value. This device is expected to enable compact gas detection and infrared countermeasure systems.

7.2 Design

The QCL EPI is grown on an indium phosphide (InP) substrate with metal-organic chemical vapor deposition (MOCVD) by Thorlabs Quantum Electronics (TQE). Table 7.1 shows the material layers of this wafer and of the SOI wafer used for bonding. There are ∼30 gain stages in the QCL active region. This EPI is very similar to the EPI used in the first QCL on SONOI demonstration. The largest variation is that the bottom cladding and contact layers are ∼50 nm thicker in this EPI.

Table 7.1: Thickness of material layers.

Layer	Material	Thickness (nm)	Doping (cm^{-3})
Substrate	InP	$\sim 360 \times 10^3$	–
Etch stop	$In_{0.53}Ga_{0.47}As$	50	–
Top contact	n-InP	1700	5×10^{18}
Top cladding	n-InP	50	5×10^{17}
Top cladding	n-InP	50	1×10^{17}
Top cladding	n-InP	2400	2×10^{16}
Active core	n-QC structure	1660	variable
Bottom cladding	n-InP	20	2×10^{16}
Bottom cladding	n-InP	35	1×10^{17}
Bottom cladding	n-InP	58	5×10^{17}
Bottom contact	n-InP	230	1×10^{18}
Bonding SL	n-InP	9	1×10^{18}
Bonding SL	n-InGaAs	9	1×10^{18}
Bonding SL	n-InP	9	1×10^{18}
Bonding SL	n-InGaAs	9	1×10^{18}
Bonding layer	n-InP	12	1×10^{18}
Capping layer	n-$In_{0.53}Ga_{0.47}As$	230	1×10^{18}
Waveguide core	Si	1500	–
Bottom cladding	SiO_2	1000	–
Substrate	Si	$\sim 720 \times 10^3$	–

7.2.1 Laser mirrors

Lasers are designed with a 4-mm gain length and two types of mirrors: a distributed feedback (DFB) and a distributed Bragg grating (DBR). The DFB lasers have a quarter-wavelength ($\lambda/4$) phase shift section at the center of the gain region to promote a single longitudinal lasing mode. The DBR lasers have a 1.0-mm long grating near the back side of the laser and a 0.5-mm long grating near the front side of the laser, both underneath the III–V mesa. Grating periods for the DFB and DBR arrays of eight lasers are listed in Table 7.2.

The gratings are defined by etching a periodic rectangular pattern into the top of the Si waveguide. The length for the etched sections is L_1 and for the un-etched sections is L_2. These lengths are designed as $L_{1,2} = \lambda_0/(4n_{\text{eff};1,2})$. Transmission matrices are used

Table 7.2: Designed and measured channel wavelengths (λ).

Ch. #	Period (nm)	Designed λ (nm)	Measured λ (nm)
1	756.13	4641	4560
2	752.94	4661	4580
3	749.75	4681	4600
4	746.56	4702	4620
5	743.37	4722	4640
6	740.18	4742	4660
7	736.99	4762	4680
8	733.80	4782	4700

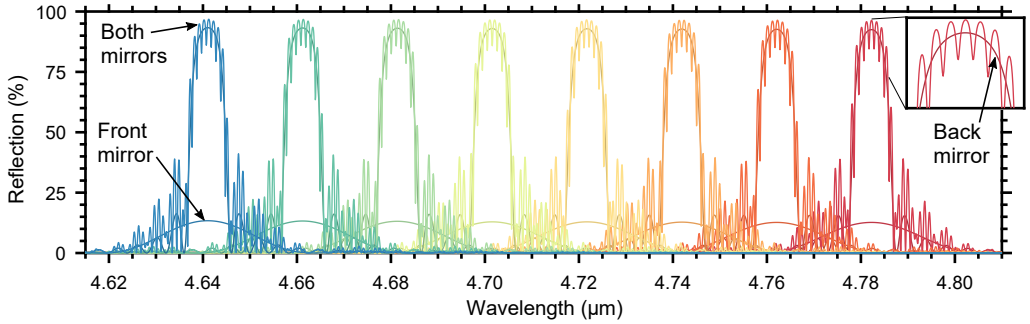

Figure 7.1: Reflection of the DBR design at transparency for the front mirror, back mirror, and both mirrors including a cavity of ∼3 mm.

to calculate the reflection and transmission of these gratings to design the mirrors [16]. The reflections for the DBR mirrors at transparency are plotted in Fig. 7.1. About six longitudinal modes exist in the 3-dB bandwidth of each mirror set. Power reflections for the front mirrors are ∼12 % and for the back mirrors are ∼93 %. Reflections for the DFB lasers at transparency are plotted in Fig. 7.2. A narrow lasing mode is evident in the center of each stop-band, with a FWHM of ∼8.0 MHz.

The grating etched in the Si waveguide produces a strong grating with a κL in the range of 9.8–10.1, as calculated with the approximate analysis using the plane-wave assumption. However, previous experiments with near-IR grating-based lasers indicate that the grating strength, κL, is often much less than values calculated from the approximate plane-wave method.

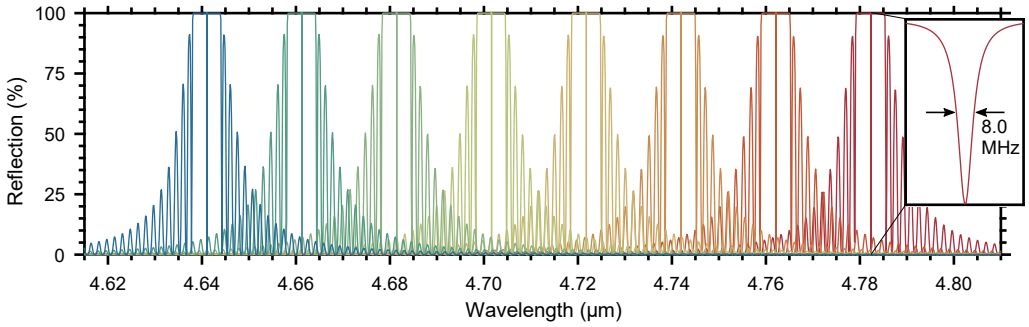

Figure 7.2: Reflection of the 4-mm long, $\lambda/4$-shifted DFB at transparency.

7.2.2 Tapers

Four different taper designs are schematized in Fig. 7.3. On each chip, there are four multi-spectral lasers (labeled A, B, C, and D), each corresponding to these different taper designs. Although simulations do not predict a large reflection from these tapers, experiments from the QCL on SONOI concluded that only a small fraction of the generated laser light was transferred to the passive Si waveguide[1]. The tapers design in Fig. 7.3(a) (design A) is exactly the same as the QCL on SONOI design [8, 9] and is used here as an experimental control[2]. Designs in Fig. 7.3(b–d) simultaneously vary the III–V mesa and Si waveguides widths to attempt at creating an adiabatic mode transition by following a contour of quasi-constant effective index [17]. Design B uses two regions of linear tapers. Designs C and D both use a single region, but design D is twice the length of design C.

The effective indices of the hybrid III–V modes are simulated for varying III–V width and varying Si width in Fig. 7.4(a) for the EPI used in the previous work [8, 9] and in Fig. 7.4(b) for the present work. These simulations reveal that the effective index trends

[1]This fraction varied between devices, but typically is near 10 % [9].

[2]Note that this control is not exactly the same design as the previous experiment because of the different EPI and the use of SOI rather than SONOI.

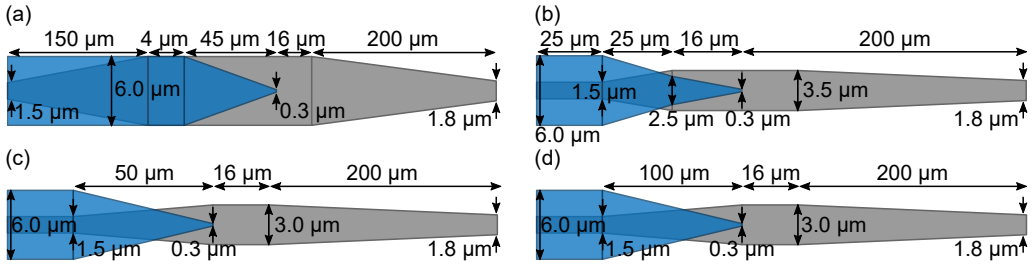

Figure 7.3: Taper designs (a–d) correspond to labels A–D.

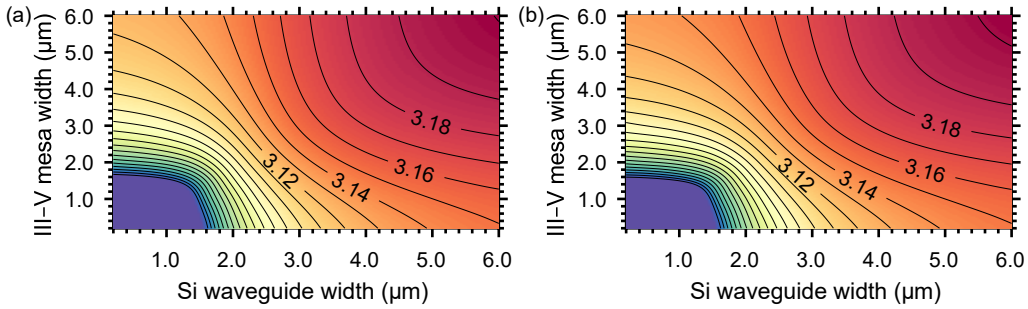

Figure 7.4: Map of effective refractive indices for the hybrid III–V/Si mode for the EPI (a) used in [8, 9] and (b) from TQE described in Table 7.1.

are nearly the same between EPIs. When comparing exact geometries, *e.g.*, III–V width of 6.0 µm and Si width of 3.7 µm, the TQE hybrid mode has a slightly larger index.

7.2.3 Arrayed waveguide grating

This AWG is designed with the same methodology as in Section 4.2 and as demonstrated in previous works [18–20]. A model of the AWG transmission spectra are shown in Fig. 7.5 and calculated design parameters are listed in Table 7.3. In part, because of the long wavelength, a low-order grating of 10 is produced. A larger channel spacing would increase ΔL and reduce the AWG footprint, but the total bandwidth is limited by the laser EPI.

The AWG model predicts a total loss for the center channels of 1.07 dB, which is the sum of the side-order grating excitation of 0.63 dB, the arrayed waveguide aperture limitation of 0.09 dB, and propagation loss of 0.35 dB. Peak-transmission of the outer

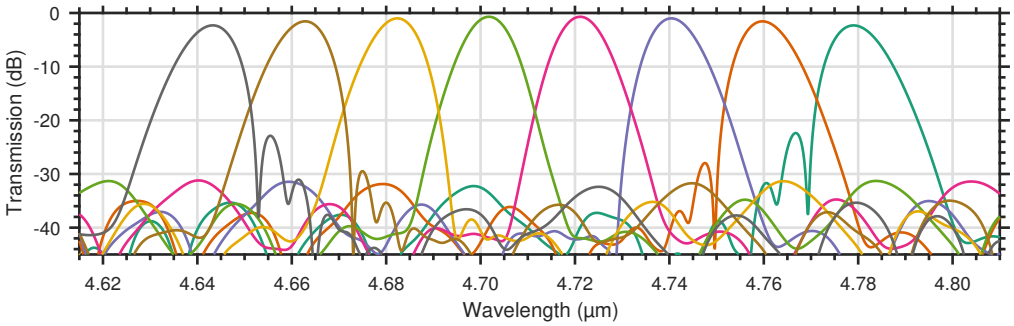

Figure 7.5: Calculated transmission spectra for AWG coupled to QCLs on SOI, with design parameters in Table 7.3.

Table 7.3: Design and layout dimensions for the 4.7-μm AWGs.

Number of channels	N_{ch}	8
Number of AWs	N_{AW}	73
Rowland radius	r	75.23 μm
AW length increment	ΔL	16.71 μm
AW width	w_{AW}	1.50 μm
AW width at FPR	$w_{\mathrm{AW\text{-}FPR}}$	1.60 μm
i/o waveguide width	w_{io}	1.80 μm
i/o waveguide width at FPR	$w_{\mathrm{io\text{-}FPR}}$	1.80 μm
AW pitch at FPR	$d_{\mathrm{c,AW}}$	1.90 μm
i/o waveguide pitch at FPR	$d_{\mathrm{c,io}}$	3.60 μm
Footprint area	S	∼3.68 mm^2

channels is 1.4-dB less than the center channels. The channel spacing is ∼20.23 nm (268.8 GHz) and the FSR is 342.8 nm.

7.3 Fabrication and methods

Schematics of each step in the fabrication process are shown in Fig. 7.6. SOI wafers, 200-mm in diameter, have a 1.0-μm thick lower cladding of SiO_2 and a 1.5-μm thick Si waveguide core. Gratings and alignment marks are etched in the Si with a standard deep-UV lithography process (ASML 5500, 248 nm) and reactive ion etching (RIE) with sulfur hexafluoride, oxygen, and argon ($SF_6/O_2/Ar$) to remove ∼23 nm of Si. Waveguides

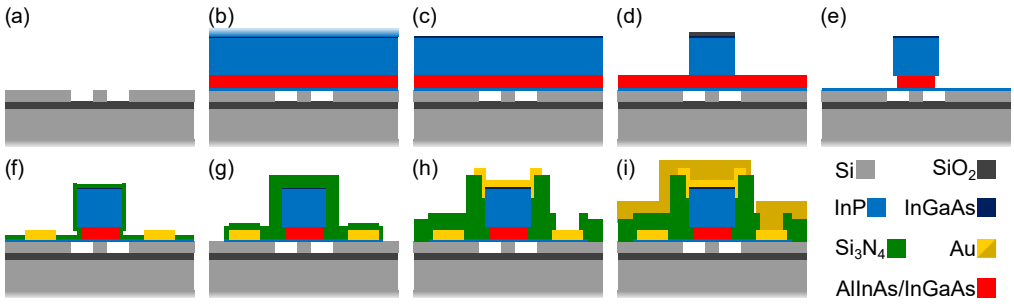

Figure 7.6: (a) Gratings and Si waveguides are defined. (b) QCL chip is bonded to the Si wafer. (c) InP substrate is removed. (d) Top contact and cladding are dry etched. (e) Active region is wet etched. (f) Bottom contact region is defined and metal is deposited. (g) Si_3N_4 is deposited and bottom cladding and contact are etched. (h) Vias are etched and the top metal is deposited. (i) Probe metal is deposited.

are then defined with a similar lithography process and are etched through the Si device layer down to the SiO_2 lower cladding. In both processes, a 4:1 mixture of sulfuric acid and hydrogen peroxide held at 80 °C strips the photoresist.

Next, the QCL EPI is prepared for bonding. The 50-mm diameter wafers are protected by spinning photoresist, then are cleaved with a diamond scribe to allocate a ∼10-mm square area for bonding over a 7.8-mm^2 die. Photoresist is removed with *N*-methyl-2-pyrrolidon (NMP). The bonding area is inspected in the microscope to identify grown defects. These are recorded to choose an orientation that will maximize yield. The 230-nm thick InGaAs capping layer is removed with a 1:1:38 mixture of H_3PO_4:H_2O_2:H_20 for 5 minutes, which selectively stops on the InP bonding layer. The patterned SOI wafer is cleaned with an 8-s etch in buffered hydrofluoric acid (BHF).

Bonding is precluded by an O_2 plasma surface activation (EVG) with 75 W capacitively coupled forward power and a 150 W plasma at 0.2 mbar. A vacuum wand is used to lift the EPI from the backside and place down the die to form an instantaneous bond. Before lifting the vacuum wand, a cotton swab is applied to the back of the EPI to prevent the vacuum wand from lifting the EPI. The bond is strengthened with a 2-hr anneal at 300 °C under compression of ∼2750-kPa applied by a graphite bonding fixture.

The InP substrate of the bonded QCL EPI is removed in two steps after protecting the wafer with photoresist. First, the substrate is mechanically polished with a 30-µm grit diamond film after covering the edges of the bonded EPI with an adhesive wax (Crystalbond 509), leaving ∼100 µm of substrate. Second, a hydrochloric acid (HCl) bath etches the remaining InP substrate, stopping selectively at the InGaAs layer. The wax and photoresist are removed with acetone, isopropanol, and de-ionized (DI) water. Large features are formed on two sides of the bonded EPI due to the crystallographic HCl etch. These are removed with a razor blade, though these could be dry-etched with a lithography process for a larger scale fabrication process.

Laser mesas are defined with the deep-UV stepper in photoresist on top of a polydimethylglutarimide (PMGI) underlayer. A SiO_2 hardmask is deposited by electron beam (e-beam) evaporation and lifted off with NMP. The InP top contact and upper cladding are etched with an inductively coupled plasma (ICP) reactive ion etch (RIE) of methane, hydrogen, and argon (CH_4/H/Ar) at flows of 4/20/10 sccm, a pressure of 75 mT and a bias of 500 V. A laser monitor allows to precisely stop after entering the AlInAs/InGaAs QC structure. This takes about 1 hr and is followed by a 20-minute O_2 etch at 20 sccm, 125 mT, and 300 V bias to clean residue.

All remaining lithography steps are done with an i-line stepper (GCA AutoStep 200) that is compatible with pieces of wafers. To enable more flexibility in our process, the wafer is diced to isolate each die: the DFB and the DBR designs.

The QC structure active region is etched with a 1:5:15 mixture of H_3PO_4:H_2O_2:DI in 22-s steps, lithographically defining the photoresist pattern each time, until the bottom cladding is visible. The hardmask, previously used to define the laser mesa, is then removed with BHF for 2 minutes.

A 100-nm thick silicon nitride (Si_3N_4) hardmask is deposited with plasma enhanced chemical vapor deposition (PECVD) and photoresist is patterned for the bottom metal

contact. The Si_3N_4 is etched with an ICP-RIE with $CF_4/CHF_3/O_2$ at 5/10/35 sccm, 500 W plasma, 50 W forward power, and 0.5 Pa. Another $CH_4/H/Ar$ ICP-RIE etch is performed to remove ∼150-nm InP lower cladding layers to expose the 1×10^{18} cm^{-3} doped InP. Next, the bottom metal of Pd/Ge/Pd/Au/Ti is deposited with thicknesses of 10/110/25/1000/10 nm on a bi-layer of PMGI and photoresist and is lifted off with acetone followed by a tetramethylammonium hydroxide (TMAH) developer.

To etch the bottom contact layer, a 300-nm thick PECVD Si_3N_4 hardmask is deposited and patterned. The hardmask is etched with $CF_4/CHF_3/O_2$ ICP-RIE and the InP bottom contact is etched with the $CH_4/H/Ar$ ICP-RIE.

A 1200-nm thick Si_3N_4 layer is deposited with PECVD, serving as the waveguide upper cladding and as an electrical isolation layer between contact metals. Vias are patterned and etched in this Si_3N_4 layer to expose the top and bottom contact areas. The top contact metal, with the same recipe as the bottom contact metal, is then patterned, deposited, and lifted off, followed by a similar process for the probe metal of Ti/Au with thicknesses of 23/1500 nm. Devices are diced and facets are polished.

Before bonding the III–V EPI, SEMs are performed. The entire AWG FPR is shown in Fig. 7.7(a) and the interface between the arrayed waveguides and the FPR is shown in Fig. 7.7(b). An SEM of the grating etched into the Si waveguide in Fig. 7.7(c) indicates that a duty cycle of ∼49.0 % is fabricated, defined as the ratio between the lengths of the etched section to the grating period. After bonding III–V EPI and etching the upper cladding, an SEM is taken of the taper transition region in Fig. 7.7(d), showing a slight undercut of the SiO_2 hardmask. This should not greatly affect the mode transition to the Si waveguide and may possibly make the conversion more efficient.

A schematic of the multi-spectral laser is shown in Fig. 7.8(a) with the micrograph of one device in Fig. 7.8(b). Non-uniform dark patterns can be seen in the Fig. 7.8(b). These appeared after the thick Si_3N_4 deposition during the step in Fig. 7.6(g). Ellipsometry

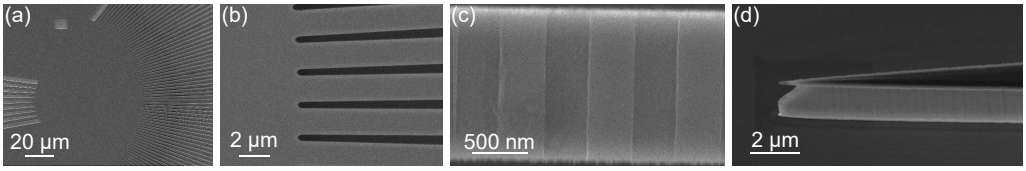

Figure 7.7: SEM of QCL taper tip before etching the n-QC structure. The top layer is the SiO_2 hardmask.

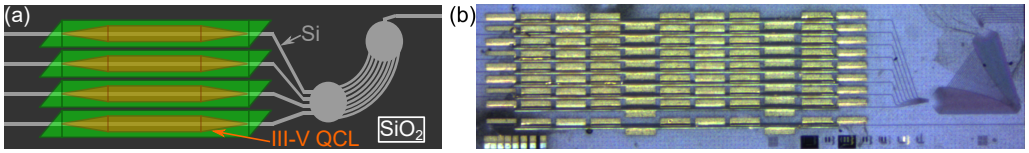

Figure 7.8: (a) Schematic and (b) micrograph of multi-spectral laser. Only 4 lasers are shown in (a) for simplicity. The actual devices in (b) have 8 lasers.

measurements indicate that 1190 nm was deposited, but the refractive index at 1550-nm wavelength is 1.53. Previous deposited layers of Si_3N_4 had indices near 1.92, so there was a problem with this final layer.

The experimental setups for the AWG and QCL characterizations are shown in Fig. 7.9(a–c), with a photograph of the QCL LIV setup in Fig. 7.9(d). AWG transmission measurements are in progress using the setup in Fig. 7.9(a). A CW tunable QCL (TL) emits a polarized free-space beam with powers up to ∼400 mW. The polarization controller (PC) consists of adjustable-angle half-wave and quarter-wave plates. A parabolic mirror (Lens) couples the free-space beam to an angled-facet indium fluoride (InF) fiber. The other side of the fiber is polished at with no angle and aligned to the input waveguide of an AWG test-chip. Parts of the multi-spectral QCL SOI wafer that were not used for bonding EPI were instead diced and polished as AWG test-chips. The output facet emits light to a similar fiber that is coupled to mercury cadmium telluride (HgCdTe) detector (DET, Vigo PVI-4TE) cooled with a thermoelectric cooler (TEC). A TEC is used with a thermistor and temperature control unit (Newport LDT-5500) to stabilize the AWG sample at room temperature.

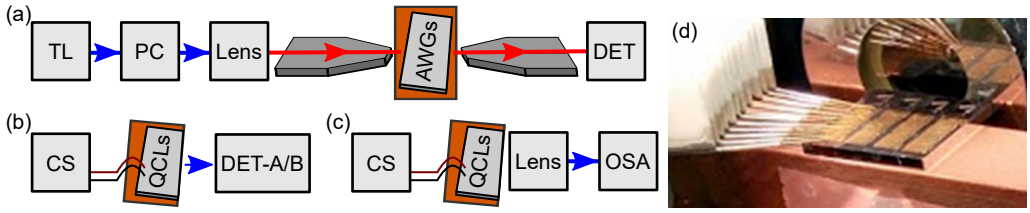

Figure 7.9: Experimental setups for (a) AWG passive transmission, (b) QCL LIV, and (c) QCL spectral measurements. (d) An photograph of the QCL LIV setup with DET-A is shown.

QCL experimental setups both use a pulsed current source (CS, Newport LDP-3830). Either one probe card, two probe cards, or individual probe needles are used to contact the probe pads on the lasers. A TEC, thermistor, and temperature control unit (Newport LDT-5500) are used to set the temperature of the copper stage in the range of 18–60 °C. In Fig. 7.9(b), a detector is aligned to the laser output for measuring light-current-voltage (LIV) characteristics[3]. Two detectors are used: DET-A (Vigo PVI-4TE) and DET-B (Vigo PVM-8). The first, DET-A, is more sensitive though the 1×1 mm^2 detector area does not capture all of the output light. The second, DET-B, has a 4×4 mm^2 detector area and is used for output power calibration with the detector very close to the laser output facet. Laser output spectra are measured with the setup in Fig. 7.9(c). An aspheric lens (Lens, Thorlabs 390037-E) collects light with a numerical aperture of ∼0.85 and focuses a beam into a Fourier transform infrared (FTIR) spectrometer (Bruker Vertex 70) with a liquid nitrogen (LN) cooled HgCdTe detector.

7.4 Experiments and results

After fabrication, devices are screened with the LIV test setup to determine which devices are lasing. Both front- and back-side outputs are measured. A summary of these measurements is reported in Table 7.4. During the bonding process, two pieces

[3]LIV characteristics measure output light power and junction voltage while driving current to the laser.

of EPI were cleaved and bonded over dies corresponding to chips DFB-1 and DBR-1. Small portions on the sides of these EPI pieces overlapped adjacent dies, corresponding to chips DFB-2 and DBR-2. Lasing was observed from 41 devices (in bold) out of 144 devices in total, a 28 % yield[4]. Some of these devices lased and then later became short circuits, while others initially were open circuits and then lased. For the devices that did not lase, 8 showed typical I-V, 34 showed short-circuit I-V, and 61 showed open-circuit I-V characteristics.

Three issues during the fabrication may be responsible for the poor device yield. First, the open-circuit may be caused be an insufficient etch down to the bottom contact layer. After this ICP-RIE etch, the depth measurement on a test structure indicated ∼50 nm penetration into the 1×10^{18}-cm^{-3} doped contact layer with total thickness of 230 nm. Due to an etch-loading effect, the etch depth into the actual laser contacts may have been less, since the array of lasers is more densely patterned during this etch than the test structures. This is supported by testing electrical conduction through the probe pads. Including the open-circuit devices, all of the top-contact pads are electrically connected with low resistance to each other. Only select bottom-contact pads showed open-circuit trends between pads. On the open-circuited devices, none of the bottom-contact had low resistance between pads. Second, due to the large topography of the QCL, spinning uniform layers of photoresist after the active region etch became a significant challenge[5]. As a result, areas over the densely patterned laser mesas have a much thicker photoresist layer than the III–V/Si taper features. During the photoresist thermal curing, air that was trapped under the laser expands and in some cases would create bubbles at the III–V taper tip if the photoresist was too thin. A small portion of these bubbles would burst

[4]This does not account for the die areas that did not overlap with bonded EPI. If this is accounted for, then the device yield is 31 %

[5]Nearly 60 lithography re-works had to be done on the lead chip to find a recipe with moderate yield.

Table 7.4: Summary of device yield. "**L**" means that the device is lasing. "**R**" means that the device was revived after initially operating as an open-circuit. "**D**" means that the device did lase and it has since stopped lasing (died), becoming a short-circuit. "G" means that the I-V trend is similar to others devices that lase, but these devices show no output light. "O" means that the device is an open-circuit and does not lase. "S" means that the device is a short-circuit and does not lase.

Chip	DFB-1				DFB-2				DBR-1				DBR-2			
Taper	A	B	C	D	A	B	C	D	A	B	C	D	A	B	C	D
#8	S	G	O	**D**	S	S	O	O	S	O	O	**D**	S	O	O	O
#7	S	O	O	**D**	O	O	O	O	S	**R**	O	O	O	O	**D**	O
#6	S	S	O	**R**	O	O	S	O	**L**	O	O	S	O	**R**	O	G
#5*	S	S	**R**	**L**	S	S	S	O	O	O	O	**D**	O	O	**L**	S
#4	**D**	S	O	**D**	**D**	O	S	O	**D**	**D**	O	O	O	O	**L**	**L**
#3	S	S	O	**L**	G	S	**D**	**L**	O	**D**	O	O	O	O	O	S
#2	S	G	O	G	**D**	O	**D**	S	**L**	**D**	O	O	O	O	O	O
#1	S	O	**L**	O	S	S	S	G	O	**L**	O	**L**	S	O	O	S
i*	**D**	**D**	**D**	S	**D**	**D**	**D**	S	S	**L**	**R**	**D**	**L**	**L**	G	G

during a metal deposition step, causing a short-circuit. The third issue is that some devices did not overlap with the bonded EPI.

7.4.1 Individual lasers

Examples of LIVs from the highest power backside outputs are shown in Fig. 7.10(a) for a DFB laser and Fig. 7.10(b) for a DBR laser. For both, the operating voltage is ∼14 V at 800-mA drive current. Some devices were tested with up to 1.6 A drive current without damage, but others were damaged at 1.0 A, so typical tests were limited to 800 mA to prevent damage. The maximum power for this DFB laser is ∼1.4 mW and for this DBR laser is ∼2.5 mW. In general, the DFB laser L-I curves show a single linear slope, while the DBR laser L-I curves show either multiple linear slopes or a higher order polynomial trend. This is likely due to the multiple longitudinal modes of the DBR lasers. As the current increases temperature an carrier dynamics give preference to different modes, which non-linearly changes the output power.

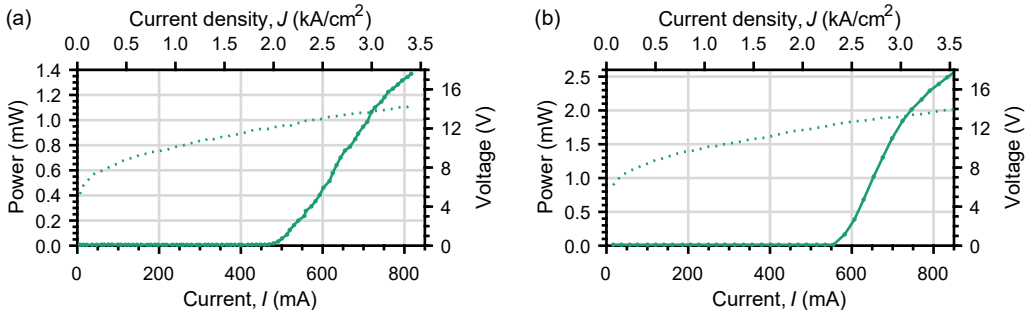

Figure 7.10: Example LIV characteristics for an (a) DFB (Channel 6, taper D, backside) and (b) DBR laser (Channel 5, taper A, backside).

For the lasers not coupled to an AWG, the LIVs from the front and backsides are plotted in Fig. 7.11 for DBRs. The R value indicated on each plot, which is the ratio of output power from the front side to the back side, defined as:

$$R = 10 \log_{10} \frac{P_{\text{max,front}}}{P_{\text{max,back}}} . \tag{7.1}$$

All of the individual DFB lasers were damaged so this analysis cannot be completed for the DFBs. However, some un-calibrated preliminary measurements on DFBs before damage occurred demonstrated R values of 1.0 dB for taper A and -2.3 dB for taper C. The variation in R is likely due to a corresponding variation in the III–V/Si taper reflection, loss, or both. Another effect that may influence this variation is imperfections in the Si facet polishing.

All measurements are conducted in pulsed mode. Increasing the duty cycle of the drive current is expected to degrade the output power as CW operation is approached and self-heating increases. The pulsed current driver is limited to a maximum duty cycle of 5.0 %, so this is still far from CW. Plots in Fig. 7.12 show the output power dependence on the duty cycle in the range of 0.01–5.00 % for pulse lengths of 500 ns and 1000 ns. For a visual aid, the output power is normalized to the output power from a 1.00-% duty cycle for each laser. The DFB and DBR lasers show less then 10 % and 30 % change in

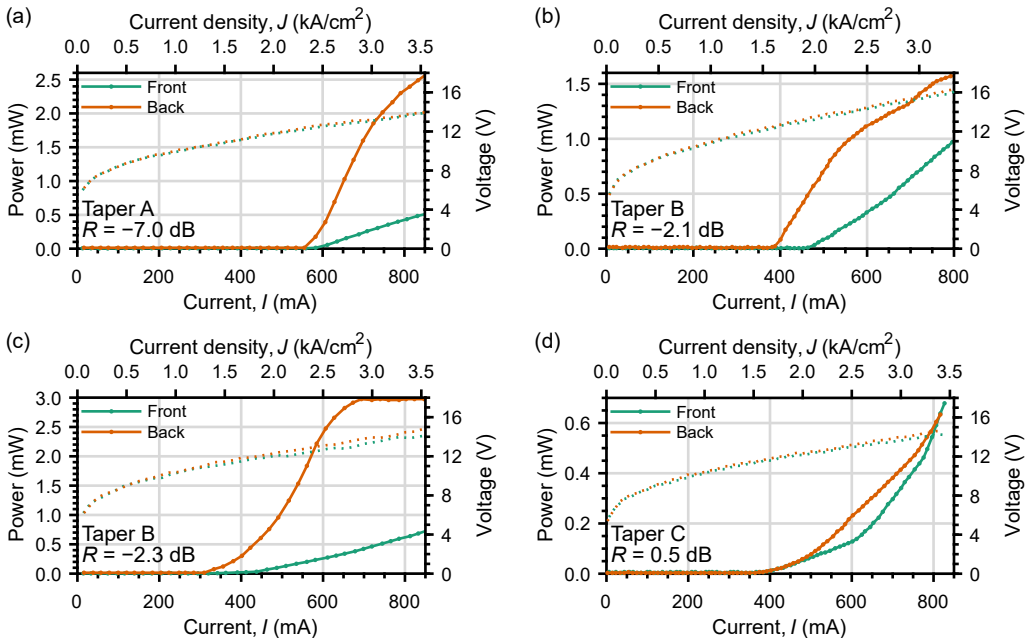

Figure 7.11: LIV characteristics from individual DBR lasers (not coupled to AWGs) to extract the ratio, R, of output power from the front side to the back side.

output power, with one being positive and the other negative for each laser type. Within this duty cycle range, there is no clear trend of increasing or decreasing output power. Mode preference due to heating and carrier concentrations are likely the dominant effects changing the output powers for these experiments. This result is encouraging, since the previous QCL on SONOI devices showed a strong trend of decreasing output power in this same duty cycle range. These previous devices did not lase at CW, even at low temperatures down to 77 K (LN cooled). However, these data suggest that CW lasing more likely from these QCL on SOI devices. Experiments are currently in progress to test for CW operation.

The output power dependence on pulse width is investigated next. With the pulse period held constant at 50 µs, the pulse width is varied from 100 ns to 1000 ns while LIVs are recorded from a DFB and a DBR laser in Fig. 7.13. Between 400 ns and 1000 ns, the DFB LIV trends are nearly constant for the entire drive current range. The DBR

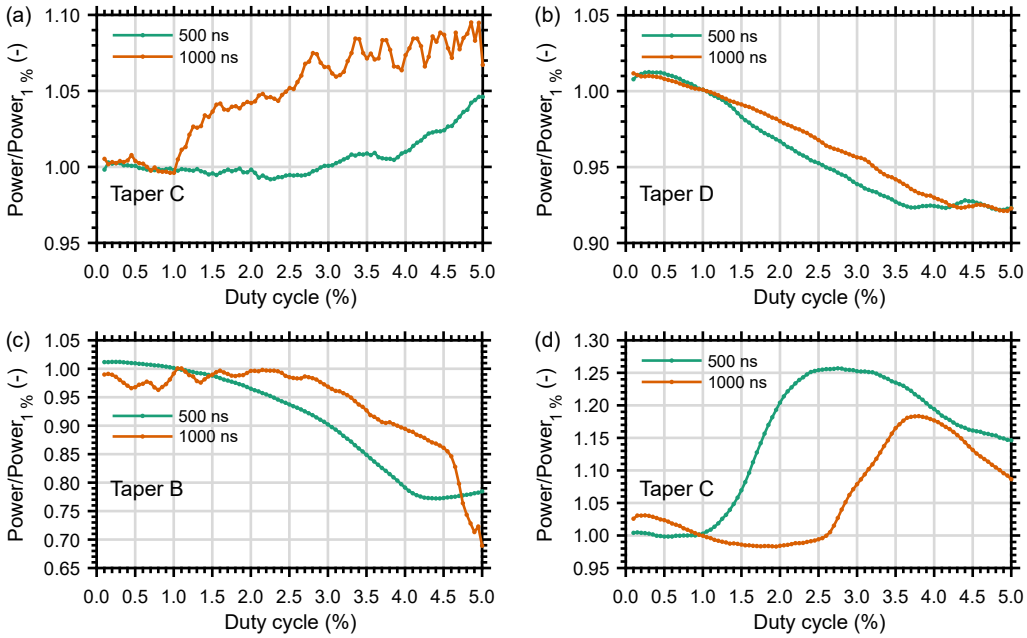

Figure 7.12: Output power dependence on the duty cycle for (a,b) DFB and (c,d) DBR devices, all from Channel 5.

lasers show a similar trend for that pulse width range, however, for driver currents above 650 mA, the output power trend takes a different shape for each pulse width. Again, this is likely a consequence of the multiple longitudinal modes in the DBR lasers. For both laser types, a decreased output power is observed for 100 ns and 200 ns pulse widths. This may not be trend inherent to the lasers. The Vigo PVI-4TE detector pre-amplifier has a bandwidth of ∼1.0 MHz, which limits the response for pulse widths less than 400 ns.

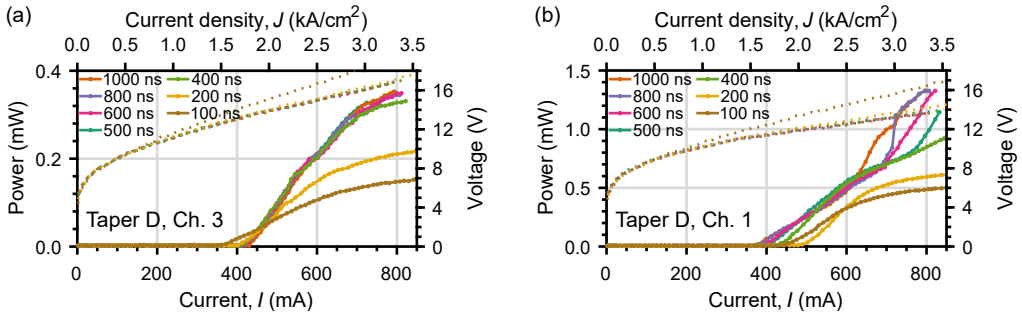

Figure 7.13: LIV dependence on the pulse width for (a) DFB and (b) DBR devices with the pulse period held constant at 50 µs.

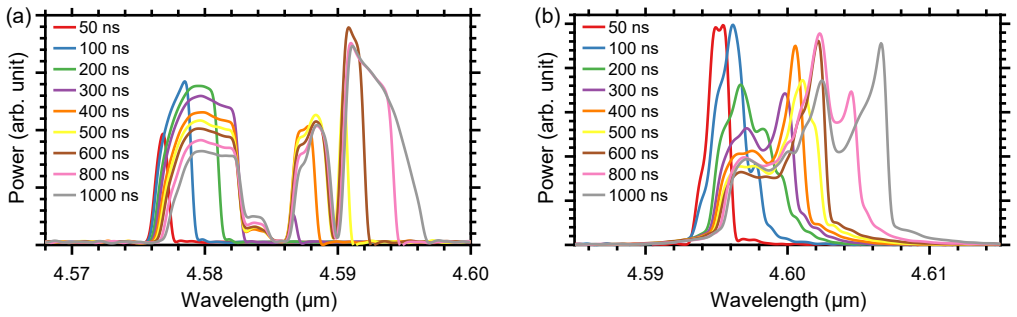

Figure 7.14: Spectral dependence on the pulse width for (a) a DFB from Channel 3 with taper design D and (b) a DBR from Channel 4 with taper design A.

For the same pulse width dependence, the output spectra are measured and plotted in Fig. 7.14. For both laser types, short pulses seem to have a single and narrow spectral width. As the pulse length increases, the spectra broaden and power is transferred to one or more longer wavelength spectral peaks. It is probable that this trend is due to heating, since longer pulses will cause a greater increase in temperature of the active region and surrounding materials. Multiple effects are responsible for the wavelength shift due to increased temperature. The thermo-optic effect is the change in refractive index of a material due to temperature and this will change the grating Bragg wavelength and optical path length of the gain region. Thermal expansion of the materials also modifies the band structure, which can shift the gain peak of the active region and thus change the lasing wavelength. Resistance also increases with temperature, which can compound these effects.

The LIV temperature dependence for each laser is plotted in Fig. 7.15 for temperatures in the range of 20–60 °C. A linear fit is performed on the first 10 data points above an estimated threshold current to find the actual threshold current and slope efficiency. The fitted lines are shown in black and black circles indicate the threshold currents. As expected threshold currents increase and slope efficiencies decrease with temperature.

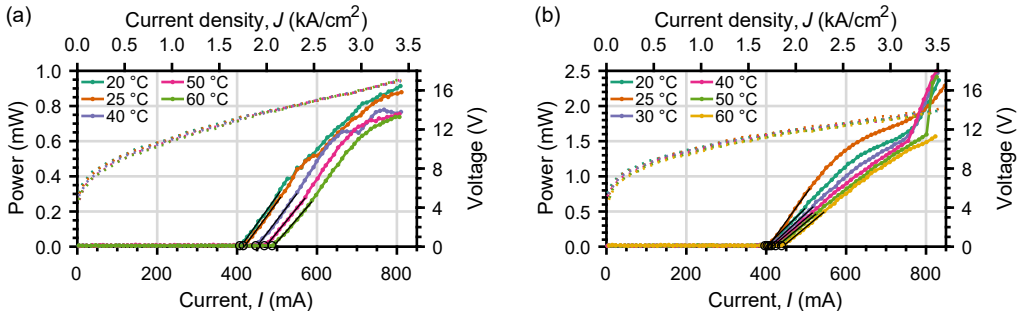

Figure 7.15: LIV dependence on the temperature for (a) DFB and (b) DBR devices.

Extracted threshold current densities (J_{th})[6] and slope efficiencies (η_{d})[7] are then plotted in Fig. 7.16. The data are fitted to the following exponential equations:

$$J_{\text{th}} = J_0 e^{T/T_0}\,, \tag{7.2a}$$

$$\eta_{\text{d}} = \eta_1 e^{-T/T_1}\,. \tag{7.2b}$$

For the DFB laser, $T_0 = 218 \pm 5$ K and $T_1 = 220 \pm 10$ K and for the DBR laser, $T_0 = 423 \pm 33$ K and $T_1 = 160 \pm 34$ K[8]. The variation between laser types is not expected to be due to the mirror types, but rather is likely due to fabrication variation. Also, note that the standard errors are much larger for the DBR laser because of the complex dynamics of lasing from multiple longitudinal modes. For comparison, these values from the previous QCL on SONOI demonstration, with 3-mm gain lengths, were $T_0 = 199$ K and $T_1 = 222$ K.

[6]Threshold currents are divided by the active region width of ∼6.0 µm and length of ∼4.0 mm to obtain the threshold current densities.

[7]The slope of the output power as a function of input current above threshold is multiplied by elementary charge and divided by the photon energy to find the slope efficiency η_{d}.

[8]Values listed after the ± symbols represent the standard uncertainty, *i.e.*, the 34.1 % confidence interval.

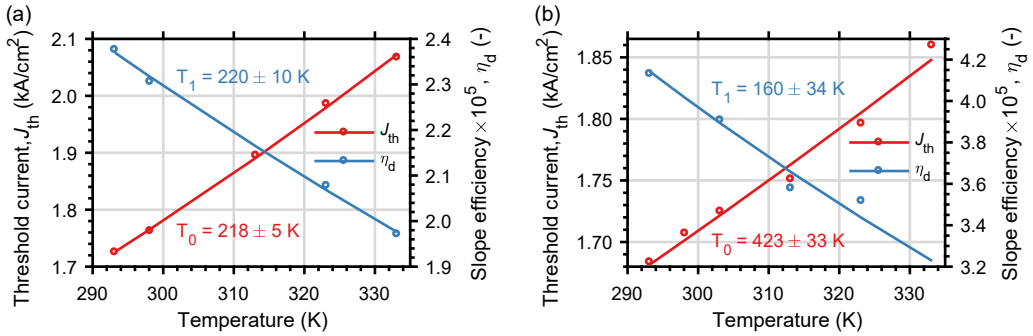

Figure 7.16: Extracted threshold and slope efficiency characteristic temperatures for (a) DFB and (b) DBR devices.

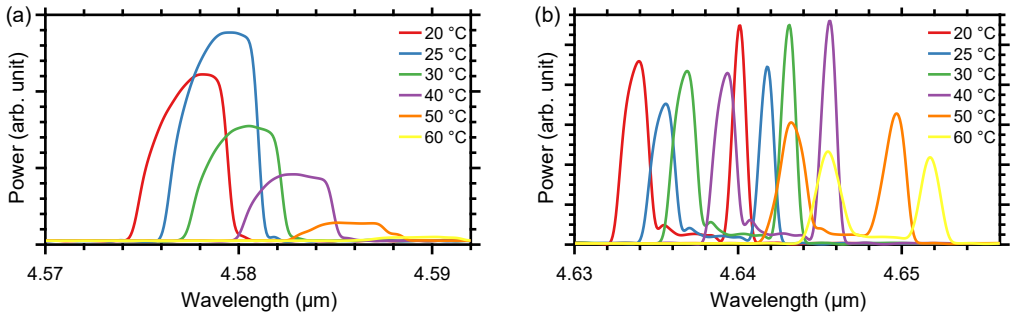

Figure 7.17: Spectral dependence on the temperature for (a) a DFB from Channel 2 with taper design C and (b) a DBR from Channel 5 with taper design D.

The output spectra of the temperature dependent measurements are plotted for a DFB in Fig. 7.17(a)[9] and for a DBR in Fig. 7.17(b). The DFB and DBR lasers are driven with 200 ns and 100 pulse widths, respectively, both with an 800-mA current level. Tracking the peak wavelengths of the DFB and DBR spectra results in a linear tuning of ∼0.27 nm/°C and ∼0.30 nm/°C, respectively.

To investigate the performance of the III–V/Si taper, one chip is polished through this taper transition, leaving a hybrid III–V/Si waveguide at the back-side output facet. LIVs and spectra from two devices on this chip are measured before and after removing the taper and the results are plotted in Fig. 7.18. Maximum powers from these two DFB

[9]The spectrum of the DFB laser at 25 °C was taken at a different time from the rest of the measurements. The higher power is expected to be due to better alignment since the calibrated power measurement in Fig. 7.15(a) does not follow the same trend.

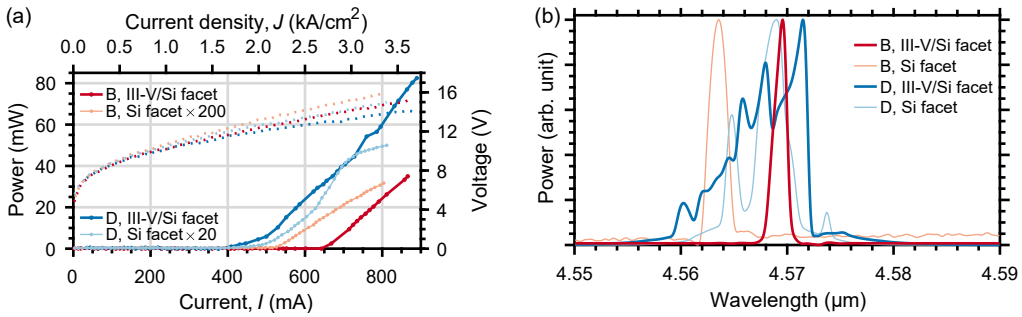

Figure 7.18: (a) LIVs and (b) spectra from a hybrid III–V/Si facet after polishing off the III–V/Si taper.

devices with light output from the hybrid III–V/Si facet are 82.5 mW and 35.0 mW at 890 mA and 866 mA, respectively. Before polishing off the taper, maximum powers from these devices with light output from the passive Si facet are 2.50 mW and 0.16 mW at 812 mA and 804 mA, respectively. These values correspond to ∼33× and ∼219× increases in the output power after removing the tapers. For the higher power laser, the threshold current is about the same before and after the taper polishing, but for the lower power laser the threshold current increases ∼ 24%. It is unclear why this value increases, but it could be due to phase of the hybrid III–V/Si facet reflection causing an increased mirror loss. The normalized spectra in Fig. 7.18(b) show that for both lasers, the peak of the output light is red-shifted after removing the taper.

7.4.2 Multi-spectral lasers

For each functioning multi-spectral laser, LIVs and spectra are measured from the front output, through the AWG. Also, during LIV measurements, all permutations of driving 1, 2, or 3 lasers simultaneously are shown. Spectra are measured for 750 mA and 800 mA per laser for 200 ns, 350 ns, and 500 ns pulse widths. The laser channel numbers are annotated on each plot. Measurements for a multi-spectral DFB laser with taper C are shown in Fig. 7.19, DFB laser with taper D are shown in Fig. 7.20, DBR

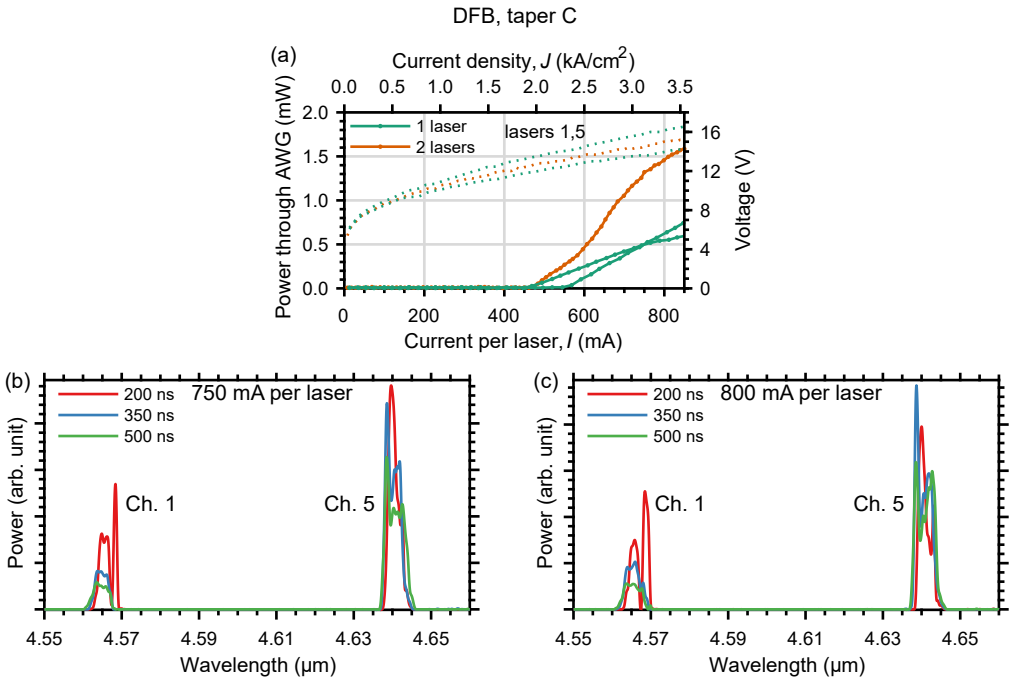

Figure 7.19: LIV plots of a multi-spectral two-channel DFB while driving laser channels 1 and 5. Spectra of the simultaneously driven two-channel DFB laser for three different pulse widths with (b) 750 mA and (c) 800 mA drive current per laser.

laser with taper A are shown in Fig. 7.21, DBR laser with taper B are shown in Fig. 7.22, and DBR laser with taper C are shown in Fig. 7.23. The maximum number of lasers in one multi-spectral laser is 3, shown in Fig. 7.20. These measurements require two probe cards and a set of individual probes to drive all lasers at once. Also, the drive current is plotted per laser, which uses the assumption that the drive current is split equally between lasers. Note that this is not explicitly correct since the series resistance of each laser is slightly different. Therefore, when driving two lasers, the actual drive current is 2× the values shown. When driving three lasers, the actual drive current is 3× the values shown. For all LIV plots, the pulse width is 500 ns. The highest multi-spectral output power is ∼1.6 mW and comes from the DFB laser with taper C.

One key concern about driving multiple lasers at once is that heating will degrade the output power while driving all lasers simultaneously relative to the sum of driving

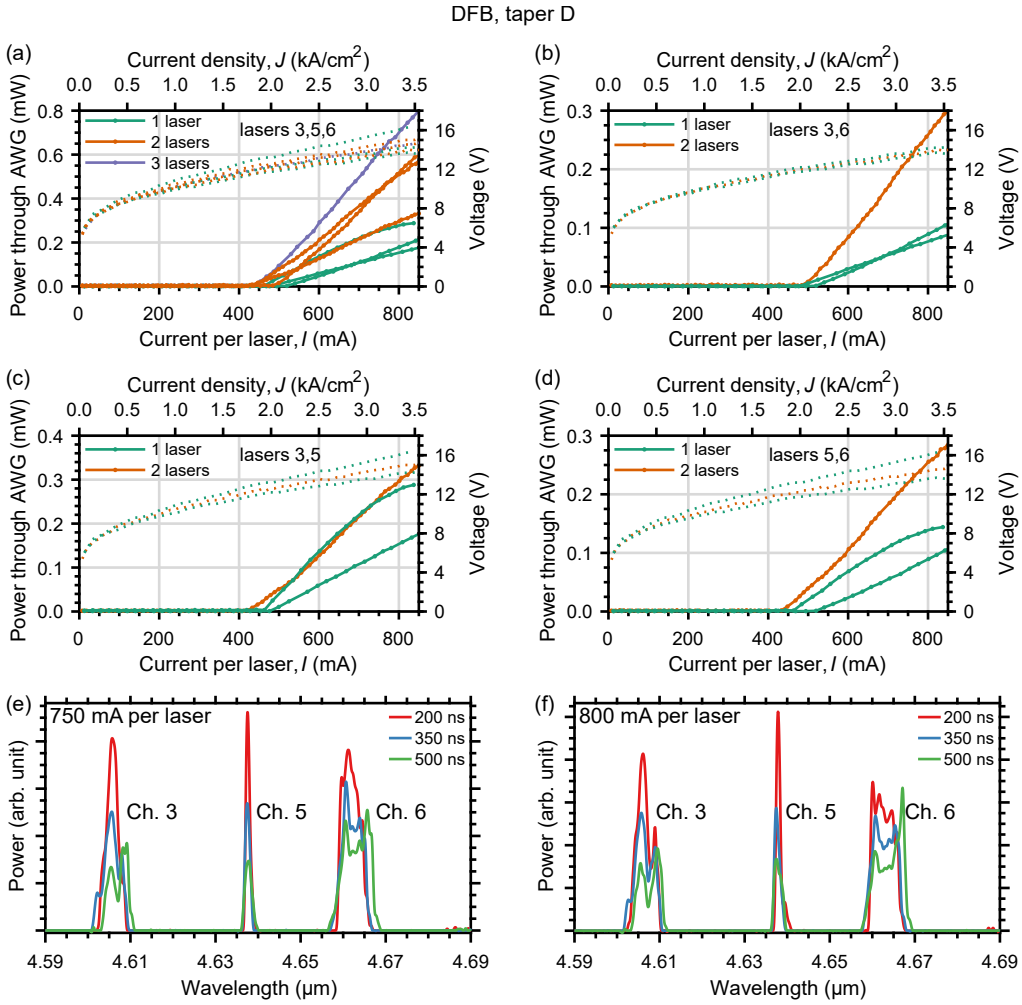

Figure 7.20: LIV plots of a multi-spectral three-channel DFB while driving laser channels (a) 3, 5, and 6; (b) 3 and 6; (c) 3 and 5; (d) 5 and 6. Spectra of the simultaneously driven three-channel DFB laser for three different pulse widths with (e) 750 mA and (f) 800 mA drive current per laser.

each laser individually. This figure-of-merit is termed the "power degradation" (D) and calculated as:

$$D = 10 \log_{10} \frac{P_{\text{mult.,max}}}{\sum_{x=1}^{N_{\text{laser}}} P_{x.\text{max}}} . \tag{7.3}$$

This parameter depends on drive current and temperature, which is evident from the temperature-dependent LIV characteristics in Fig. 7.15. The thermal crosstalk scales with

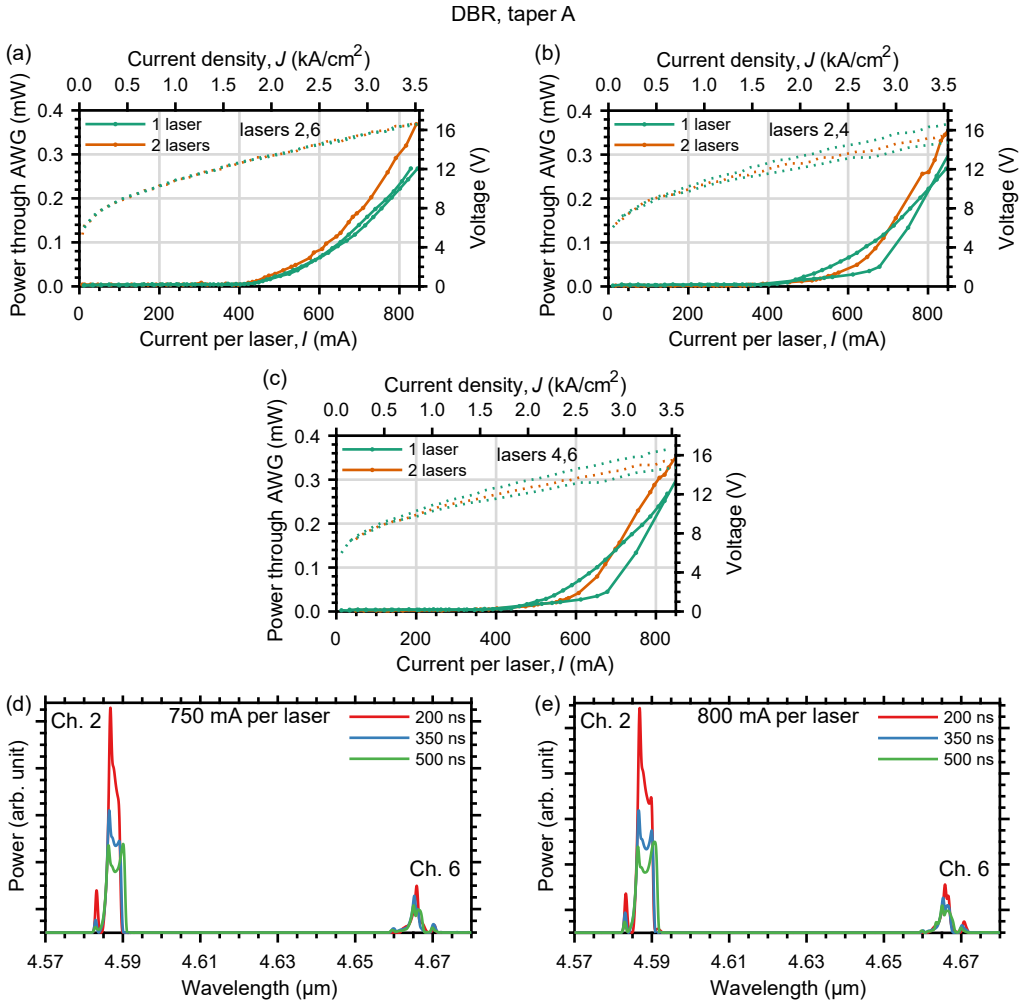

Figure 7.21: LIV plots of a multi-spectral two-channel DBR while driving laser channels (a) 1 and 7; and (b) 1 and 8.

the inverse of the distance between lasers [21]. If D is influenced by thermal crosstalk, then a similar trend would be observed for the laser proximity dependence on D.

The power degradation D is calculated for each multi-spectral laser and listed in Table 7.5. From these data, it is evident that D is not dependent on taper design. Interestingly, for the 3-channel multi-spectral DFB laser, the D values when driving all 3 lasers at once is nearly equal to the average of the D values when driving 2 lasers at once: $D_{3,5,6} = 0.88$ dB compared to $(D_{3,6} + D_{3,5} + D_{5,6})/3 = (1.89 - 1.54 + 0.50)/3 = 0.85$.

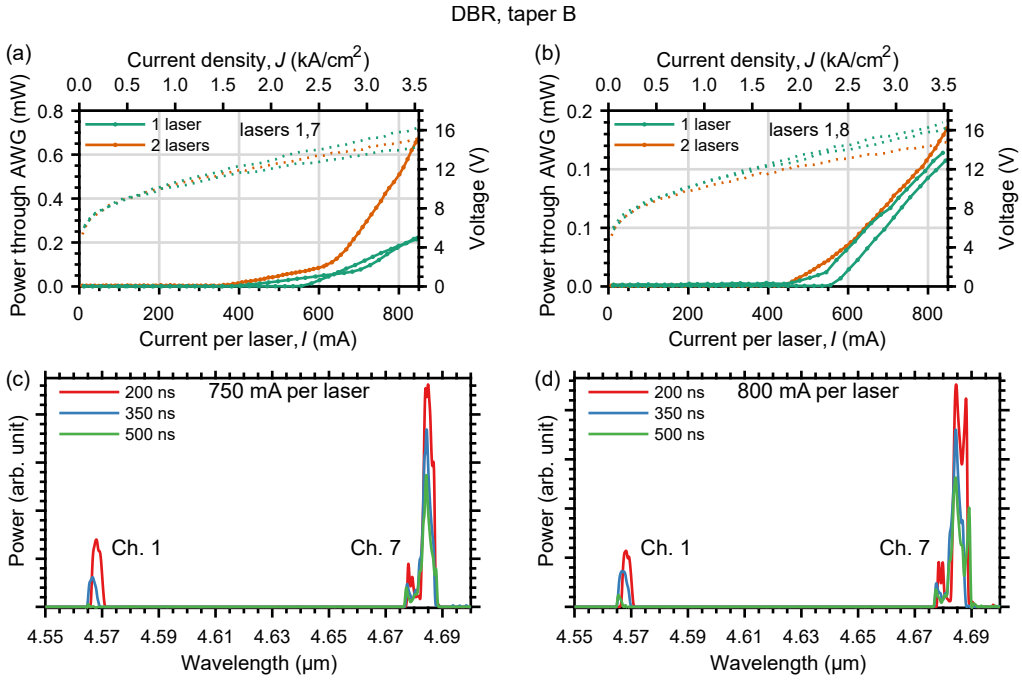

Figure 7.22: LIV plots of a multi-spectral two-channel DBR with taper design B while driving laser channels (a) 1 and 7; and (b) 1 and 8.

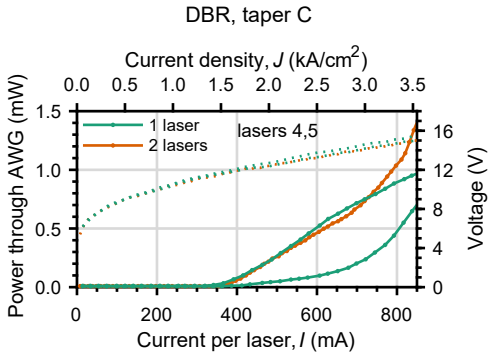

Figure 7.23: LIV plots of a multi-spectral two-channel DBR with taper design C while driving laser channels 4 and 5.

Since there is only one device with more than two channels in operation, this analysis cannot be used to draw conclusions since this could just be a coincidence.

In Fig. 7.24, D is plotted for each pair of lasers coupled through an AWG against the distance between the laser mesas. If thermal crosstalk is responsible for the degradation, then a decreasing trend as the distance between lasers increases would be expected for D.

Table 7.5: Power degradation (D) for each multi-spectral laser.

Lasers	Reference to figure	D (dB)
DFB, taper C: 1,5	Fig. 7.19(a)	0.56
DFB, taper D: 3,5,6	Fig. 7.20(a)	0.88
DFB, taper D: 3,6	Fig. 7.20(b)	1.89
DFB, taper D: 3,5	Fig. 7.20(c)	−1.54
DFB, taper D: 5,6	Fig. 7.20(d)	0.50
DBR, taper A: 2,6	Fig. 7.21(a)	−1.63
DBR, taper A: 2,4	Fig. 7.21(b)	−2.20
DBR, taper A: 4,6	Fig. 7.21(c)	−2.60
DBR, taper B: 1,7	Fig. 7.22(a)	1.81
DBR, taper B: 1,8	Fig. 7.22(b)	−2.34
DBR, taper C: 4,5	Fig. 7.23	−0.73

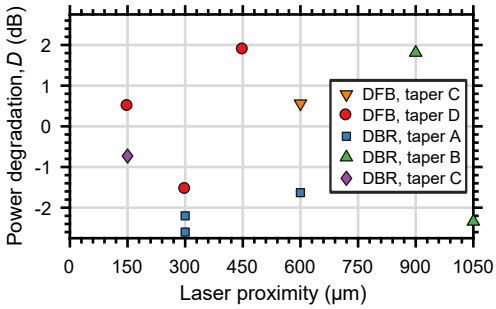

Figure 7.24: Power degradation dependence on proximity of two lasers for ∼800 mA drive current and a temperature of 25 °C.

However, this trend is not evident, so the degradation must arise from other effects. The difference in series resistance between lasers may cause the variation in D, which would imply that the degradation is not inherent to the devices. Rather, if separate current sources were available to drive current through each laser at independent voltage levels, then D may not vary as much as in Fig. 7.24 and may show a different trend with laser proximity.

A general comment that seems to apply to all multi-spectral lasers is that the junction voltage when driving multiple lasers at once takes, approximately, the average value of the voltages when driving the lasers separately. Although trends are not apparent, the differences in junction voltage or, similarly, differences in laser series resistance may affect

D. For an example with two lasers, if one laser has a high series resistance while the other has a low series resistance, more than half of the drive current will flow through the one low-resistance device.

7.5 Summary and conclusion

QCLs heterogeneously integrated on SOI waveguide have been demonstrated for the first time. Output powers of up to 2.5 mW from passive Si waveguides and up to 82.5 mW from hybrid III–V/Si facets are observed. Pulse duty cycle, pulse width, and device temperature trends from LIV and spectral measurements were analyzed, despite poor device yield plagued this experiment.

The III–V/Si taper transition is limiting the output power coupled to the passive Si waveguide and improvements are possible to increase the light coupled from the gain section to the passive waveguide. One possibility is that the active region undercut due to the wet etch process causes high-loss in the tapers. Using a chlorine-based dry etch is expected to remove the undercut and decrease this loss.

A multi-spectral QCL has also been demonstrated on the SOI platform by spectrally combining the beams from multiple lasers emitting in the range of 4.6–4.7 µm with an AWG. In one case, three lasers are combined, and in three other cases, two lasers are combined. Both DFB and DBR laser types are demonstrated with multi-spectral outputs. This is the first PIC with integrated QCLs on a Si substrate and its demonstration marks an important step towards large-scale, low-cost, and high-performance mid-IR photonic devices.

For future work, reducing the waveguide loss is an important step to make the AWG combiner more efficient. If the taper loss can also be significantly decreased, then it may be feasible to construct a multi-spectral DBR laser with back-mirrors under the III–V

material and a common front mirror for all channels located on the output side of the AWG. To take full advantage of this laser architecture, an experimental investigation of optimized output beam quality is possible to maximize the output brightness. This demonstration allows for this unique ability to tune the output waveguide cross-sectional geometry to minimize M^2.

References

[1] O. Cathabard, R. Teissier, J. Devenson, J. C. Moreno, and A. N. Baranov, "Quantum cascade lasers emitting near 2.6 µm," Appl. Phys. Lett. **96**, 141110 (2010).

[2] C. Walther, M. Fischer, G. Scalari, R. Terazzi, N. Hoyler, and J. Faist, "Quantum cascade lasers operating from 1.2 to 1.6 thz," Appl. Phys. Lett. **91**, 131122 (2007).

[3] A. Lyakh, R. Maulini, A. Tsekoun, R. Go, C. Pflügl, L. Diehl, Q. J. Wang, F. Capasso, and C. K. N. Patel, "3 w continuous-wave room temperature single-facet emission from quantum cascade lasers based on nonresonant extraction design approach," Appl. Phys. Lett. **95**, 141113 (2009).

[4] Y. Bai, N. Bandyopadhyay, S. Tsao, S. Slivken, and M. Razeghi, "Room temperature quantum cascade lasers with 27% wall plug efficiency," Appl. Phys. Lett. **98**, 181102 (2011).

[5] B. G. Lee, J. Kansky, A. K. Goyal, C. Pflügl, L. Diehl, M. A. Belkin, A. Sanchez, and F. A. Capasso, "Beam combining of quantum cascade laser arrays," Opt. Express **17**, 16216–16224 (2009).

[6] P. Rauter and F. Capasso, "Multi-wavelength quantum cascade laser arrays," Laser Photon. Rev. **9**, 452–477 (2015).

[7] W. Zhou, D. Wu, R. McClintock, S. Slivken, and M. Razeghi, "High performance monolithic, broadly tunable mid-infrared quantum cascade lasers," Optica **4**, 1228–1231 (2017).

[8] A. Spott, J. Peters, M. L. Davenport, E. J. Stanton, C. D. Merritt, W. W. Bewley, I. Vurgaftman, C. S. Kim, J. R. Meyer, J. Kirch, L. J. Mawst, D. Botez, and J. E. Bowers, "Quantum cascade laser on silicon," Optica **3**, 545–551 (2016).

[9] A. Spott, J. Peters, M. L. Davenport, E. J. Stanton, C. Zhang, C. D. Merritt, W. W. Bewley, I. Vurgaftman, C. S. Kim, J. R. Meyer, J. Kirch, L. J. Mawst, D. Botez, and

J. E. Bowers, "Heterogeneously Integrated Distributed Feedback Quantum Cascade Lasers on Silicon," Photonics **3**, 35 (2016).

[10] S. Jung, J. Kirch, J. H. Kim, L. J. Mawst, D. Botez, and M. A. Belkin, "Quantum cascade lasers transfer-printed on silicon-on-sapphire," Appl. Phys. Lett. **111**, 211102 (2017).

[11] E. J. Stanton, M. J. Heck, J. Bovington, A. Spott, and J. E. Bowers, "Multi-octave spectral beam combiner on ultra-broadband photonic integrated circuit platform," Opt. Express **23**, 11272–11283 (2015).

[12] A. Spott, E. J. Stanton, N. Volet, J. D. Peters, J. R. Meyer, and J. E. Bowers, "Heterogeneous Integration for Mid-Infrared Silicon Photonics," IEEE J. Sel. Topics Quantum Electron. (2017).

[13] A. Malik, M. Muneeb, S. Pathak, Y. Shimura, J. Van Campenhout, R. Loo, and G. Roelkens, "Germanium-on-Silicon Mid-Infrared Arrayed Waveguide Grating Multiplexers," IEEE Photon. Technol. Lett. **25**, 1805–1808 (2013).

[14] M. Muneeb, X. Chen, P. Verheyen, G. Lepage, S. Pathak, E. Ryckeboer, A. Malik, B. Kuyken, M. Nedeljkovic, J. Van Campenhout, G. Z. Mashanovich, and G. Roelkens, "Demonstration of Silicon-on-insulator mid-infrared spectrometers operating at 3.8 µm," Opt. Express **21**, 11659–11669 (2013).

[15] S. A. Miller, M. Yu, X. Ji, A. G. Griffith, J. Cardenas, A. L. Gaeta, and M. Lipson, "Low-loss silicon platform for broadband mid-infrared photonics," Optica **4**, 707–712 (2017).

[16] L. A. Coldren, S. W. Corzine, and M. L. Mašanović, *Diode lasers and photonic integrated circuits*, vol. 218 (John Wiley & Sons, 2012), 2nd ed.

[17] M. L. Davenport. Personal communication.

[18] E. Stanton, A. Spott, M. Davenport, N. Volet, and J. Bowers, "Low-loss arrayed waveguide grating at 760 nm," Opt. Lett. **41**, 1785–1788 (2016).

[19] E. J. Stanton, N. Volet, and J. E. Bowers, "Low-loss demonstration and refined characterization of silicon arrayed waveguide gratings in the near-infrared," Opt. Express **25**, 30651–30663 (2017).

[20] E. J. Stanton, N. Volet, and J. E. Bowers, "Silicon arrayed waveguide gratings at 2.0-µm wavelength characterized with an on-chip resonator," Opt. Lett. **in press** (2017).

[21] K. Sato and M. Murakami, "Experimental investigation of thermal crosstalk in a distributed feedback laser array," IEEE Photon. Technol. Lett. **3**, 501–503 (1991).

Chapter 8

Conclusion

8.1 Summary

A high-brightness laser is demonstrated by integrating lasers on Si and spectrally combining each to a single multi-spectral output. A particular architecture is proposed using Si, SiO_2, and Si_3N_4 passive waveguides and lasers grown on GaN, GaAs, InP, and GaSb substrates. Design methodologies are discussed and experiments are performed on the spectral beam combining elements consistent with this platform. The high fundamental-mode transmission observed in each demonstration validates the design process. These investigations show lower on-chip loss values than previous reports on similar devices. Integrating a QCL array with an AWG is the first step in demonstrating this high-brightness laser concept. Analyses of the QCL on SOI laser characteristics provide new understandings for the design, performance, and capabilities of this platform.

8.2 Prospectives

Future work will integrate the AWGs with lasers and, potentially, SOAs at wavelengths spanning the near-IR to the mid-IR. To convey the current capability of this platform, a spectrally combined output power is calculated using the maximum output powers of individual lasers and the on-chip losses of AWGs and beam combiners. For lasers spanning the VIS to the mid-IR with eight channels per band, this multi-spectral laser architecture can produce >400 mW in the fundamental mode [1–4]. Further improvements to the maximum power per laser are expected as the III–V/Si tapers are optimized, waveguide loss is decreased, and thermal dissipation is increased. Another way to deliver higher multi-spectral power is to increase the number of channels per band. A thorough study is necessary to determine the limits, though ∼20 lasers per band seems feasible based on the footprint of single lithographic field. While scaling to higher power is necessary for IRCM applications, molecular detection and quantification is a viable with the currently demonstrated devices characteristics.

8.2.1 Outlook for lasers on silicon

In the near-IR, device yield for heterogeneously integrated lasers on Si has been demonstrated up to 99 % [5]. Device yield for the QCLs on Si can be improved with the three following recommendations. First, the QCL EPI should be planarized before bonding. This could be done by first depositing a layer of SiO_2 in the form of spin-on-glass, then using a chemical-mechanical-polishing (CMP) tool to remove this SiO_2 layer along with any large defects protruding from the EPI surface. Reducing the number of large protrusions will minimize bond failures. A bond defect of ∼5 µm in diameter and height may cause a bond fail area of ∼50 µm in diameter. If the surface is instead planarized, then the bond may not fail and the total "dead" area would be ∼5 µm in

diameter. Second, the QCL active region should be etched with an RIE system rather than a liquid chemical. This will reduce the active region undercut and likely decrease the III–V/Si taper transition loss[1]. Third, etch-loading features should be designed into the mask set to create a dense pattern of III–V mesas in areas near the laser mesas. The primary failure mechanism for the QCLs on Si was due to the large feature sizes and undesired etch-loading effects. Such features will help create a uniform topography around the lasers so that small features near the center and near the III–V/Si tapers can be resolved with the same photoresist and lithography recipes.

A thorough investigation into the absorption loss of SiO_2, Si_3N_4, Si, and Ge should be performed. Surface-normal measurements on thin films are typically reported to determine the spectral absorption edges of a material, but this method is not sensitive enough to provide relevant propagation loss values within the transparency window. Waveguide must be uniquely designed to have a high optical confinement in the material under investigation. The interaction length with the material can be extended by creating an on-chip resonator to measure the loss. There is a strong interest to compare high-quality films of SiO_2 and Si_3N_4 cladding materials with Si waveguide cores. Current measurements have not been tailored for this investigation. Rather, demonstrations such as the QCL on SOI presented in Chapter 7 use modes with high-confinement in the Si core to minimize the SiO_2 loss. The opposite design with high-confinement in the cladding, either SiO_2 or Si_3N_4, should be made for absorption loss characterization. The challenge of finding the absorption spectrum across a broadband is that facet coupling varies with wavelength[2], so a different test structure is necessary for each spectral band of interest.

[1] A. Spott has already successfully developed and demonstrated this fabrication process.

[2] In comparison, surface-normal measurements can easily be obtained over an ultra-broadband spectrum using a single lamp source.

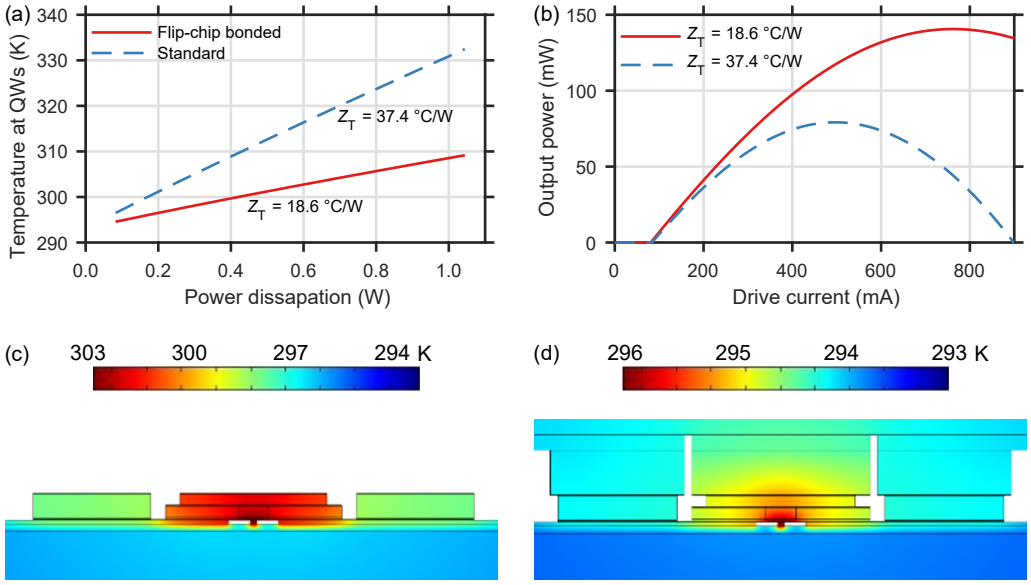

Figure 8.1: (a) Temperature on power dissipation in the active region is used to extract Z_T. (b) Modeled LIVs showing how the thermal dissipation affects the maximum output power of the two configurations. Temperature maps of bonded lasers (c) with and (d) without flip-chip bonding to an AlN submount.

Dissipation of heat from the laser active region can be increased with a flip-chip bonding procedure to mount the top-side of the lasers to an aluminum nitride (AlN) submount. In Fig. 8.1, the improvement is simulated using thermal conductivity values from literature [6]. In this case, the output power is expected to double as the thermal resistance (Z_T) decrease from 37.4 °C/W with the standard design to 18.6 °C/W with a flip-chip bond to an AlN submount.

Laser mirrors are defined by etching shallow patterns in the top of the Si waveguide. This process requires a finely-tuned etch recipe with a slow rate and it creates a large index perturbation. Consequently, the gratings are strong with $\kappa L \approx 10$ for the DFB. A weaker grating can be produced with a Ge-ion implant [7]. An experiment is performed on a DBR mirror in a mode-locked laser heterogeneously integrated on Si [8] to determine the current-injection tuning properties, shown in Fig. 8.2. Amplified spontaneous emission (ASE) spectra are measured for various current levels injected to the active region and

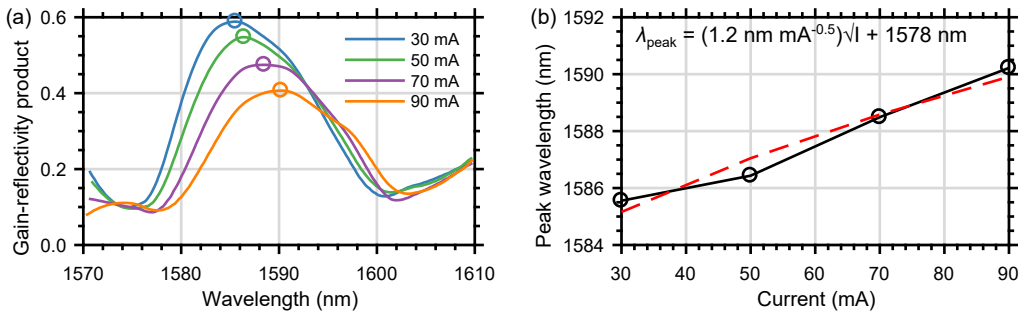

Figure 8.2: Experimental results of ion-implanted DBR grating tuning. (a) The gain-reflectivity product spectra. (b) Peak wavelength dependence on tuning current.

the gain-reflectivity product is calculated with the Cassidy method [9]. Within 60 mA above transparency, ∼4.7 nm of peak-wavelength tuning is observed. This preliminary experiment suggests that DBR lasers could be tuned to align with the AWG channels of a multi-spectral laser. Future work is necessary to determine the performance in the mid-IR.

A different waveguide platform can improve the thermal conductivity to the Si substrate and drastically improve the laser performance without performing a flip-chip bonding process. Two platforms are suggested: GOS and Si-on-AlN. These are motivated by the thermal conductivities of Ge and AlN (60 W/m K and 319 W/m K) compared to SiO_2 and Si_3N_4 (1.4 W/m K and 12 W/m K) [6, 10, 11]. The first, GOS, is already a commercially available as wafers and will improve the thermal dissipation to the substrate by removing the insulating SiO_2 or Si_3N_4 lower cladding materials. The second is a new proposal (Si-on-AlN) and one fabrication method is shown in Fig. 8.3. A film of AlN is grown on a Si substrate using molecular beam epitaxy (MBE) [12].

Another possibility for a new Si-based waveguide platform is to create amorphous-Si (α-Si) waveguide cores directly in crystalline-Si (c-Si): a pure-Si platform. This idea is inspired from two sources: the doped silica platform and the ion-implanted gratings [13]. The benefit is that a very low-cost platform could be produced with transparency over the

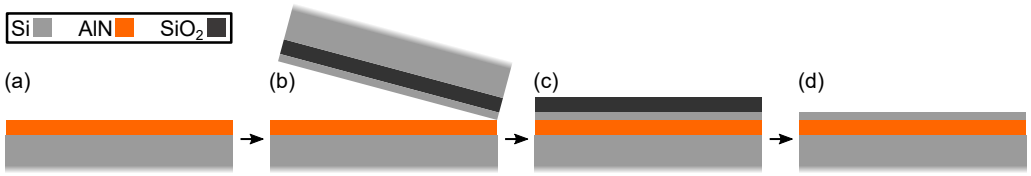

Figure 8.3: Proposed waveguide platform with AlN replacing the SiO_2 lower cladding. (a) AlN is grown on a Si substrate by MBE. (b) An SOI wafer is bonded to the AlN surface. (c) The Si substrate of the bonded SOI is removed by mechanical polishing and and ICP etch with $C_4F_8/SF_6/Ar$ gases. (d) The SiO_2 layer is removed with BHF.

entire transparency window of Si (1.2–6.0 µm). However, large mode sizes and bending radii would limit the performance of this platform. Waveguides could be defined by ion-implantation of either Si^{2+} or Ge^{2+} in a bare Si wafer to create a small and positive index perturbation [14]. This waveguide platform would support a high thermal conductivity if lasers are integrated by direct bonding.

Localized heating of the Si waveguide under the III–V laser may cause increased absorption loss due to an increased concentration of free-carriers. Partially etched waveguides should be used to allow for free-carrier diffusion away from the Si waveguide. By reducing the temperature of the Si waveguide, then the free-carrier concentration can also be reduced. Using the Si-on-AlN, GOS, or pure-silicon platforms are some examples that can achieve this.

8.2.2 Applications for arrayed waveguide gratings

Research on AWGs has historically been applied towards telecommunications. Only recently are large-scale PICs being demonstrated and AWGs are central components for any wavelength multiplexed system. Every year, new ideas and contributions are added to the AWG design methodology and demonstrations continue to improve performance [15–18]. As a result, new applications for AWGs are emerging. A recent demonstration uses an AWG as part of an on-chip photon entanglement source that enables quantum

key distribution, quantum random numbers, and quantum logic [19]. There is a growing field of interest in AWGs for astronomy [20, 21]. Active control is being integrated with AWGs for signal processing [22]. AWGs are being designed for tissue analysis as well [23].

8.3 Final word

The AWG design and characterization contributions in this work enable the full-integration of practical high-brightness lasers on Si. A multi-spectral QCL is the first demonstration of this technology. After similar lasers are demonstrated at multiple spectral bands, the broadband combiner designs and characterizations will provide a basis for engineering an ultra-broadband output. Research continues on the mid-IR high-brightness lasers due to their direct applications with molecular sensing, and the GOS is viewed as the seen as the next advancement for these devices.

This research has contributed to the fast-growing fields of Si and mid-IR photonics. Experiments on the system components have demonstrated the feasibility of an ultra-broadband high-brightness laser. Maturation of this technology is expected to result in large-scale manufacturing of these devices. A low-cost and configurable version of the high-brightness laser could revolutionize numerous applications spanning the fields of medicine, defense, optical communication, industrial manufacturing, and fundamental science.

References

[1] J. T. Bovington, M. J. R. Heck, and J. E. Bowers, "Heterogeneous lasers and coupling to Si_3N_4 near 1060 nm," Opt. Lett. **39**, 6017–6020 (2014).

[2] A. Spott, M. Davenport, J. Peters, J. Bovington, M. J. R. Heck, E. J. Stanton, I. Vurgaftman, J. Meyer, and J. Bowers, "Heterogeneously integrated 2.0 µm CW hybrid silicon lasers at room temperature," Opt. Lett. **40**, 1480–1483 (2015).

[3] N. Volet, A. Spott, E. J. Stanton, M. L. Davenport, L. Chang, J. D. Peters, T. C. Briles, I. Vurgaftman, J. R. Meyer, and J. E. Bowers, "Semiconductor optical amplifiers at 2.0-µm wavelength on silicon," Laser Photon. Rev. **11**, 1600165 (2017).

[4] A. Spott, J. Peters, M. L. Davenport, E. J. Stanton, C. Zhang, C. D. Merritt, W. W. Bewley, I. Vurgaftman, C. S. Kim, J. R. Meyer, J. Kirch, L. J. Mawst, D. Botez, and J. E. Bowers, "Heterogeneously Integrated Distributed Feedback Quantum Cascade Lasers on Silicon," Photonics **3**, 35 (2016).

[5] S. Srinivasan, N. Julian, J. Peters, D. Liang, and J. E. Bowers, "Reliability of hybrid silicon distributed feedback lasers," IEEE J. Sel. Topics Quantum Electron. **19**, 1501305–1501305 (2013).

[6] S. Adachi, "Lattice thermal conductivity of group-IV and III–V semiconductor alloys," J. Appl. Phys. **102**, 063502 (2007).

[7] R. Loiacono, G. T. Reed, G. Z. Mashanovich, R. Gwilliam, S. J. Henley, Y. Hu, R. Feldesh, and R. Jones, "Laser erasable implanted gratings for integrated silicon photonics," Opt. Express **19**, 10728–10734 (2011).

[8] M. L. Davenport, "Heterogeneous Silicon III-V Mode-Locked Lasers," Ph.D. thesis, University of California Santa Barbara (2017).

[9] D. T. Cassidy, "Technique for measurement of the gain spectra of semiconductor diode lasers," J. Appl. Phys. **56**, 3096–3099 (1984).

[10] X. Zhang and C. P. Grigoropoulos, "Thermal conductivity and diffusivity of free-standing silicon nitride thin films," Rev. Sci. Instrum. **66**, 1115–1120 (1995).

[11] T. Yamane, N. Nagai, S.-i. Katayama, and M. Todoki, "Measurement of thermal conductivity of silicon dioxide thin films using a 3ω method," J. Appl. Phys. **91**, 9772–9776 (2002).

[12] J. Norman. Personal communication.

[13] S. Homampour, M. P. Bulk, P. E. Jessop, and A. P. Knights, "Thermal tuning of planar Bragg gratings in silicon-on-insulator rib waveguides," Phys. Status Solidi C **6** (2009).

[14] M. L. Davenport. Personal communication.

[15] S. Tondini, C. Castellan, M. Mancinelli, C. Kopp, and L. Pavesi, "Methods for low crosstalk and wavelength tunability in arrayed-waveguide grating for on-silicon optical network," J. Lightw. Technol. **35**, 5134–5141 (2017).

[16] E. J. Stanton, N. Volet, and J. E. Bowers, "Low-loss demonstration and refined characterization of silicon arrayed waveguide gratings in the near-infrared," Opt. Express **25**, 30651–30663 (2017).

[17] K. Shang, S. Pathak, C. Qin, and S. J. B. Yoo, "Low-Loss Compact Silicon Nitride Arrayed Waveguide Gratings for Photonic Integrated Circuits," IEEE Photon. J. **9**, 1–5 (2017).

[18] J. Zou, Z. Le, J. Hu, and J.-J. He, "Performance improvement for silicon-based arrayed waveguide grating router," Opt. Express **25**, 9963–9973 (2017).

[19] N. Matsuda, H. Nishi, P. Karkus, T. Tsuchizawa, K. Yamada, W. J. Munro, K. Shimizu, and H. Takesue, "Generation of entangled photons using an arrayed waveguide grating," J. Opt. **19**, 124005 (2017).

[20] A. Stoll, Z. Zhang, R. Haynes, and M. Roth, "High-Resolution Arrayed-Waveguide-Gratings in Astronomy: Design and Fabrication Challenges," Photonics **4**, 30 (2017).

[21] P. Gatkine, S. Veilleux, Y. Hu, J. Bland-Hawthorn, and M. Dagenais, "Arrayed waveguide grating spectrometers for astronomical applications: new results," Opt. Express **25**, 17918–17935 (2017).

[22] M. R. Gehl, D. Trotter, A. Starbuck, A. Pomerene, A. Lentine, and C. DeRose, "High Resolution Silicon Arrayed Waveguide Gratings for Photonic Signal Processing Applications," in "Conference on Lasers and Electro-Optics," (Optical Society of America, 2017), p. SF1I.3.

[23] D. Geuzebroek, A. van Rees, E. Klein, and K. Lawniczuk, "Ultra-wide Band (400-1700nm) Integrated Spectrometer based on Arrayed Waveguide Gratings for Spectral Tissue Sensing," in "14$^{\text{th}}$ Int. Conf. on Group IV Photonics," (IEEE, 2017), pp. 83–84.